

***Meso-Beta Scale Numerical Simulation Studies of Terrain-Induced  
Jet Streak Mass/Momentum Perturbations***

***FY93 May Semi-Annual Report***

***submitted to the***

***Mesoscale Processes Research Program***

***Atmospheric Dynamics and Radiation Branch***

***Earth Science and Application Division***

***Office of Space Science and Applications***

***NASA Headquarters***

***Washington, D. C. 20546***

***Attention: Dr. Ramish Kakar, Program Manager***

***by***

***Yuh-Lang Lin and Michael L. Kaplan***

***Department of Marine, Earth, and Atmospheric Sciences***

***North Carolina State University***

***Raleigh, North Carolina 27695-8208***

***(919) 515-7977***

***May 1993***

*GRANT  
IN-46-CR  
163041  
P.80*

N93-27284

Unclas

G3/46 0163041

(NASA-CR-193045) MESO-BETA SCALE  
NUMERICAL SIMULATION STUDIES OF  
TERRAIN-INDUCED JET STREAK  
MASS/MOMENTUM PERTURBATIONS  
Semiannual Report (North Carolina  
State Univ.) 80 p

## Table of Contents

### Part I. 3-D Numerical Modeling of Terrain-Induced Circulations

(a) Additional Insights Into Gravity Wave Generation Mechanisms Based on the Control Simulation.....	1
(b) Ongoing Nested-Grid Numerical Simulations.....	3
(c) Work To be Completed During the Remainder of FY93.....	6
(d) Work Objectives for FY94.....	7

### Part II. Linear Theory and Theoretical Modeling

(a) The Free Response of a Uniform Barotropic Flow To An Initially Stationary Unbalanced (Ageostrophic) Zonal Wind Anomaly.....	10
(b) The Free Response of a Uniform Barotropic Flow To An Initially Stationary Balanced Zonal Wind Anomaly.....	19
(i) <i>Total Perturbation Response due to a Geostrophically Balanced         Zonal Wind Anomaly.....</i>	19
(ii) <i>Total Perturbation Response for an Inertially Balanced         Zonal Wind Anomaly.....</i>	21
(c) The Forced Response of a Uniform Barotropic Flow to an Independently	

Propagating Zonal Wind Anomaly.....	24
<b>References.....</b>	<b>32</b>
<b>List of Figures.....</b>	<b>33</b>
<b>Appendix A</b>	
Derivation of the Dispersion Relationship and Components of the Phase Speeds and Group Velocities for Three-Dimensional Linear Plane Waves Excited in a Uniform Barotropic Flow.....	36

## **Part I. 3-D Numerical Modeling of Terrain-Induced Cirulations**

During the first half of FY93 progress has been made in two areas. First, continued analyses have been performed in an effort to understand the physical processes at work in the GMASS control (smoothed terrain) simulation for the CCOPE case study. Second, a highly detailed plan has been formulated and is being implemented for the subsequent nested-grid CCOPE simulations with the GMASS model based upon inadequacies, limitations, and problems with the control simulation.

### **(a) Additional Insights Into Gravity Wave Generation Mechanisms Based on the Control Simulation**

During the early part of FY93 additional dynamical analyses were performed on the fields derived from the control simulation which were not presented in the FY92 November Semi-Annual report. This effort was focused on the problem of the model's ability to simulate the observed cross-stream ageostrophy over north central Idaho prior to the first CCOPE gravity wave episode observed by Koch and his colleagues. It was clearly evident that the control simulation employing highly smoothed terrain was not able to replicate the observed *intensity* of the unbalanced flow over this region at the 300 mb level at 1200 UTC 11 July 1981. While this was mentioned in the November Semi-Annual Report, subtle details concerning the inadequacy of the simulation have become more evident since then, resulting in a hypothesis which relates directly to the control simulation's inability to replicate the observed gravity waves.

A close examination of the observed versus simulated 300 mb height field at 1200 UTC 11 July 1981 indicates a concentrated region of 30 meter or greater height errors. This region extends along the northern border between Idaho and Montana due west of Kalispell, Montana and Missoula, Montana and northeast of Spokane, Washington along the Bitterroot Mountain chain. Here, 300 mb height errors in the 12 hour simulation average ~ +30 meters while just south,

southwest, and southeast of this region the errors become almost zero. This model deficiency has been more closely examined and is believed to be the reason why geostrophic adjustment was greatly underestimated by the GMASS control simulation during observed gravity wave episode I.

At first, the cause was assumed to be the smooth nature of the terrain reducing the upslope flow and adiabatic cooling along the Bitterroot Mountains prior to 1200 UTC. After further examination it appears that the problem is not only the terrain smoothness, but its unrealistically low elevation as well. The highest elevation in the smooth terrain data base within the Bitterroot Range is ~1500 m, i.e., ~850 mb. However, in nature much of this region extends from 1750 to 2250 m. This should extend the model's lowest sigma surface to >2500 m or close to 700 mb as opposed to just above 850 mb in the control simulation.

During the first 6 - 9 hours of the control simulation the 850 mb flow is virtually calm while the 700 mb flow is due southwesterly at ~10 m/sec. This southwesterly flow is nearly perpendicular to the northwest-southeast oriented Bitterroot Range, hence, it is directly upslope. The estimated intensity of the upslope vertical motion just below 700 mb due solely to the terrain would be ~5 cm/sec as opposed to ~0 cm/sec in the control run where much weaker terrain gradients as well as much lower elevation with a much weaker upslope wind component would combine to virtually suppress the upslope flow. Prolonged absence of this low-level lifting could change the sign of the upward motion over the mountains where simulated ascent at 700 mb and 500 mb never exceeded 5 cm/sec prior to 1200 UTC. As a matter of fact, much of the Bitterroot Range was covered by sinking motions in the control simulation prior to 1200 UTC at both 700 mb and 500 mb. The lack of low-level, i.e., ~700 mb and 500 mb ascent would change the sign of the adiabatic heating term in the model's thermodynamic energy equation throughout much of the column. Thus, adiabatic *cooling* along the border region between Idaho and Montana would be misrepresented as adiabatic *warming* prior to 1200 UTC. This could easily result in 2-4 K temperature errors which were too warm within the very stable part of the simulated column between 700 mb and 300 mb wherein the mean temperature would be too warm. This warm bias would then result in hydrostatic thickness errors wherein the column thickness was too large, i.e., 300 mb heights becoming too high. The

positive height anomaly would then act to reduce the the northwestward directed pressure gradient force responsible for accelerating the flow across the geostrophic stream by as much as 25% or more. The subsequent magnitude of the zonal wind component accelerations would be underestimated as the model attempted to *balance* the underpredicted Coriolis force resulting from the underpredicted cross stream wind component with the existing pressure gradient force resulting in a *weakening* of the radiation of gravity waves across Montana in the downstream direction of the CCOPE network. Divergence tendencies caused by the adjustment of the wind field into a state of geostrophic balance would be too weak in the control simulation because the pressure gradient force distribution was too homogeneous within the gravity wave source region over western Montana. This would be particularly significant at the 500 mb level where both the control simulation and the observations (as noted in the most recent paper by Koch et al.) indicate a well developed duct for the gravity waves.

This subtle error is clearly real in the control simulation. It is anticipated that the corrections to be discussed in the forthcoming section which are presently being implemented into the model will eliminate said problem. However, if our hypothesis is correct, it highlights the subtle mechanisms by which mountains can impose mass/momentum perturbations on the jet stream.

#### **(b) Ongoing Nested-Grid Numerical Simulations**

Based upon what was learned during the first year of the NASA contract involving the simulation of the role of terrain in jet streak mass/momentum perturbations, we have designed a simulation plan which maximizes the ability of the GMASS model to simulate the mesoscale phenomena observed by Koch and his colleagues over the CCOPE network for the 11-12 July 1981 case study.

We are presently in the process of preparing the model for nested-grid simulations employing a set of software modifications based on this plan. These modifications must synthesize the following improvements which were necessitated by lessons learned from

simplifying assumptions in the control simulation: 1) removal of model lateral boundary conditions from the regions of interest to minimize contamination by boundary noise, 2) increase horizontal resolution to the point necessary to resolve both the primary and secondary gravity waves observed within CCOPE as well as to negate the generation of numerical terrain-induced instabilities in the solution of the primitive equations, 3) employ minimal smoothing of the observed high resolution terrain data base to define the detailed variation in terrain forcing on the meso-beta scale mass and momentum fields, 4) employ sufficient vertical resolution to allow the Blackadar PBL parameterization to realistically flux sufficient sensible heat vertically to generate diabatic orogenic circulations without so much vertical resolution as to generate numerical terrain-induced instabilities, 5) employ sufficient upstream areal coverage to include upstream forcing of jet streak circulations, 6) employ sufficient downstream areal coverage to simulate convection generated by the terrain-induced waves and circulations as well as to simulate downstream gravity wave dissipation zones, 7) minimize internal memory limitations and maximize available processing time on the Cray Y-MP supercomputer at the North Carolina Supercomputing Center for several different simulations, and 8) maximize postprocessing diagnostic requirements regarding cross-stream trajectories and along-stream trajectory calculations of geostrophy, ageostrophy, Rossby numbers and divergence equation terms.

In an effort to meet this large matrix of totally necessary but internally conflicting requirements, we are implementing the following modifications to the model and terrain data base. Two different grid meshes within a single three-dimensional matrix of grid points will be employed in the subsequent numerical simulation studies. The first "coarse" mesh matrix of grid points spaced 16 km apart will include  $223 \times 146 \times 30$  grid points. This grid was formed by truncating approximately 9 degrees of longitudinal coverage from the 24 km control simulation area on the western upstream side and adding approximately 3 degrees of longitudinal coverage on the eastern downstream side. Additionally, approximately 4 degrees of latitudinal coverage on the southern side was truncated and approximately 2 degrees of latitudinal coverage on the northern side was added. Hence, the new "coarse" mesh grid will extend from approximately 2 degrees of longitude

west of the Pacific Coasts of California , Oregon, Washington, and British Columbia to central Illinois, eastern Wisconsin, and the Mississippi River Valley region in its upstream and downstream extents, respectively, while additional space has been added on the northern boundary to act as a buffer zone against contamination by boundary noise. These adjustments should remove northeastern boundary noise further from the regions of scientific interest, increase the space downstream for convection and gravity wave dissipation studies, and still insure enough upstream forcing from jet streak adjustments over the Pacific Coast region. This "coarse" grid matrix will soon be employed for 30 hour simulation studies commencing at 0000 UTC 11 July 1981 and integrated through 0600 UTC 12 July 1981.

Within the "coarse" mesh grid will be nested a matrix of  $223 \times 146 \times 30$  grid points spaced 8 km apart in the horizontal. This nested-grid model will receive its time dependent lateral boundary conditions from the "coarse" mesh model. The nested-grid model will be initialized from the "coarse" mesh simulation fields at 0900 UTC 11 July 1981 and run 21 hours to 0600 UTC 12 July 1981. The western boundary of the nested fine mesh grid will be located just west of the Idaho/Oregon and Idaho/Washington border region and extend to just west of the Minnesota/Dakotas and northern Iowa/northern Nebraska border regions. The northern border will be north of Montana by at least 1 degree of latitude. The time of initialization of this fine mesh simulation corresponds to approximately 1 to 2 hours prior to the observed generation of gravity waves and modeled generation of unbalanced flow in the 24 km control simulation over southwestern Montana on or about 1100 UTC 11 July 1981. The 8 km resolution should be more than sufficient to resolve the primary and secondary modes observed in the CCOPE data sets by Koch and his colleagues.

The vertical resolution to be utilized in both the "coarse" and fine mesh simulations was slightly degraded from 32 to 30 layers, i.e., from ~500 m to 533 m layer depths so that runs would fit comfortably within the available memory on the North Carolina Supercomputing Center's 40 megaword Cray Y-MP, i.e., ~38 megaword. We feel that the reduced vertical resolution from ~500 to ~533 meters would not significantly affect the performance of the Blackadar PBL scheme,



i.e., sensible heat flux rates would be reduced minimally, thus not adversely affecting the simulation of the surface heating-induced orogenic circulation.

In order to avoid numerical terrain-induced instabilities, the ultra-high resolution terrain data base will be smoothed slightly so that horizontal terrain gradients do not exceed 533 m/16 km. This will still allow terrain gradients which are at least 30 times larger than the 24 km control simulation employed and terrain maximum elevations which are nearly 50% higher. The nested-grid simulation will employ linearly interpolated terrain gradients not to exceed the above criteria. This still should be sufficient to resolve most of the meso-beta scale terrain forcing implicit in the high resolution data base.

Additionally, in an effort to reduce boundary condition noise, the specified diffusion and fast time steps employed in the forthcoming simulations will be increased and decreased, respectively, to increase the smoothing and provide a greater buffer against both nonlinear and linear instabilities, respectively.

### **(c) Work to be Completed During the Remainder of FY93**

First, complete the complex terrain nested-grid GMASS simulation described in (b), above, which has been designed to maximize the accuracy and detail of observed terrain variability over Idaho, Montana, and Wyoming without causing terrain instability, a significant reduction in surface sensible heat flux, or truncating upstream synoptic scale forcing mechanisms. This first of four simulations will *not* include the physics associated with condensational processes.

Second, perform a detailed dynamical analysis of the first complex nested grid GMASS simulation. This analysis will go further than the analysis of the control simulation because surface pressure tendencies as well as terms in the horizontal divergence equation within both Eulerian and Lagrangian frameworks will be analyzed both over and upstream from the CCOPE mesonet network. Compare the output to the observed analyses of Koch and his colleagues as well as to the control

simulation in an effort to determine the causes of, characteristics of, and evolution of simulated gravity waves during both observed gravity wave episodes.

Third, begin work on the first of two journal papers to be prepared on the CCOPE case study. The first paper will deal with the basic forcing mechanism for the dual gravity wave episodes prior to the onset of condensation processes. Additional model sensitivity studies will be required to be performed during FY94 before it can be submitted for publication. These sensitivity studies will involve turning off the surface sensible heat flux and smoothing the terrain during analogous nested-grid simulations.

#### **(d) Work Objectives for FY 94**

First, perform a second nested-grid GMASS simulation analogous to that performed during FY93, however, do not allow surface sensible heat flux to perturb the fields. This will aid in the determination of the importance of surface sensible heat flux in the orogenic circulation which may be forcing CCOPE gravity waves. This simulation will employ complex terrain but neglect the physics associated with condensation. Compare pressure tendencies and divergence equation terms to the nested-grid simulation with surface sensible heat flux. Include the results in the first journal article which was started during FY93.

Second, perform a third nested-grid GMASS simulation analogous to that performed during FY93, however employ the same highly smoothed terrain as was employed for the control simulation. This should confirm or disprove the hypothesis that the CCOPE gravity waves could have resulted from geostrophic adjustment or shearing instability alone, independent of terrain forcing. This simulation will employ surface sensible heat flux physics but neglect the physics associated with condensation. Compare pressure tendencies and divergence equation terms to the nested-grid simulation with complex terrain. Include the results in the first journal article which was started during FY93.

Third, finish and submit the first journal article for publication which focuses on CCOPE gravity wave generation mechanisms independent of condensation processes.

Fourth, transfer the version of GMASS with explicit microphysical processes from the NASA Goddard Laboratory for Atmospheres to the North Carolina Supercomputing Center's Cray Y-MP. Test the model.

Fifth, perform a fourth nested-grid GMASS simulation analogous to those performed during FY93 and FY94, however, employ the explicit microphysics version and include the physics associated with condensational processes. Include complex terrain and surface sensible heat flux. This will allow the determination of the role of condensation in the initiation and evolution of the gravity waves observed during CCOPE as well as the role of gravity waves in initiating mesoscale convective complex systems. Compare pressure tendencies and divergence equation terms to the other nested-grid simulations. Compare simulated condensation and precipitation to observed satellite, radar, and surface observations.

Sixth, write the second journal article which emphasizes the role of condensation in gravity wave initiation and evolution. Submit this article for publication when completed.

Seventh, prepare a conference preprint article to be presented at either the forthcoming AMS Mesoscale Processes or Numerical Weather Prediction Conferences scheduled for late in calendar year 94. The paper will summarize the results of the numerical simulations in comparison to the observations published by Koch and his colleagues.

Eighth, prepare a final project report which compares the nested-grid simulations in depth. Detail the role of terrain in forcing the initiation and evolution of gravity waves as well as all forms of mesoscale jet streak mass/momentum perturbations.

## **Part II. Linear Theory and Theoretical Modeling**

During FY93, Dr. Yuh-Lang Lin and Mr. Ronald P. Weglarz have investigated the fundamental dynamics associated with both the free and forced response of idealized models of the

terrestrial planetary atmosphere to localized *unbalanced and balanced non-propagating* (free) as well as *independently propagating* (forced) zonal wind anomalies in order to identify the inertia-gravity waves generated during this type of geostrophic adjustment process, so that these fundamental modes may be better identified and distinguished from the continuous spectrum of inertia-gravity waves found in more complex synoptic scale situations. Attention has been focused on the response of the basic state (i.e. synoptic scale) *flow* to the *alongstream* shear which a propagating midlatitude upper tropospheric jet streak exerts on the environmental jet stream flow in which it is embedded. We approach the problem from a theoretical perspective by assuming that the zonal wind anomaly is a small amplitude perturbation to an otherwise horizontally as well as vertically homogeneous (i.e. barotropic) basic state flow. Note that at this point, we cautiously prefer to use the terminology 'zonal wind anomaly' since jet streaks are uniquely defined mesoscale structures embedded within the planetary jet stream in terms of associated thermally direct and indirect ageostrophic circulations, and play a major role as upper level tropospheric forcing mechanisms in a variety of mesoscale processes. One of the major objectives of our research has been to identify and distinguish the mechanisms responsible for the ageostrophic circulations in barotropic versus baroclinic flows. It is our opinion that the response may be identified as a 'jet streak' if and only if the proper thermally direct and indirect circulations, whether free or forced, are present. This is another key point which *uniquely distinguishes* our geostrophic adjustment work from the traditional problems investigated by classical adjustment theory (Rossby, 1938, Chan, 1945, Blumen, 1972) and recently published work (Duffy, 1990, Fritts and Luo, 1992, Luo and Fritts, 1993). The constraint of barotropy will be removed in subsequent work which is currently in progress and is planned to be continued into the latter half of FY93 and early FY94. However, since the present line of research attempts to fill the gap between the very idealistic initial states traditionally investigated by classical adjustment theory and the more complex evolutionary states commonly found in the real atmosphere, a fundamental understanding of the geostrophic adjustment of the simpler case of uniform barotropic flows must be considered first. For the sake of completeness, both homogeneous and continuously stratified

barotropic flows have been considered, but for the sake of brevity and for comparison with recently published work, we present solutions for the continuously stratified case here only.

**(a) The Free Response of a Uniform Barotropic Flow to an Initially Stationary Unbalanced (Ageostrophic) Zonal Wind Anomaly**

*(i) Total Perturbation Response*

In order not to unduly overburden the reader with complex mathematical details, we shall focus attention on a physical analysis of the flow response through a discussion of the fundamental dynamics associated with the geostrophic adjustment process in conjunction with a series of representative figures which indicate the major features of the flow response. As a first approximation in investigating the inertia-gravity wave radiation field, we assume that the zonal wind anomaly is located far enough above the planetary surface such that the free response in an unbounded, uniformly barotropic, rotating, continuously stratified, Boussinesq *flow* correctly models the first order dynamics of the inertia-gravity wave radiation field and adjustment to geostrophic equilibrium. Similar models have been recently published in the refereed literature (Fritts and Luo, 1992, Luo and Fritts, 1993), and are commonly employed in geostrophic adjustment studies. It is important to distinguish between the *free* response of the barotropic current versus the *forced* response of the barotropic current, since the former physical system conserves potential vorticity while the latter physical system does not. In fact, as we shall see later, external forcing provides for a source of additional potential vorticity generation which can significantly alter the characteristics of the initial state potential vorticity.

Starting from the linearized continuum field equations, it is possible to derive wave equations governing the response for the total zonal (east-west), meridional (north-south) perturbation winds ( $u'$  and  $v'$  respectively), the perturbation vertical velocity ( $w'$ ), perturbation pressure ( $p'$ ) and perturbation potential temperature ( $\theta'$ ). These wave equations are

inhomogeneous due to the contribution from the linearized perturbation potential vorticity of the initial state which governs or characterizes the nature of the particular solutions (i.e. the geostrophic equilibrium or steady state solutions). It is readily determined that the total zonal wind perturbation is governed by the meridional gradient of the linearized initial state potential vorticity,  $(\partial q'/\partial y)$ , the total meridional wind perturbation is governed by the zonal gradient of the linearized initial state potential vorticity,  $(\partial q'/\partial x)$ , the perturbation pressure is governed solely by the linearized initial state potential vorticity,  $(q')$ , while the potential temperature perturbation is governed by the vertical gradient of the linearized initial state potential vorticity,  $(\partial q'/\partial z)$ . The linearized wave equation governing the perturbation vertical velocity is homogenous in the sense that no contribution of the linearized initial state potential vorticity is imparted to this dynamical field *directly*. Therefore, the vertical velocity field evolves solely due to the evolution of the associated mass  $(\theta')$  and momentum  $(u', v')$  fields. The linearized perturbation potential vorticity is defined here as

$$q'(x,y,z,t) = \frac{\partial v'}{\partial x}(x,y,z,t) - \frac{\partial u'}{\partial y}(x,y,z,t) + \frac{f}{\rho_0 N^2} \frac{\partial^2 p'}{\partial z^2}(x,y,z,t) \quad (1).$$

In fact, the inhomogeneous terms which govern the response of the linearized dynamical fields in the presence of a uniform basic state current depend on  $q'(x,y,z,t)$ , and not merely  $q'(x,y,z, t = 0)$ . In other words, *the conservation relation of classical linear geostrophic adjustment theory*, namely

$$\frac{\partial q'}{\partial t} = 0 \quad (2),$$

which states that small-amplitude perturbations in a quiescent or motionless basic state can be determined solely from a knowledge of the initial state potential vorticity, *is no longer valid*. In the presence of a nonzero basic state, the conservation relation for the linearized perturbation potential vorticity becomes

$$\frac{\partial q'}{\partial t} + \left( U \frac{\partial}{\partial x} + V \frac{\partial}{\partial y} \right) q' = 0 \quad (3).$$

Note that Equation (3) immediately implies that the initial state potential vorticity (hereafter PV) anomaly *is advected downstream of the initial source location by the basic state current*. Therefore,

just by including a nonzero basic state current, our model offers a more physically realistic scenario of geostrophic adjustment processes in a rotating planetary atmosphere. Furthermore, the recently published results by Luo and Fritts (1993) will be closely approximated within the context of our theory in the asymptotic limit of a quiescent or motionless basic state.

Figures 1a, 1b, 1c, 1d, 1e, and 1f show the three-dimensional linear theoretical response of a *quiescent*, unbounded, continuously stratified, rotating, uniformly barotropic Boussinesq flow to an unbalanced localized zonal wind anomaly introduced into the flow at  $t = 0$  at  $(x,y,z) = (0,0,0)$  one hour after its introduction. Horizontal cross sections on the  $z = 0$  plane as well as vertical cross sections on the  $y = 0$  plane are presented. The  $z = 0$  level on the  $y = 0$  vertical plane is defined to be the level at which the zonal wind anomaly is introduced, and may be considered to be approximately 32 km above the planetary surface, although it should be kept in mind that no rigid lower boundary formally exists. By unbalanced we mean that only the total zonal wind anomaly contributes to the linearized perturbation potential vorticity of the initial state [i.e. 2<sup>nd</sup> term on the r. h. s. of Eqn. (1)]. The initial zonal wind anomaly was specified to have the following horizontal and vertical structure dependence:

$$u'(x,y,z,t=0) = u'_{jet}(x,y,z) = \frac{u_{j0}}{(x^2/a^2 + y^2/b^2 + z^2/c^2 + 1)^{3/2}} \quad (4),$$

where  $a$ ,  $b$ , and  $c$  refer to the anomaly's zonal, meridional, and vertical half-widths, respectively. The initial maximum magnitude of the anomaly ( $u_{j0}$ ) is chosen to be 10 m/sec, and the initial zonal and meridional half-widths were specified to be equal to  $a = b = 500$  km, while the initial vertical half-width was specified to be  $c = 5$  km. At this time ( $t = 1$  hr), we see that the response consists of an adjustment in not only the total perturbation zonal wind field, but compensating adjustments in the other dynamical fields ( $v'$ ,  $w'$ ,  $p'$ , and  $\theta'$ ). Fig. 1a shows that the magnitude of the zonal wind anomaly has reduced from its initial value of 10 m/sec to approximately 8 m/sec in the first hour of the response. A southeastward directed meridional wind component has developed, whose maximum magnitude is approximately -3 m/sec, and is due to the initial

meridional acceleration ( $\partial v'/\partial t$ ) imposed by the Coriolis force acting on the unbalanced zonal wind anomaly. At this time, the vertical extent of the meridional wind anomaly is limited to the initial source region of the zonal wind anomaly. Fig. 1b shows the corresponding perturbations in the pressure and potential temperature fields on the  $z = 0$  and  $z = -1$  km horizontal planes, respectively, along with vertical cross sections of these fields on the  $y = 0$  plane. Within the initial source region, i.e.,  $-10 \text{ km} < z < +10 \text{ km}$ , the pressure perturbation consists of a low-high dipole couplet, with maximum and minimum values of approximately  $+1 \text{ mb}$  and  $-1 \text{ mb}$ , respectively. This structure is due primarily to the initial perturbation pressure tendency ( $\partial p'/\partial t$ ) imposed on the barotropic current when the zonal wind anomaly was introduced. This perturbation pressure tendency is proportional to the initial perturbation divergence field associated with the zonal wind anomaly. Note that the dipole structure reverses its pattern for  $z > +16 \text{ km}$ , and  $z < -16 \text{ km}$ . This is due to the vertical wavenumber dependence on the perturbation pressure tendency, which is proportional to  $1/m^2$ . Also shown in Fig. 1b is the response of the perturbation potential temperature field at this time, which is indicative of hydrostatic balance between the perturbation pressure and temperature fields, which holds for all time since we have from the outset assumed that the perturbations are hydrostatic. Note that in the region of low pressure on the  $z = -1 \text{ km}$  horizontal plane, adiabatic cooling exists at this time, while in the region of high pressure, a region of adiabatic warming is present, whose maximum values are approximately  $|0.1 \text{ K}|$  at this time. Also note that the potential temperature field is plotted at  $z = -1 \text{ km}$  since it is exactly zero at the jet level ( $z = 0$ ) due to the  $1/m$  dependence of this dynamical field on the vertical wave number.

Figure 1c shows the horizontal cross sections of vertical velocity and perturbation divergence fields on the  $z = -1 \text{ km}$  and  $z = 0$  horizontal planes respectively, along with vertical cross sections of these fields on the  $y = 0$  plane at this time. The vertical velocity field shows a dipole pattern, with rising motion in the jet entrance region (i.e.  $x < 0$ ,  $-500 \text{ km} < y < +500 \text{ km}$ ) and sinking motion in the jet exit region (i.e.  $x > 0$ ,  $-500 \text{ km} < y < +500 \text{ km}$ ). It is this vertical motion field which is responsible for the regions of adiabatic cooling (warming) in the jet's entrance (exit) regions at  $z = -1 \text{ km}$  (Fig. 1b). This field of vertical motion is induced from the



divergence associated with the initial zonal wind anomaly. The perturbation divergence field at this time shows a localized region of divergence (convergence) in the jet's entrance (exit) regions due to the introduction of a positive zonal wind anomaly into a quiescent or motionless basic state flow.

Figure 1d shows the horizontal cross sections of perturbation relative vorticity of the total perturbation wind field and the corresponding streamlines of the induced flow on the  $z = 0$  plane respectively, along with a vertical cross section of the perturbation relative vorticity on the  $y = 0$  plane at this time. A region of positive (cyclonic) relative vorticity exists north of the jet (i.e.  $y > 0$ ), while a region of negative (anticyclonic) relative vorticity exists south of the jet ( $y < 0$ ). The vertical cross section at  $y = 0$  shows that this perturbation field is confined to the initial source region of the zonal wind anomaly at this time. This figure also shows that the induced flow at this time is primarily southeasterly due to the combination of a positive zonal wind perturbation with a southeasterly directed meridional wind component forced by the initial meridional acceleration ( $\partial v'/\partial t$ ) due to rotational effects (i.e. Coriolis forcing) imposed by conservation of meridional momentum. Figs. 1e and 1f show vertical cross-sections along the  $x = 0$  plane of the induced response at this time.

Figures 2a, 2b, 2c, 2d, 2e, and 2f show the response of the quiescent, continuously stratified fluid three hours after the introduction of the ageostrophic (unbalanced) zonal wind anomaly. Horizontal cross sections of the total zonal and meridional perturbation winds on the  $z = 0$  plane along with vertical cross sections of these fields on the  $y = 0$  plane are presented in Fig. 2a. At this time, the zonal wind perturbation has acquired a preferential elongation along the line  $y = 0$ , indicating that at least on this plane ( $z = 0$ ), there is a predisposal for inertia-gravity wave energy radiation along the  $x$ -axis. The magnitude of the zonal wind anomaly has decreased further to a value of approximately 3 m/sec, while weak counter currents of total perturbation zonal wind (i.e.  $u' < 0$ ) have developed to the north and south of the main wind anomaly, whose centers are located approximately 900 km on either side of the line  $y = 0$ . Fig. 2a also indicates that the magnitude of the meridional wind perturbation has further strengthened to approximately - 5 m/sec at this time,

and is still primarily confined to the initial source region occupied by the ageostrophic zonal wind anomaly.

Fig. 2b shows horizontal cross sections of the pressure and potential temperature perturbations on the  $z = 0$  and  $z = -1$  km planes, respectively, along with vertical cross sections of these fields on the  $y = 0$  plane at this time ( $t = 3$  hr). The absolute magnitude of the pressure perturbation has been reduced from 1.0 to approximately 0.8 mb as compared to the previous two hour period, and shows a major clockwise or anticyclonic rotation around the  $(x, y) = (0, 0)$  point in the  $z = 0$  plane. This motion is indicative of the induced perturbation pressure or mass field adjusting to the non-divergent part of the wind field, as predicted by classical geostrophic adjustment theory. The perturbation potential temperature field response at this time has increased in magnitude slightly to roughly 0.16 K at this time, and shows features of clockwise rotation around the point  $(x, y) = (0, 0)$  in the  $z = 0$  plane, and a low-high dipole structure similar to the horizontal structure of the perturbation pressure field, as required by the hydrostatic balance. Vertical cross sections on the plane  $y = 0$  indicate not only a propagation of inertia-gravity wave energy horizontally at the  $z = 0$  level, as can be inferred from the oppositely propagating low and high perturbation pressure cells of approximately 0.6 mb magnitude (compare with Fig. 1b), but vertical propagation of inertia-gravity wave energy in this plane above and below  $z = 0$  as well.

Fig. 2c shows the horizontal cross sections of vertical velocity and total perturbation divergence fields on the  $z = -1$  km and  $z = 0$  km planes, respectively, along with vertical cross sections of these fields on the  $y = 0$  plane at this time. Both fields indicate a strong rotation around the point  $(x, y) = (0, 0)$  in the  $z = 0$  plane, similar to the response found in both the perturbation pressure and potential temperature fields. The absolute magnitude of these fields has been reduced slightly as compared to their values two hours before, and whose vertical cross sections on the plane  $y = 0$  show strong indication of inertia-gravity wave energy propagation away from (i.e. above and below) the initial source region of the zonal wind anomaly.

Fig. 2d shows the horizontal cross sections of perturbation relative vorticity and streamlines of the induced flow on the  $z = 0$  plane, along with a vertical cross section of the relative

vorticity at this time on the  $y = 0$  plane. Notice that the characteristic clockwise or anticyclonic rotation around the point  $(x, y) = (0, 0)$  in the  $z = 0$  plane is present here as well. This character of the response can be explained by deriving the dispersion relationship for three-dimensional linear plane waves satisfying the linearized wave equation governing the response of small-amplitude perturbations excited in this physical system (see Appendix A). From this, it can be seen that at  $(x, y, z) = (0, 0, 0)$ , singularities exist in the horizontal ( $k, l$ ) and vertical ( $m$ ) wavenumbers. The angular frequency of the three-dimensional linear plane waves comprising the response at this point in physical space is exactly equal to the Coriolis or inertial frequency ( $\sim 17$  hours at  $45^\circ$  North latitude) at this location, thereby implying that this point in physical space undergoes a purely inertial oscillation. As shown by Chan (1945) for a rotating homogeneous fluid, and by Zhu and Holton (1987) as well as Luo and Fritts (1993) for a rotating continuously stratified fluid, the magnitude of this inertial oscillation tends to asymptotically approach the steady state or geostrophic equilibrium solution within several inertial periods. Linear inertia-gravity wave theory allows one to prove that inertia-gravity waves tend to exhibit characteristic anticyclonic or clockwise rotation. Figures. 2e and 2f show the vertical cross sections of the response for the various perturbation fields on the plane  $x = 0$  at this time.

Figures 3a, 3b, and 3c show the linear, three-dimensional steady state, non-divergent geostrophic equilibrium solution of a quiescent, unbounded, continuously stratified, rotating Boussinesq fluid imposed by the introduction of the divergent, unbalanced (ageostrophic) zonal wind anomaly given by Eqn (4). Fig. 3a shows the horizontal cross section of the total zonal and meridional wind perturbations on the  $z = 0$  plane, along with the vertical cross section of the total zonal wind perturbation on the  $y = 0$  plane. The steady state non-divergent zonal wind perturbation has a magnitude of approximately 3.3 m/sec, and exhibits relatively weak compensating perturbation zonal counter currents ( $u' < 0$ ) of magnitude 0.5 m/sec located to the north and south of the main non-divergent zonal wind perturbation. The existence of these counter currents is due to the induced cyclonic (anticyclonic) flow around the steady state low (high) perturbation pressure distribution (Fig. 3b) which was generated as the mass field adjusted to the

non-divergent (geostrophic) portion of the initial total zonal wind field of the ageostrophic jet. These counter currents were first discovered in the theoretical work on geostrophic adjustment of a rotating homogeneous fluid by Rossby (1938), and are a direct consequence of the conservation of linearized perturbation potential vorticity. It should be noted that the steady state geostrophic equilibrium solution presented in Luo and Fritts (1993) does not indicate the presence of the compensating zonal counter currents, and although their forced problem is *mathematically* equivalent to our initial value problem, the external momentum forcing in their model provides a mechanism which *physically* violates the conservation of linearized perturbation potential vorticity, and provides for a source of additional linearized potential vorticity generation. As we shall see, the forced and free responses need not necessarily be similar.

The horizontal cross section of the steady state meridional wind perturbation on the  $z = 0$  plane in Fig. 3a indicates confluence (diffluence) in the jet's entrance (exit) regions. The vertical cross section of the zonal wind perturbation on the plane  $y = 0$  indicates a somewhat broader distribution in the vertical than that associated with the initial unbalanced zonal wind anomaly. This result is consistent with the theoretical work of Bolin (1953) who found that for an infinite, two-dimensional ageostrophic current introduced into a rotating, continuously stratified ocean with a free surface capable of exhibiting vertical displacement, the vertical structure of the final, geostrophic, non-divergent equilibrium state is smoothed or broadened as compared to the vertical structure associated with the initial state since the amplitude of the higher baroclinic modes (i.e. modes with increasing  $m$ ) tend to be reduced relative to modes with smaller  $m$ . Therefore, since the vertical wavenumber is defined here as  $m = 2\pi/L_z$ , these previous theoretical results along with ours indicate that shallow ageostrophic zonal wind anomalies (small  $L_z \rightarrow$  large  $m$ ) will undergo a greater vertical smoothing as compared to deep ageostrophic zonal wind anomalies (large  $L_z \rightarrow$  small  $m$ ). Note that  $m$  here refers to the preferential baroclinic mode excited by an unbalanced (ageostrophic) zonal wind anomaly of depth  $L_z$ . (The preferential horizontal wavenumbers of the primary baroclinic modes will be given by  $k = 2\pi/L_x$ , and  $l = 2\pi/L_y$ ). Similar results have been found for other two-dimensional geostrophic adjustment problems (Walterscheid and Boucher,

1984). Also note that since the steady state equilibrium solution is one of both geostrophic as well as hydrostatic balance, it constitutes a *thermal wind balance among the perturbation fields*.

With the introduction of a nonzero basic state flow (i.e.  $U, V > 0$ ), the phase speed of the three-dimensional linear plane waves is modified such that the propagation speeds of the inertia-gravity modes excited by the ageostrophic (divergent) portion of the initial total zonal wind anomaly are decreased by  $U$  for modes propagating against the basic state current, and increased by  $U$  for modes propagating with the basic state current. Except for the modification to the horizontal and vertical components of the phase speeds and group velocities due to the presence of a nonzero basic state flow, the adjustment to geostrophic equilibrium proceeds along the lines indicated in the above paragraphs. However, *with the addition of a nonzero basic state barotropic flow, the steady state, non-divergent geostrophic equilibrium solution is advected downstream by the basic state flow*. Therefore, our theory not only immediately generalizes the results of classical adjustment theory for resting or quiescent base states, but *the basic state current provides the physical mechanism for vorticity and temperature advection associated with the potential vorticity anomaly represented by the non-divergent, geostrophically balanced zonal wind anomaly*. These physical mechanisms are known to play a crucial role in the development of synoptic scale disturbances and are usually associated with baroclinic waves in a baroclinic atmosphere. However, the vorticity and temperature advection provided by the downstream advection of the geostrophically balanced zonal wind (PV) anomaly from its initial source location by the barotropically uniform basic state current provides an idealized representation of the upper level forcing mechanisms commonly associated with midlatitude upper tropospheric jet streaks. Based on this result, an investigation of the fundamental dynamics of this type of upper-level vorticity and temperature advection over isolated orographic and thermal forcings in barotropic atmospheres is warranted, and may have important implications when applied to the lee and coastal cyclogenesis problems. Future work along these lines is being planned.

**(b) The Free Response of a Uniform Barotropic Flow to an Initially Stationary Balanced Zonal Wind Anomaly**

The linearized field equations allow for an investigation of the response or geostrophic adjustment dynamics of a uniformly barotropic basic state flow to a variety of *linear balanced initial states* not commonly treated in classical adjustment theory, but nevertheless have important theoretical implications for the initialization of simple numerical models, data assimilation, as well as the early or short period response of mesoscale models, since most model initial states require an optimum balance between the mass and momentum fields in order to minimize the total number of inertia-gravity modes at the beginning of a numerical simulation in order to provide the least contamination of the slow manifold (quasi-geostrophic) dynamics. Indeed, one of the greatest applications of classical geostrophic adjustment theory has been in the initialization of numerical weather prediction or primitive equation models. It is our intent, however, in this section to provide a preliminary discussion of the fundamental dynamical response of a uniformly barotropic basic state flow to initially balanced zonal wind anomalies, with emphasis on the physical differences in the geostrophic adjustment process between these types of initial states as compared to the unbalanced or ageostrophic initial states of Section (a), with minimal emphasis on practical applicability of the theory.

*(i) Total Perturbation Response due to a Geostrophically Balanced Zonal Wind Anomaly*

By balanced initial states, we mean that both meridional wind ( $v'$ ) and pressure ( $p'$ ) perturbations contribute to the total linearized perturbation potential vorticity ( $q'$ ) of the initial state along with the zonal wind anomaly ( $u'$ ) at  $t = 0$ . The first linear balance relationship that we investigate is one of initial geostrophic balance between the perturbation mass and momentum fields, i.e., we assume that at  $t = 0$ , the following relationships are valid:

$$\frac{1}{\rho_0} \frac{\partial p'}{\partial y} = -f u'_{jet} \quad (5),$$

$$f v' = \frac{1}{\rho_0} \frac{\partial p'}{\partial x} \quad (6).$$

We assume that the structure of the zonal wind anomaly is known. Then, utilizing the geostrophic relationship of Eqn. (5) to approximate the conservation of meridional momentum, we can determine the perturbation pressure distribution, and from the geostrophic approximation of the conservation of zonal momentum, Eqn (6), once the perturbation pressure is known, the meridional wind perturbation can then be determined. Each perturbation ( $u'$ ,  $p'$ , and  $v'$ ) will contribute to the total linearized perturbation potential vorticity ( $q'$ ) of the initial state (see Eqn. (1)). Linear potential vorticity dynamics indicates that a geostrophically balanced zonal wind anomaly introduced into a nonzero barotropic basic state is simply advected downstream of the initial source location by the uniform current, and that neither the magnitude or geometry (morphology) of the initial zonal wind anomaly changes as it is advected downstream. No inertia-gravity waves are generated since the initial state is purely non-divergent, and constitutes a minimum energy state. It is to this equilibrium state which an initially ageostrophic or unbalanced zonal wind anomaly will asymptotically approach, as the physical response in Section (a) clearly indicates. Since the physical interpretation of the response to this type of initial balance is fairly straightforward, and should offer no conceptual difficulties to the reader, we do not present any figures illustrating this simple downstream advection.

Therefore, linear geostrophic adjustment theory for this type of balanced initial state indicates that a geostrophically balanced state is the perfect initialization for incorporating zonal wind anomalies in (linear) primitive equation models. This is found, in general not to be the case, since numerical models integrate *discretized* versions of the *continuum* field equations, and therefore only *approximate* the true nature of the geostrophic balance.

(ii) *Total Perturbation Response for an Inertially Balanced Zonal Wind Anomaly*

By inertially balanced, we mean that the linear geostrophically balanced initial state of the previous section is modified to take into account the effects of the inertial advective terms ( $U \partial u'/\partial x$ ,  $V \partial u'/\partial y$ ,  $U \partial v'/\partial x$ , and  $V \partial v'/\partial y$ ) such that the following balance relationship is assumed to exist at  $t = 0$ :

$$\left( U \frac{\partial}{\partial x} + V \frac{\partial}{\partial y} \right) u'_{jet} - f v' + \frac{1}{\rho_0} \frac{\partial p'}{\partial x} = 0 \quad (7),$$

$$\left( U \frac{\partial}{\partial x} + V \frac{\partial}{\partial y} \right) v' + f u'_{jet} + \frac{1}{\rho_0} \frac{\partial p'}{\partial y} = 0 \quad (8).$$

These balance relationships are obtained when the initial local or Eulerian accelerations  $\partial u'/\partial t$  and  $\partial v'/\partial t$  vanish identically. Under the assumption that the zonal wind anomaly structure is known, then the linearized zonal and meridional momentum equations, Eqns (7) and (8), may be combined to yield relationships for the initial meridional wind perturbation ( $v'$ ) and pressure perturbation ( $p'$ ) in terms of the initial zonal wind anomaly, all of which contribute to the total linearized perturbation potential vorticity ( $q'$ ) of the initial state. Note that the horizontal advection of the zonal wind and meridional wind perturbations at  $t = 0$ , will in general, yield a divergent initial state. Another way to interpret this balance relationship is to take the difference  $\partial/\partial x$  (8) -  $\partial/\partial y$  (9), which indicates that the perturbation divergence associated with the zonal wind anomaly is balanced by the linearized vorticity advection.

Figures 4a, 4b, 4c, 4d, 4e, and 4f show the total perturbation response of a uniformly barotropic flow of magnitude  $U = 10$  m/sec to an inertially balanced zonal wind anomaly of the same magnitude whose horizontal and vertical structure is specified by Eqn (4) at  $t = 1$  hr after it is inserted into the flow. The initial half-widths in the horizontal and vertical are identical to the unbalanced or ageostrophic case presented in Figs 1a - 1f. Fig. 4a shows horizontal cross sections



of the total zonal wind field ( $u = U + u'$ ) and meridional wind perturbation ( $v'$ ) on the  $z = 0$  plane, along with vertical cross sections of these same fields on the  $y = 0$  plane. The zonal wind perturbation has a maximum value of approximately 8.7 m/sec at this time, exhibits a slight preferential anticyclonic curvature, and is primarily confined both horizontally and vertically within the initial source region. By comparison, the meridional wind perturbation at this time on the  $z = 0$  plane is markedly different from the unbalanced response at the same time (Fig. 1a). For the inertially balanced initial state, the meridional wind anomaly exhibits a dominant two-cell character on the southern side ( $y < 0$ ) of the zonal wind anomaly, although careful inspection of the figure reveals a northward directed component everywhere in the region  $x < 0$ , while a southward directed component exists everywhere in the region  $x > 0$ . The horizontal structure of the meridional wind field can be explained as follows: Consider the linearized zonal momentum equation, Eqn (7). This can be rearranged to yield

$$v' = \frac{1}{f} \left[ \left( U \frac{\partial}{\partial x} + V \frac{\partial}{\partial y} \right) u'_{jet} + \frac{1}{\rho_0} \frac{\partial p'}{\partial x} \right] = 0 \quad (9).$$

The early stages in the evolution of the meridional wind component will be dominated by the alongstream gradient in the zonal wind anomaly, and since the meridional component of the basic state barotropic current,  $V = 0$ , Eqn (9) reduces to

$$v' = \frac{1}{f} U \frac{\partial u'_{jet}}{\partial x} \quad (10).$$

Then, in the region  $x < 0$ , where  $\partial u'/\partial x > 0$ ,  $v' > 0$ , and in the region  $x > 0$ , where  $\partial u'/\partial x < 0$ ,  $v' < 0$ . Fig. 4b shows horizontal cross sections of the perturbation pressure and total potential temperature fields on the planes  $z = 0$  and  $z = -1$  km, respectively. Vertical cross sections of these fields are also indicated on the  $y = 0$  plane. The pressure perturbation exhibits a maximum of approximately 8.7 mb on the south side ( $y < 0$ ) of the zonal wind anomaly. The meridional

structure of the perturbation pressure field may be explained by considering the following example presented for illustrative purposes. Let us assume that the zonal wind anomaly on the  $z = 0$  plane can be approximately represented by

$$u'_{jet}(x, y, z = 0) \sim u_{j0} \left( \frac{a^2}{x^2 + a^2} \right) \left( \frac{b^2}{y^2 + b^2} \right) \quad (11).$$

The linearized meridional momentum equation, Eqn. (8), may be rewritten as

$$\frac{1}{\rho_0} \frac{\partial p'}{\partial y} = - \left[ \left( U \frac{\partial}{\partial x} + V \frac{\partial}{\partial y} \right) v' + f u'_{jet} \right] \quad (12).$$

Substitution of Eqn. (10) into Eqn. (12), and setting  $V = 0$ , we obtain the result

$$p' (x, y, z = 0, t = 0) \approx - \rho_0 \left( \frac{U^2}{f} \frac{\partial^2}{\partial x^2} + f \right) \int_{y=-\infty}^y u'_{jet} dy \quad (13).$$

Using Eqn. (11) as a crude approximation to the actual initial zonal wind distribution, integration of the bell-shaped zonal wind anomaly yields a meridional structure dependency proportional to  $\tan^{-1} (y/b)$ . This is the reason for the apparent north-south homogeneity of the perturbation fields evidenced in the meridional wind and pressure perturbation fields indicated in Figs. 4a and 4b. The horizontal distribution of the potential temperature field is similar to that of the perturbation pressure, as required by the hydrostatic balance.

Figure 4c shows the horizontal cross sections of vertical velocity and the perturbation divergence on the  $z = -1$  km, and  $z = 0$  planes, respectively. Also presented are vertical cross sections of these fields on the  $y = 0$  plane at this time ( $t = 1$  hr). The horizontal structure of the vertical velocity field indicates rising (sinking) motion in the jet entrance (exit) region, whose structure can only be accounted for due to the alongstream variations associated with the balanced,

divergent zonal wind anomaly. This response is similar to the vertical motion field induced by the unbalanced, ageostrophic zonal wind anomaly presented in Section (a) (see Fig.1c). The perturbation divergence field in this case is also similar when compared to the unbalanced, ageostrophic case. Figure 4d shows horizontal cross sections of the perturbation relative vorticity and streamlines of the total wind field on the  $z = 0$  plane at this time, along with a vertical cross section of the relative vorticity perturbation on the  $y = 0$  plane. A cell of negative (anticyclonic) relative vorticity which is associated with the perturbation high pressure cell for  $y < 0$  dominates the response on the southern side of the main zonal wind anomaly at this time, and which is confined in the vertical to the initial source region of the jet. Due to the combination between the existence of the positive zonal wind perturbation, and the horizontal structure of the meridional wind perturbation (i.e.  $v' > 0$  for all  $x < 0$ , and  $v' < 0$  for all  $x > 0$ ), the streamlines of the total wind on the  $z = 0$  plane indicate the presence of a ridge on this plane. Figures 4e and 4f show the vertical cross sections on the  $x = 0$  plane at this time.

At later times (not shown), inertia-gravity waves are evident primarily in the vertical velocity and perturbation divergence fields, and propagate away from the initial source region, while the perturbation fields of zonal wind, meridional wind, pressure and potential temperature perturbations indicated in Figs. 4a-4f are advected downstream by the basic state barotropic current. These results seem to indicate that (at least for barotropic flows) zonal wind anomalies whose geometry or morphology is similar to Eqn. (4) or Eqn. (11) which satisfy a linear balance relationship given by Eqns. (7) and (8) will be predisposed to acquire an anticyclonic curvature. This type of response to this type of balanced initial state may help to explain the existence of some anticyclonically curved midlatitude jet streaks in regions where the constraint of barotropy is valid.

### **(c) The Forced Response of a Uniform Barotropic Flow to an Independently Propagating Zonal Wind Anomaly**

As can be seen from the preceeding paragraphs discussing the free response of a uniformly barotropic basic state current to either an unbalanced (ageostrophic) or balanced (geostrophic or inertial) zonal wind anomaly, it was found that no long-lived ageostrophic secondary circulations commonly associated with midlatitude jet streaks are produced. These circulations have traditionally been inferred through qualitative analysis of the *quasi-geostrophic* omega equation for a baroclinic atmosphere. In a baroclinic atmosphere, even in the absence of thermal (diabatic) and orographic forcings, these ageostrophic circulations are produced because *the basic state baroclinicity provides the physical mechanism* which forces the steady state vertical velocity which is required to compensate the divergence of the *ageostrophic* winds, thereby maintaining a *quasi-geostrophic* equilibrium, instead of the purely *geostrophic* equilibrium which is asymptotically approached in a barotropic atmosphere. Indeed, quasi-geostrophic vertical velocity equations for continuously stratified barotropic and baroclinic flows may be derived, and are given by

$$N^2 \nabla^2 w' + f^2 \frac{\partial^2 w'}{\partial z^2} = 0 \quad (14),$$

$$\nabla^2 w' + \frac{f^2}{N^2} \frac{\partial^2 w'}{\partial z^2} = \frac{2f}{N^2} \left( U_z \frac{\partial}{\partial x} + V_z \frac{\partial}{\partial y} \right) \left[ q' - \frac{f g}{\theta_0 N^2} \frac{\partial \theta'}{\partial z} \right] \quad (15).$$

respectively. It appears that the inhomogeneous forcing term in the baroclinic vertical motion equation (15) may be expressed in a variety of ways (e.g. Hoskins et al. 1987, Zehnder and Keyser, 1991, Holton, 1992), and is not necessarily limited to the form presented here. The form of Eqn (15). is a three-dimensional generalization of the two-dimensional baroclinic form presented by Zehnder and Keyser (1991). From this it can be seen that the vertical motion is forced by one of two physical mechanisms: (i) advection of the perturbation potential vorticity (PV) anomaly (i.e. jet streak) by the basic state thermal wind, and (ii) advection of the perturbation stratification by the basic state thermal wind. Although non-uniform PV anomalies ( $q'$ ) and perturbation stratifications ( $\partial \theta' / \partial z$ ) generally exist in continuously stratified barotropic flows, the horizontal temperature

gradient required for the existence of vertical shear of the basic state current (i.e. the thermal wind) doesn't.

Although the barotropic vertical motion equation, Eqn. (14), is homogeneous, and there is no physical mechanism which can be associated with the basic state which will generate *free* ageostrophic circulations as in a baroclinic atmosphere, note that jet streaks or zonal wind anomalies in the real atmosphere possess a propagation speed  $c$ , which is independent of the basic state current speed,  $U$ . Usually,  $c < U$ , although  $|u_{jet}| > |U|$  (Bluestein, 1986). Under normal circumstances, geostrophically balanced jet stream flow ( $U$ ) passing through the slower moving ( $c$ ) isotach maximum will generally experience strong acceleration as it enters the jet streak's entrance region and strong deceleration as it exits and leaves the jet streak's exit region. It is this alongstream variation of the geostrophic wind component associated with jet streaks in baroclinic atmospheres which provides the primary physical mechanism for the generation and maintenance of the thermally direct and indirect circulations (within the context of quasi-geostrophic theory). Therefore, it is useful to examine the response of a uniform barotropic current to an external momentum forcing which is taken to be representative of the external forcing which an independently propagating zonal wind anomaly exerts on the environmental flow in which it is embedded.

In general, we will examine two types of external momentum forcing:

$$F(x,y,z,t) = \frac{u'_{j0}}{\tau} e^{-\left[\frac{(x - ct)^2}{a_x^2} + \frac{y^2}{a_y^2} + \frac{z^2}{a_z^2}\right]} \quad (16),$$

$$F(x,y,z,t) = u_* \frac{\partial}{\partial x} \left\{ \frac{u_{j0}}{\left[\frac{(x - ct)^2}{a_x^2} + \frac{y^2}{a_y^2} + \frac{z^2}{a_z^2} + 1\right]^{3/2}} \right\} \quad (17).$$

The external forcing given by Eqn. (16) is chosen to investigate the response of a continuously stratified, uniform barotropic flow to an independently propagating Gaussian jet. Luo and Fritts

(1993) have investigated the response of a continuously stratified quiescent fluid to a Gaussian jet whose structural dependence is identical to that given in Eqn. (16), but instead of allowing the external momentum forcing to be temporally continuous as we do here, their temporal dependence was specified to be a Dirac delta function. We believe that our theory offers a better approach to understanding the forced geostrophic adjustment dynamics applicable to midlatitude jet streaks. The external momentum forcing given by Eqn. (17) is chosen to investigate the response of a continuously stratified, uniform barotropic flow to the entrance region accelerations and exit region decelerations forced by the alongstream variations or shear associated with an independently propagating zonal wind anomaly.

In order to formulate a mathematically tractable problem, we investigate the response in a frame of reference which is uniformly translating in the  $+x$ -direction at the zonal wind anomaly speed,  $c$ . Note that in this frame of reference, the magnitude of the uniform basic state barotropic current is  $U-c$ . In general, linear potential vorticity theory indicates that the response consists of (i) the excitation and propagation of an inertia-gravity wave radiation field, (ii) the generation of a PV anomaly (due to the external momentum forcing) which is then advected downstream from the forcing region by the basic state flow, and (iii) a steady response within the forcing region. An observer in a non-propagating reference frame (i.e. a frame with  $c = 0$ ) will see the steady state portion of the response uniformly propagate downstream at the zonal wind anomaly speed  $c$ . It is therefore this portion of the response which must be characteristic of the circulations commonly associated with midlatitude jet streaks, and is dependent upon the choice of the external momentum forcing. Note that (ii) implies that for a proper choice of external momentum forcing,  $F(x,y,z,t)$ , chosen to be representative of say, tropopause folding or the proper phasing of a ridge and trough associated with synoptic scale waves, the PV anomaly generated theoretically could be of the form of an *isolated zonal wind anomaly*. This model within the context of our theory may be used to investigate the physical mechanism of forced jetogenesis in a barotropic atmosphere.

Figure 5a shows the horizontal cross section of both the zonal and meridional wind perturbations on the  $z = 0$  plane as well as the vertical cross sections of these fields on the  $y = 0$

plane one hour after the external forcing given by Eqn. (16) is applied. The magnitude of the zonal wind anomaly  $u_0$  is specified to be 30 m/sec, the magnitude of the basic state barotropic flow is specified to be  $U = 20$  m/sec, and the propagation speed of the zonal wind anomaly is specified to be  $c = 10$  m/sec. All other parameters such as the horizontal and vertical scales of the wind anomaly are chosen to be the same as those used for the unbalanced zonal wind anomaly of Section (a). At this time ( $t = 1$  hr), a zonal wind anomaly of approximately 2 m/sec exists within the center of the forcing domain. A relatively weak southeastward directed meridional wind anomaly of approximately -0.26 m/sec exists at this time, with regions of weak northward directed meridional components flanking the main cell to the east and west.. Since  $\partial u'/\partial t = F$ , then once the nonzero zonal wind perturbation forms, the Coriolis force will act to produce a meridional component directed to the right of the zonal wind perturbation.

Figure 5b shows horizontal cross sections of the perturbation pressure and potential temperature perturbations on the planes  $z = 0$  and  $z = -1$  km, respectively. Vertical cross sections of these fields on the  $y = 0$  plane are also shown. Similar to the early stages of the free response to an unbalanced or ageostrophic zonal wind anomaly, both the pressure and potential temperature perturbations show a low-high or cold-warm dipole structure at this time. As was found for the early stages of the free response, the low-high couplet of perturbation pressure dominates the response within the initial forcing region, with reversed high-low couplets for  $z > 16$  km, and  $z < -16$  km. The vertical cross section of the potential temperature field indicates the hydrostatic balance which exists between the perturbation pressure and potential temperature fields. Figure 5c shows horizontal cross sections of the vertical velocity and perturbation divergence on the  $z = -1$  km and  $z = 0$  planes at this time, along with vertical cross sections of these fields on the  $y = 0$  plane. This figure can be compared with Fig. 1c, which shows markedly similar structural similarity with the free response at the same time. Figure 5d shows horizontal cross sections of the perturbation relative vorticity and perturbation streamlines of the induced flow, along with a vertical cross section of the perturbation relative vorticity on the  $y = 0$  plane. Similar to the free response, a region of cyclonic (anticyclonic) relative vorticity exists north (south) of the forced zonal wind

perturbation at this time, and is primarily confined to the forcing region. The induced flow on the plane  $z = 0$  indicates that the induced flow within the forcing region is dominated by the forced zonal wind perturbation, and is flanked by regions of cyclonic (anticyclonic) circulation north (south) of the zonal wind anomaly. No dramatic southerly deflection of the zonal flow is evident as was found in the free response, since the flow response here is dominated by the external momentum forcing. Figures 5e and 5f show the vertical cross sections of the response on the  $x = 0$  plane at this time (compare with Figs. 1e and 1f).

Figure 6a shows the horizontal cross sections of the forced zonal and meridional wind perturbations on the  $z = 0$  plane six hours after the external momentum forcing is applied. Vertical cross sections of these fields on the  $y = 0$  plane are also indicated. At this time, the magnitude of the zonal wind anomaly has increased from approximately 2 m/sec to 4.2 m/sec during the previous five hours. Weak compensating zonal counter currents ( $u' < 0$ ) of approximately 0.6 m/sec are located north and south of the forced zonal wind perturbation at this time. The meridional wind perturbation has strengthened to approximately -2.9 m/sec, and compensating northward directed components have formed in both the southwest and northeast quadrants of the forcing region, indicating the initial stages in the formation of confluence (diffuence) in the jet's entrance (exit) region. Vertical cross sections on the  $y = 0$  plane still indicate that the response is primarily confined to the forcing region. Figure 6b shows the horizontal cross sections of perturbation pressure and potential temperature on the  $z = 0$  and  $z = -1$  km planes at this time ( $t = 6$  hr). The magnitude of the pressure perturbation has increased dramatically from approximately 0.2 mb to 1.1 mb during the previous five hour period, and exhibits a clockwise or anticyclonic rotation around the point  $(x,y) = (0,0)$  on the  $z = 0$  plane as the mass field is forced to adjust to the strengthening zonal wind anomaly. The potential temperature perturbation indicates a region of adiabatic cooling in the forced jet's entrance region ( $x < 0$ ), and a region of adiabatic warming in the exit region. Vertical cross sections verify the existence of the hydrostatic balance between these fields. Figure 6c shows horizontal cross sections of the forced vertical motion and perturbation divergence on the  $z = -1$  km and  $z = 0$  planes, respectively. Vertical cross sections of these fields



on the plane  $y = 0$  are also presented. Forced vertical motion at this time ( $t = 6$  hr) indicates rising motion in the low pressure perturbation region which exists north of the zonal wind anomaly, and sinking motion in the high pressure perturbation region south of the zonal wind anomaly. Vertical cross sections on the  $y = 0$  plane indicate the structure of the forced inertia-gravity wave field at this time, which is due to the forced divergence associated with the formation of the zonal wind anomaly. Figure 6d shows the horizontal cross sections of perturbation relative vorticity and streamlines of the induced flow on the  $z = 0$  plane along with the vertical cross section of perturbation relative vorticity on the  $y = 0$  plane. The regions of cyclonic (anticyclonic) circulation which exist to the north (south) of the forced zonal wind anomaly have increased due to the strengthening of the pressure perturbation field as it adjusts in response to the forced zonal wind perturbation. Figures 6e and 6f show the vertical cross sections of the forced perturbations on the  $x = 0$  plane at this time.

Figure 7a shows the horizontal cross sections of the forced zonal and meridional wind perturbations on the  $z = 0$  plane at  $t = 12$  hrs. Also shown are vertical cross sections of the forced perturbations on the plane  $y = 0$  at this same time. The magnitude of the forced zonal wind perturbation has further increased from 4.2 m/sec to approximately 5.1 m/sec during the previous 6 hours, and the magnitudes of the compensating counter currents have increased to approximately -2.9 m/sec. The meridional wind perturbation has developed a four-cell structure at this time, indicating the development of a confluent region in the forced jet's entrance region, and a diffluent region in the jet's exit region. The vertical cross sections show that the response is still primarily confined to the forcing region. Figure 7b shows that the high-low dipole structure of the pressure perturbation has increased to a maximum value of 2.3 mb and deepened to a minimum value of -1.7 mb, and has rotated into a position whose meridional (north-south) gradient can balance and support the zonal wind perturbation which exists at this time. The horizontal and vertical structure of the perturbation potential temperature field at this time ( $t = 12$  hr) indicates the existence of a pool of cold air to the north of the zonal wind anomaly in the region of perturbation low pressure, while a pool of warm air resides to the south in the region of perturbation high pressure, indicative

of the hydrostatic balance which exists between these two fields. Figure 7c shows the horizontal cross sections of the forced vertical motion and perturbation divergence on the  $z = -1$  km and  $z = 0$  planes, respectively. Vertical cross sections on the plane  $y = 0$  are also shown. The forced vertical motion, although still indicative of the two-cell circulation of the previous six hour period, shows at this time ( $t = 12$  hr) that the cell of sinking motion is of greater magnitude than the cell of rising motion which exists north of the forced zonal wind perturbation, and that a relatively weaker cell of rising motion exists downstream of the jet core, roughly aligned with the jet axis. These features are indicators of the horizontal advection of the vertically propagating inertia-gravity modes as can be seen in the vertical cross sections on the  $y = 0$  plane. Note that in the region just below the  $z = 0$  km level that both the cells of negative and positive vertical motion which exist there are being advected downstream by the basic state barotropic current. The horizontal structure of the perturbation divergence field on the  $z = 0$  plane indicates that at this time convergence (divergence) exists in the forced wind anomaly's entrance (exit) region. Figure 7d shows the horizontal cross sections of the forced perturbation relative vorticity and streamlines of the induced flow on the  $z = 0$  plane, along with a vertical cross section of the perturbation relative vorticity on the  $y = 0$  plane. It can be seen that positive (cyclonic) relative vorticity and negative (anticyclonic) relative vorticity coincides with the low-high pressure perturbations which co-exist on the  $z = 0$  plane at this time. The vertical cross section indicates that the response is still primarily confined to the forcing region. Figures 8e and 8f show vertical cross sections of the forced perturbations on the  $x = 0$  plane.

By  $t = 48$  hours, (not shown) this zonal wind anomaly, which may be considered to be a PV anomaly, is clearly *being advected downstream by the basic state barotropic current*. This result indicates that while the external momentum forcing given by Eqn. (16) is dynamically adequate for the *genesis* of a localized zonal wind anomaly in a uniform barotropic flow, it is not adequate for a proper representation of the acceleration and subsequent deceleration which the environmental basic state flow experiences as it passes through a slower, independently propagating zonal wind anomaly. We believe that the first approximation to a better representation

of such physical processes will be obtained by investigation of the forced response associated with the external momentum forcing given by Eqn. (17), whose structure is specifically chosen to represent these proper alongstream variations.

In addition, based on recognition of the fact that the genesis and maintenance of the ageostrophic circulations in jet entrance and exit regions can be determined from quasi-geostrophic dynamics, the natural extension of our work to baroclinic flows should necessarily proceed along these lines. Although the physical mechanisms responsible for the generation of inertia-gravity modes will be excluded within the framework of a quasi-geostrophic theory, the thermally direct and indirect circulations can be obtained. In this way, we will be able to develop a linear quasi-geostrophic theory for a propagating jet streak. The theory will then be applied to an investigation of the role which jet streaks play as upper level forcing mechanisms in idealized models of lee (Smith, 1984, 1986) and coastal (Lin, 1989, 1990) cyclogenesis.

## References

- Bluestein, H. B., 1986: Fronts and Jet Streaks: A theoretical perspective. *Mesoscale Meteorology and Forecasting*. P. S. Ray, ed., Amer. Meteor. Soc., Boston, 793 pp.
- Blumen, W., 1972: Geostrophic adjustment. *Rev. Geophys. Space Phys.*, **10**, 485-528.
- Bolin, B., 1953: The adjustment of a non-balanced velocity field toward geostrophic equilibrium in a stratified fluid. *Tellus*, **5**, 373-385.
- Chan, A., 1945: An investigation of the free oscillations of a simple current system. *J. Meteor.*, **2**, 113-119.
- Duffy, D. G., 1990: Geostrophic adjustment in a baroclinic atmosphere. *J. Atmos. Sci.*, **47**, 457-473.
- Fritts, D. C., and Z. Luo, 1992: Gravity wave excitation by geostrophic adjustment of the jet stream. Part I: Two-dimensional forcing. *J. Atmos. Sci.*, **49**, 681-697.
- Holton, J. R., 1992: An introduction to dynamic meteorology. 3rd ed., Academic Press, 511 pp.

- Hoskins, B. J., Draghici, I., and Davies, H. C., 1978: A new look at the  $\omega$ -equation. *Quart. J. Roy. Meteor. Soc.*, **111**, 877- 946.
- Lin, Y.-L., 1989: A theory of cyclogenesis forced by diabatic heating. Part I: A Quasi-geostrophic approach. *J. Atmos. Sci.*, **46**, 3015-3036.
- Lin, Y.-L., 1990: A theory of cyclogenesis forced by diabatic heating. Part II: A Semigeostrophic approach. *J. Atmos. Sci.*, **47**, 1755-1777.
- Luo, Z., and D. C. Fritts, 1993: Gravity wave excitation by geostrophic adjustment of the jet stream. Part II: Three-dimensional forcing. *J. Atmos. Sci.*, **50**, 104-115.
- Rossby, C. G., 1938: On the mutual adjustment of pressure and velocity distributions in simple current systems, II. *J. Mar. Res.*, **1**, 239-263.
- Smith, R. B., 1984: A theory of lee cyclogenesis. *J. Atmos. Sci.*, **41**, 1159-1168.
- Smith, R. B., 1986: Further development of a theory of lee cyclogenesis. *J. Atmos. Sci.*, **43**, 1582-1602.
- Walterscheid, R. L., and D. J. Boucher, Jr., 1984: A simple model of the transient response of the thermosphere to impulsive forcing. *J. Atmos. Sci.*, **41**, 1062-1072.
- Zehnder, J. A., and D. Keyser, 1991: The influence of interior gradients of potential vorticity on rapid cyclogenesis. *Tellus*, **43A**, 198-211.
- Zhu, X., and J. R. Holton, 1987: Mean fields induced by local gravity-wave forcing in the middle atmosphere. *J. Atmos. Sci.*, **44**, 620-630.

## List of Figures

Figure 1a: Horizontal and vertical cross sections of the total zonal and meridional wind perturbations on the  $z = 0$  and  $y = 0$  planes respectively, one hour after the introduction of an unbalanced (ageostrophic) zonal wind anomaly (whose geometry is given by Eqn. (4)) is introduced into an unbounded quiescent, continuously stratified, rotating, uniformly barotropic Boussinesq atmosphere. The parameters associated with the basic state flow and initial

ageostrophic wind anomaly are:  $U = V = 0$ ,  $N = 0.01 \text{ sec}^{-1}$ ,  $f = 0.0001 \text{ sec}^{-1}$ ,  $\theta_0 = 273 \text{ K}$ ,  $u_{j0} = 10 \text{ m/sec}$ ,  $a = b = 500 \text{ km}$ ,  $c = 5 \text{ km}$ .

Figure 1b: Horizontal and vertical cross sections of the perturbation pressure and potential temperature fields on the  $z = 0$ ,  $z = -1 \text{ km}$ , and  $y = 0$  planes, respectively, one hour after the introduction of an unbalanced (ageostrophic) zonal wind anomaly is introduced into a quiescent, continuously stratified, rotating, uniformly barotropic Boussinesq atmosphere.

Figure 1c: Horizontal and vertical cross sections of the vertical velocity and perturbation divergence fields on the  $z = -1 \text{ km}$ ,  $z = 0$ , any  $y = 0$  planes at  $t = 1 \text{ hr}$ .

Figure 1d: Horizontal and vertical cross section of the perturbation relative vorticity field on the  $z = 0$  and  $y = 0$  planes at  $t = 1 \text{ hr}$ . Also shown are streamlines of the induced perturbation flow ( $u'$ ,  $v'$ ) on the  $z = 0$  plane at the same time.

Figure 1e: Vertical cross sections of the total zonal and meridional wind perturbations, along with the vertical velocity and pressure perturbation fields on the  $x = 0$  plane at  $t = 1 \text{ hr}$ .

Figure 1f: Vertical cross sections of the perturbation potential temperature, divergence, and relative vorticity fields on the  $x = 0$  plane at  $t = 1 \text{ hr}$ .

Figure 2a: Same as Figure 1a, but at  $t = 3 \text{ hr}$ .

Figure 2b: Same as Figure 1b, but at  $t = 3 \text{ hr}$ .

Figure 2c: Same as Figure 1c, but at  $t = 3 \text{ hr}$ .

Figure 2d: Same as Figure 1d, but at  $t = 3 \text{ hr}$ .

Figure 2e: Same as Figure 1e: but at  $t = 3 \text{ hr}$ .

Figure 2f: Same as Figure 1f, but at  $t = 3 \text{ hr}$ .

Figure 3a: Horizontal cross sections of the steady state (geostrophic, non-divergent) total zonal and meridional wind perturbations on the  $z = 0$  plane. Also shown is the vertical cross section of the steady state zonal wind anomaly on the  $y = 0$  plane. With the addition of a non-zero basic state barotropic current, this potential vorticity (PV) anomaly is advected downstream from the initial source region.

Figure 3b: Horizontal cross sections of the steady state perturbation pressure, potential temperature, relative vorticity, and streamlines of induced perturbation flow on the  $z = 0$  and  $z = -1$  km planes.

Figure 3c: Vertical cross sections of the steady state perturbation zonal wind, pressure, potential temperature, and relative vorticity fields on the  $x = 0$  plane. Hydrostatic balance between the perturbation pressure and potential temperature fields is evident.

Figure 4a: Horizontal and vertical cross sections of the total zonal wind ( $u = U + u'$ ) and perturbation meridional wind ( $v'$ ) on the  $z = 0$  and  $y = 0$  planes at  $t = 1$  hr for an initially inertially balanced zonal wind anomaly. The magnitude of the basic state current is  $U = 10$  m/sec. Other flow field parameters are the same as indicated in Figure 1a. This balanced state is advected downstream at later times by the barotropic current.

Figure 4b: Same as Figure 1b except for an inertially balanced initial state. Note that the total potential temperature field ( $\theta = \theta_0 + \theta'$ ) is plotted.

Figure 4c: Same as Figure 1c except for an inertially balanced initial state.

Figure 4d: Same as Figure 1d except for an inertially balanced initial state. Note that streamlines for the total flow ( $u = U + u'$ ,  $v'$ ) are plotted. Due to the predominance of perturbation high pressure, the flow field at this time exhibits strong anticyclonic curvature.

Figure 4e: Same as Figure 1e except for an inertially balanced initial state.

Figure 4f: Same as Figure 1f except for an inertially balanced initial state. Note that the total potential temperature field is plotted.

Figure 5a: Horizontal and vertical cross sections of the forced response of a uniform barotropic flow to the external momentum forcing given by Eqn. (16) on the  $z = 0$  and  $y = 0$  planes as seen by an observer in a frame of reference uniformly propagating at the zonal wind anomaly speed  $c$  one hour after the forcing is applied. Note that the magnitude of the basic state flow in this frame is  $U - c$ . The magnitude of the zonal wind anomaly is  $u_j0 = 30$  m/sec, the barotropic current value is  $U = 20$  m/sec, and the propagation speed of the jet is taken to be  $c = 10$  m/sec. Other parameters are the same as indicated in Figure 1a. The time scale  $\tau$  is chosen to be

$a_X/(U-c)$ , which represents the time required for an air parcel of the environmental flow in which the zonal wind anomaly is embedded to pass through the isotach maximum.

Figure 5b: Same as Figure 1b, but for the forced response.

Figure 5c: Same as Figure 1c, but for the forced response.

Figure 5d: Same as Figure 1d, but for the forced response.

Figure 5e: Same as Figure 1e, but for the forced response.

Figure 5f: Same as Figure 1f, but for the forced response.

Figure 6a: Same as Figure 5a, but at  $t = 6$  hr.

Figure 6b: Same as Figure 5b, but at  $t = 6$  hr.

Figure 6c: Same as Figure 5c, but at  $t = 6$  hr.

Figure 6d: Same as Figure 5d, but at  $t = 6$  hr.

Figure 6e: Same as Figure 5e, but at  $t = 6$  hr.

Figure 6f: Same as Figure 5f, but at  $t = 6$  hr.

Figure 7a: Same as Figure 5a, but at  $t = 12$  hr.

Figure 7b: Same as Figure 5b, but at  $t = 12$  hr.

Figure 7c: Same as Figure 5c, but at  $t = 12$  hr.

Figure 7d: Same as Figure 5d, but at  $t = 12$  hr.

Figure 7e: Same as Figure 5e, but at  $t = 12$  hr.

Figure 7f: Same as Figure 5f, but at  $t = 12$  hr.

## **Appendix A Derivation of the Dispersion Relationship and Components of the Phase Speeds and Group Velocities for Three-Dimensional Linear Plane Waves Excited in a Uniform Barotropic Flow**

The linearized continuum field equations may be combined to yield the following wave equation governing the free response of small amplitude perturbations excited in a rotating, continuously stratified, uniformly barotropic Boussinesq flow:

$$L \phi = 0 \quad (A1),$$

where  $\phi$  may be any one of the dynamical variables  $u'$ ,  $v'$ ,  $w'$ ,  $p'$ , or  $\theta'$ , and  $L$  is a linear differential operator defined by

$$L = \frac{D}{Dt} \left[ \left( \frac{D^2}{Dt^2} + f^2 \right) \frac{\partial^2}{\partial z^2} + N^2 \nabla^2 \right] \quad (A2),$$

where  $D/Dt$  is the material derivative  $D/Dt = \partial/\partial t + U \partial/\partial x + V \partial/\partial y$ . We assume that three-dimensional linear plane waves of the form

$$\phi(x, y, z, t) = \phi_0 e^{i[kx + ly + mz - \omega t]} \quad (A3)$$

satisfy the wave equation (A1). Substitution of (A3) into (A1) yields the dispersion relationship

$$\omega = (kU + lV) \pm \sqrt{\frac{N^2 (k^2 + l^2)}{m^2} + f^2} \quad (A4),$$

The horizontal ( $c_{px}$  and  $c_{py}$ ) and vertical ( $c_{pz}$ ) components of the propagation phase speed for these free internal inertia-gravity waves are given by

$$c_{px} = \frac{(kU + lV)}{k} \pm \frac{1}{k} \sqrt{\frac{N^2 (k^2 + l^2)}{m^2} + f^2} \quad (A5),$$

$$c_{py} = \frac{(kU + lV)}{l} \pm \frac{1}{l} \sqrt{\frac{N^2 (k^2 + l^2)}{m^2} + f^2} \quad (A6),$$

$$c_{pz} = \frac{(kU + lV)}{m} \pm \frac{1}{m} \sqrt{\frac{N^2 (k^2 + l^2)}{m^2} + f^2} \quad (A7).$$



The horizontal ( $c_{gx}$  and  $c_{gy}$ ) and vertical ( $c_{gz}$ ) components of the group velocity vector at which the inertia-gravity wave energy propagates are given by (positive root):

$$c_{gx} = \frac{\partial \omega}{\partial k} = U + \frac{k N^2}{m^2 \sqrt{\frac{N^2 (k^2 + l^2)}{m^2} + f^2}} \quad (\text{A8}),$$

$$c_{gy} = \frac{\partial \omega}{\partial l} = V + \frac{l N^2}{m^2 \sqrt{\frac{N^2 (k^2 + l^2)}{m^2} + f^2}} \quad (\text{A9}),$$

$$c_{gz} = \frac{\partial \omega}{\partial m} = \frac{-N^2 (k^2 + l^2)}{m^3 \sqrt{\frac{N^2 (k^2 + l^2)}{m^2} + f^2}} \quad (\text{A10}).$$

There exists a Rossby deformation for each baroclinic mode, which is given by

$$L_R = \frac{N L_z}{2 \pi f}, \text{ where } m = \frac{2 \pi}{L_z} \quad (\text{A11}).$$

The primary internal modes to be excited for a zonal wind anomaly whose horizontal scales are  $a_x$  and  $a_y$ , and whose vertical depth is  $D$  will be  $k = 2\pi/a_x$ ,  $l = 2\pi/a_y$ , and  $m = 2\pi/D$ . The steady state geostrophic equilibrium solution will be confined to the deformation radius  $ND/(2\pi f)$ .

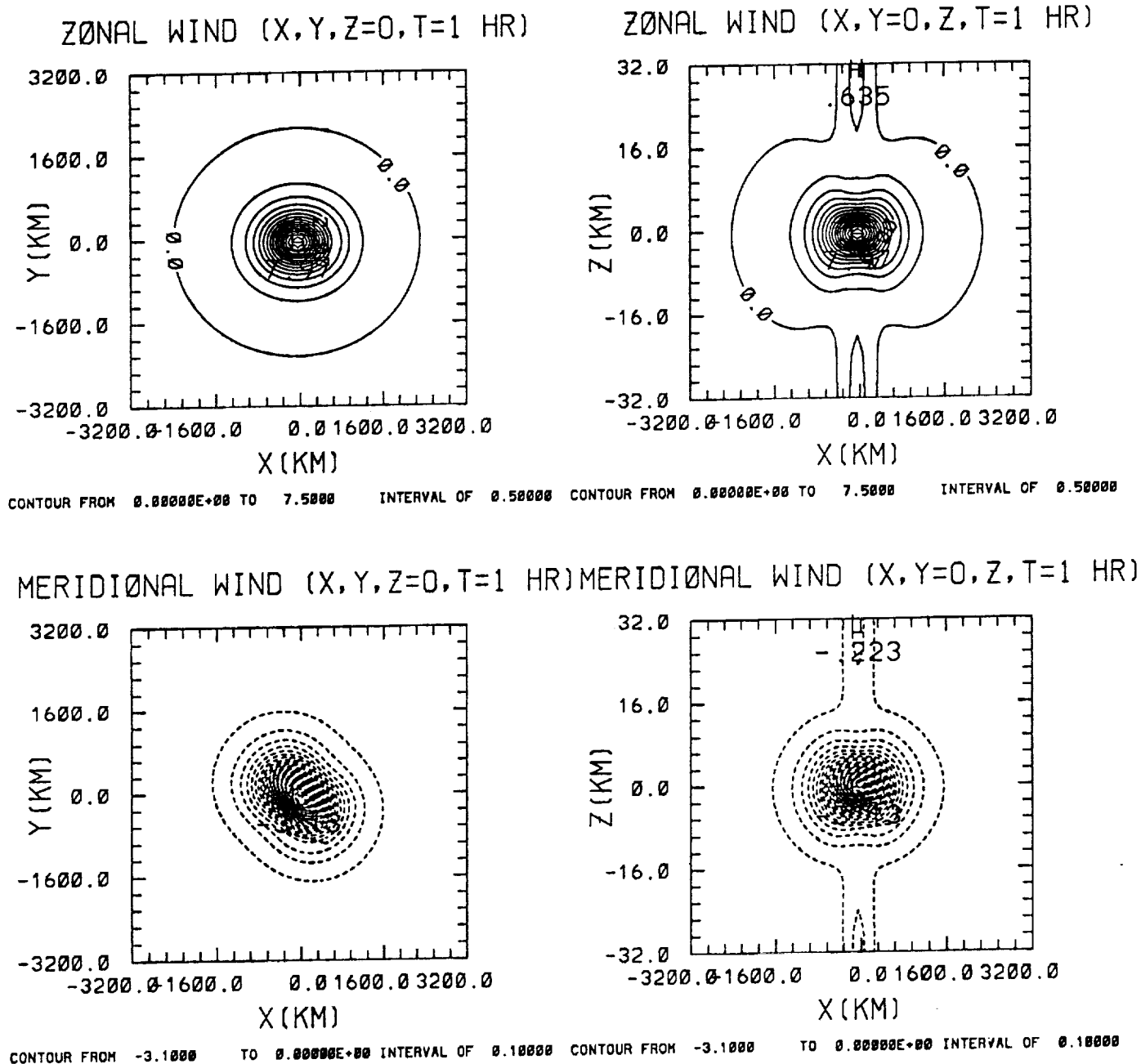
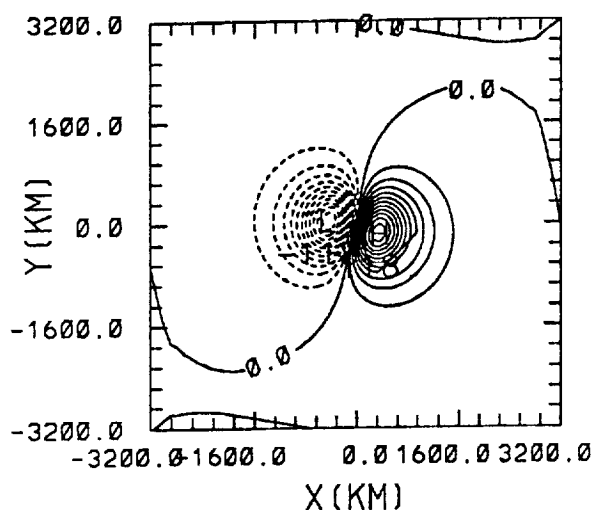
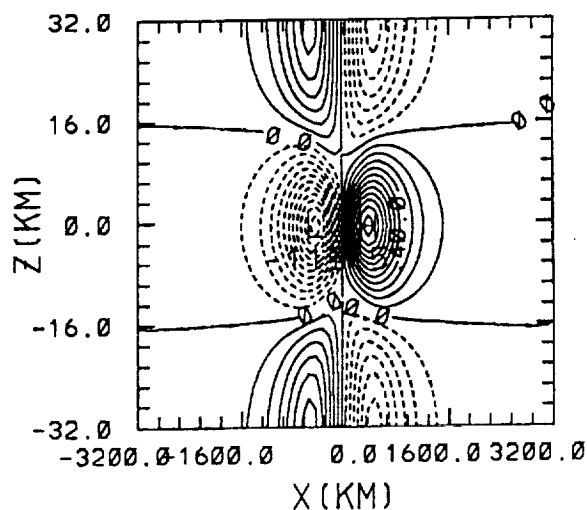


Figure 1 a

PRESSURE (X,Y,Z=0,T=1 HR)

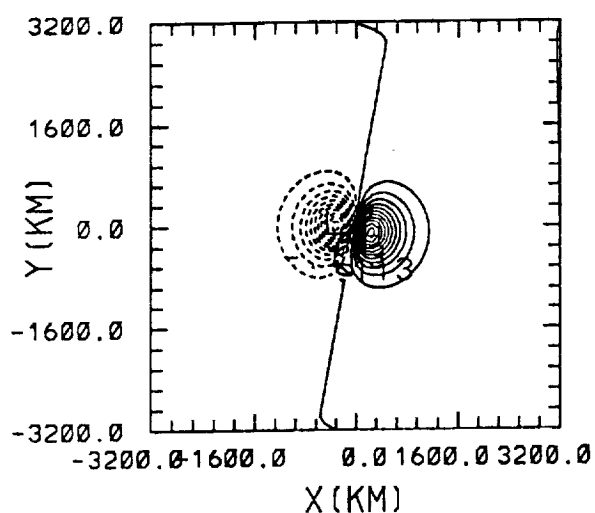


PRESSURE (X,Y=0,Z,T=1 HR)

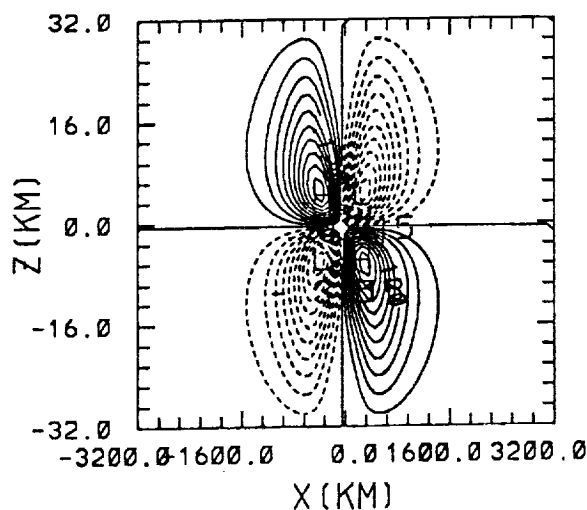


CONTOUR FROM -110.00 TO 110.00 INTERVAL OF 10.000 CONTOUR FROM -110.00 TO 110.00 INTERVAL OF 10.000

THETA (X,Y,Z=-1 KM,T=1 HR)

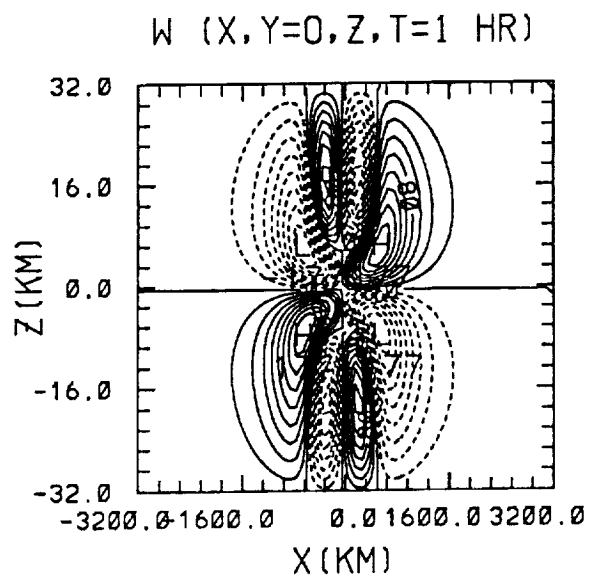
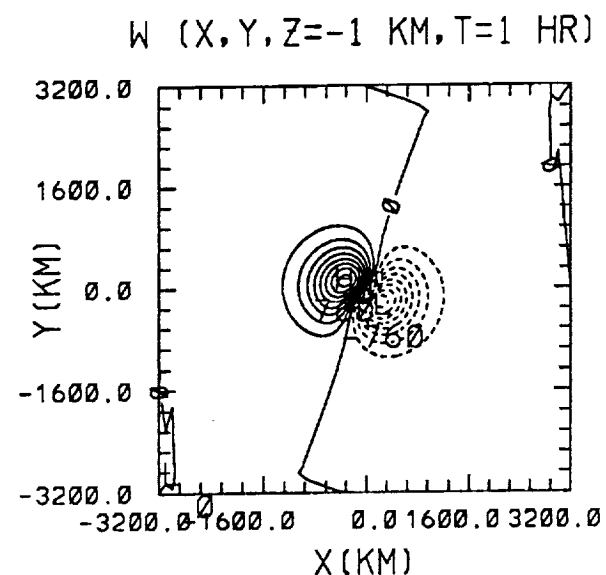


THETA (X,Y=0,Z,T=1 HR)

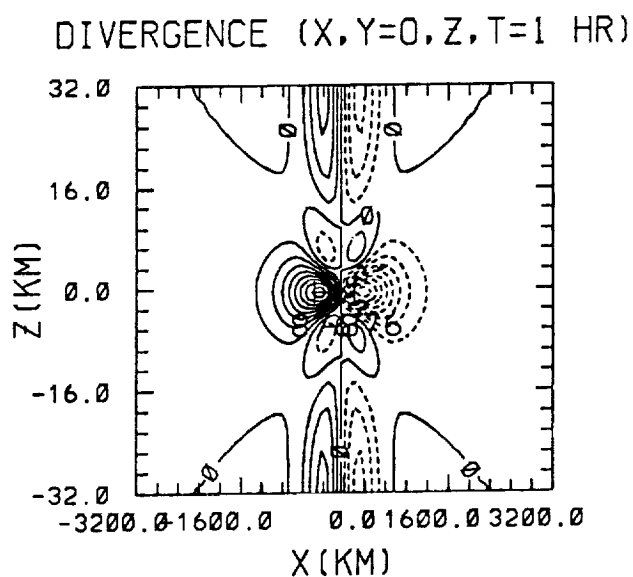
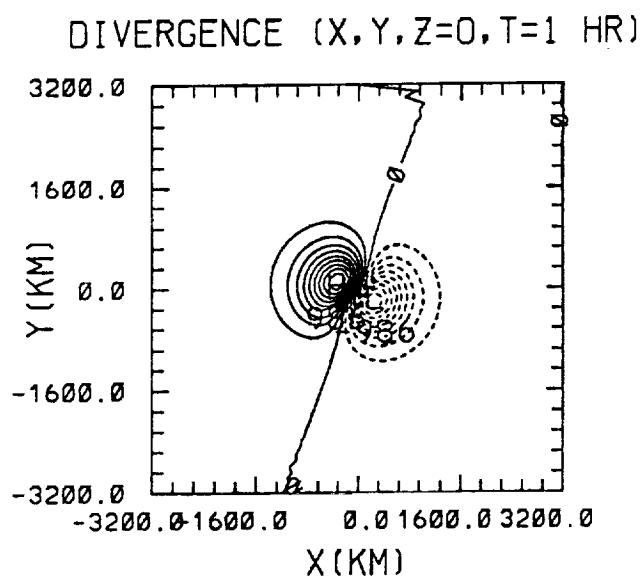


CONTOUR FROM -0.11000 TO 0.11000 INTERVAL OF 0.10000E-00 CONTOUR FROM -0.30000 TO 0.30000 INTERVAL OF 0.30000E-01

Figure 1 b



CONTOUR FROM  $-0.72000E-02$  TO  $0.72000E-02$  INTERVAL OF  $0.90000E-03$  CONTOUR FROM  $-0.16000E-01$  TO  $0.16000E-01$  INTERVAL OF  $0.20000E-02$



CONTOUR FROM  $-0.90000E-05$  TO  $0.90000E-05$  INTERVAL OF  $0.10000E-05$  CONTOUR FROM  $-0.80000E-05$  TO  $0.80000E-05$  INTERVAL OF  $0.10000E-05$

Figure 1 c

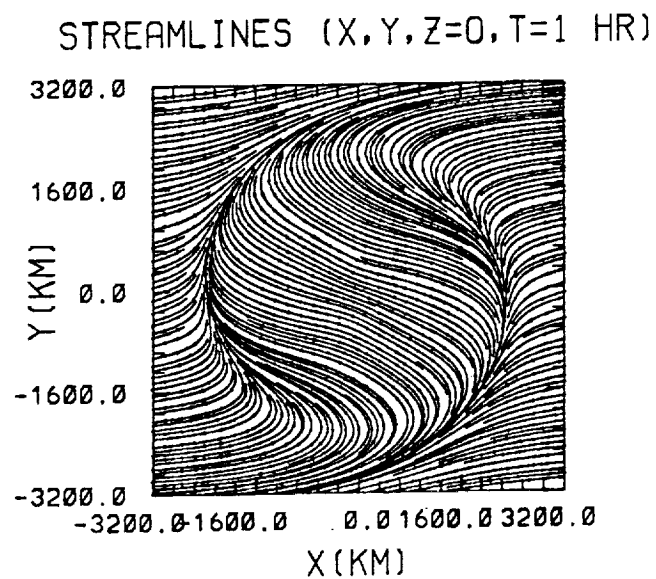
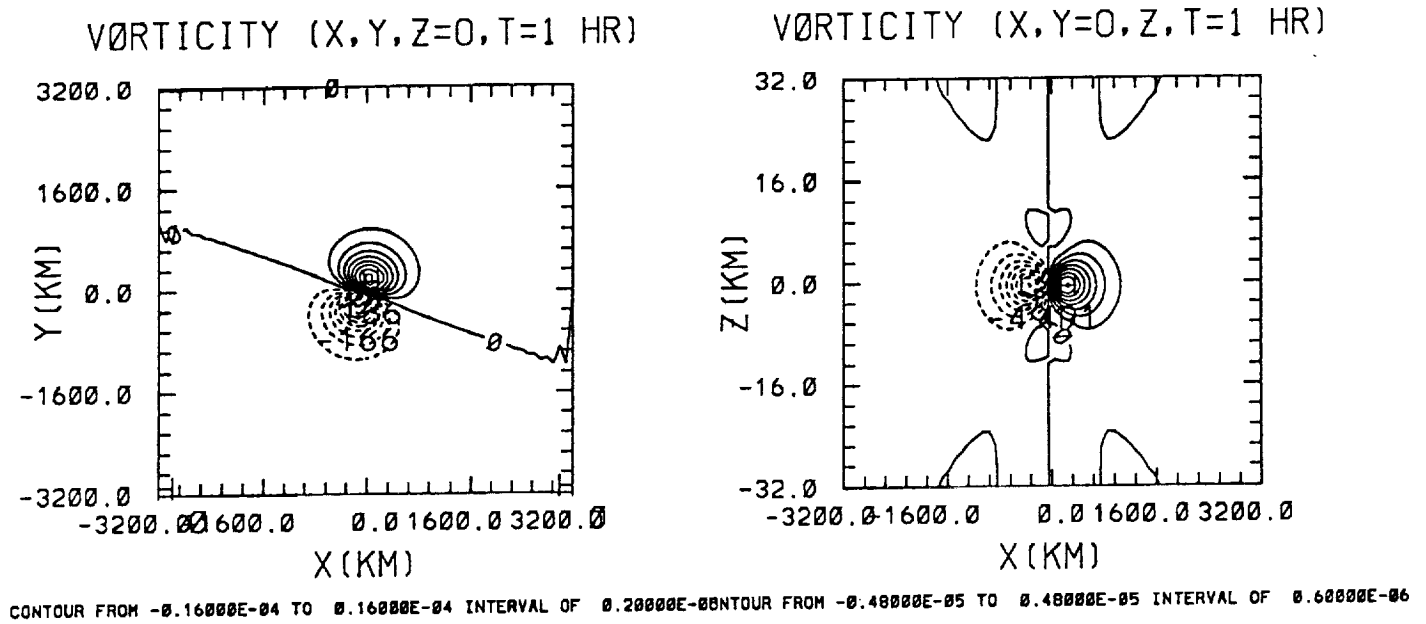


Figure 1 d

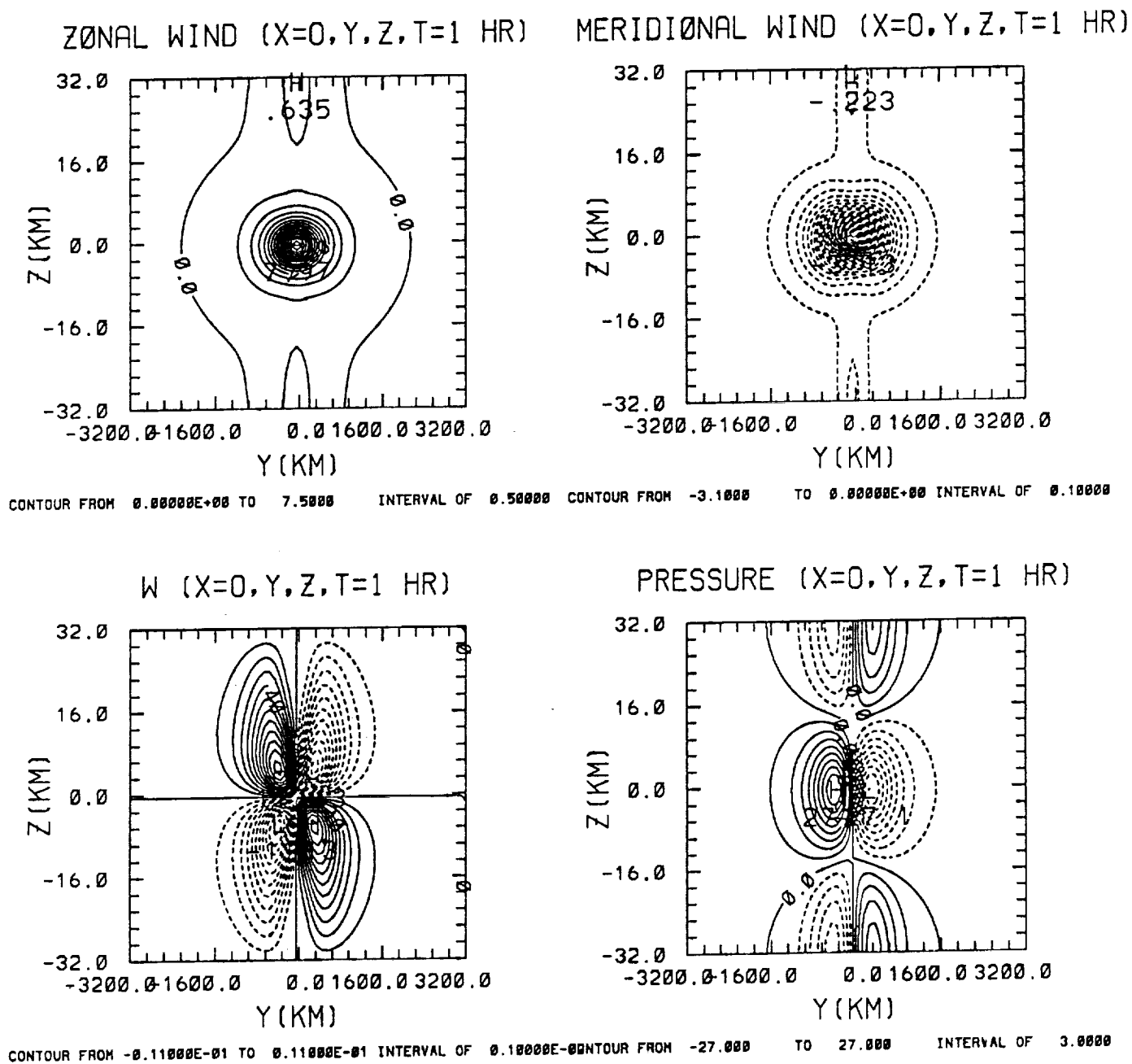
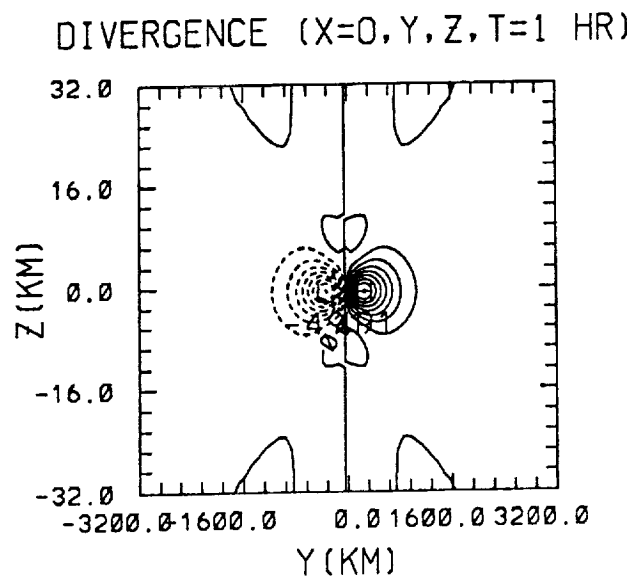
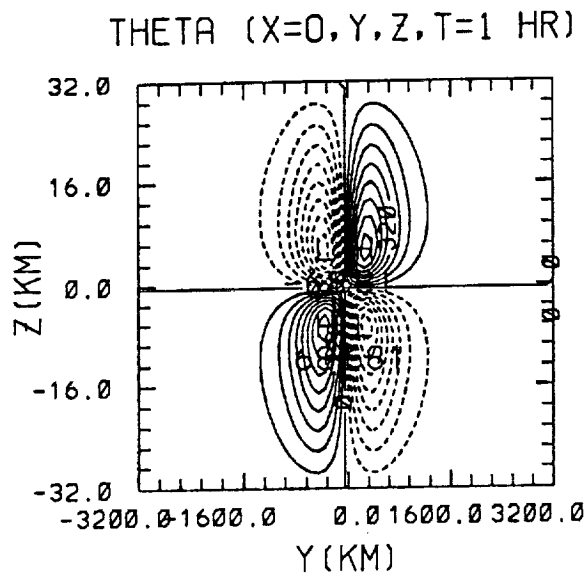
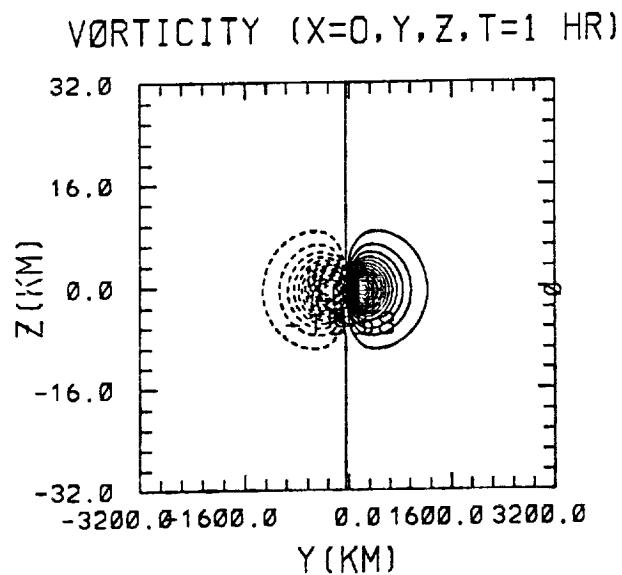


Figure 1 e



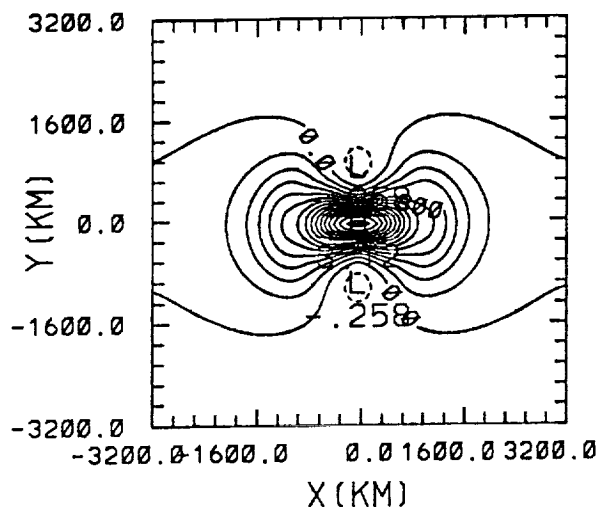
CONTOUR FROM  $-0.64000E-01$  TO  $0.64000E-01$  INTERVAL OF  $0.80000E-02$  CONTOUR FROM  $-0.48000E-05$  TO  $0.48000E-05$  INTERVAL OF  $0.60000E-06$



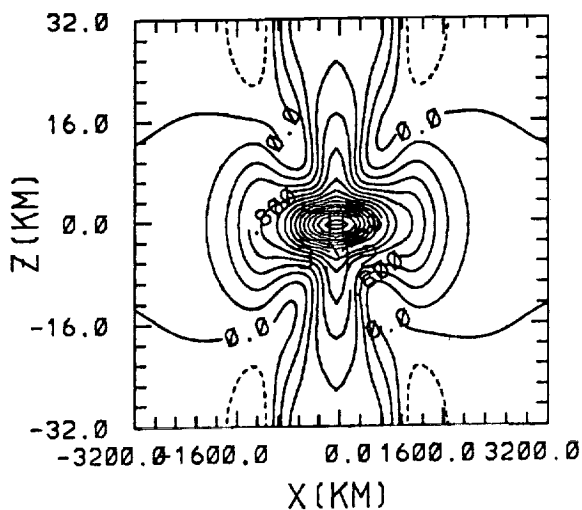
CONTOUR FROM  $-0.15000E-04$  TO  $0.15000E-04$  INTERVAL OF  $0.10000E-05$

Figure 1 f

ZONAL WIND (X,Y,Z=0,T=3 HR)

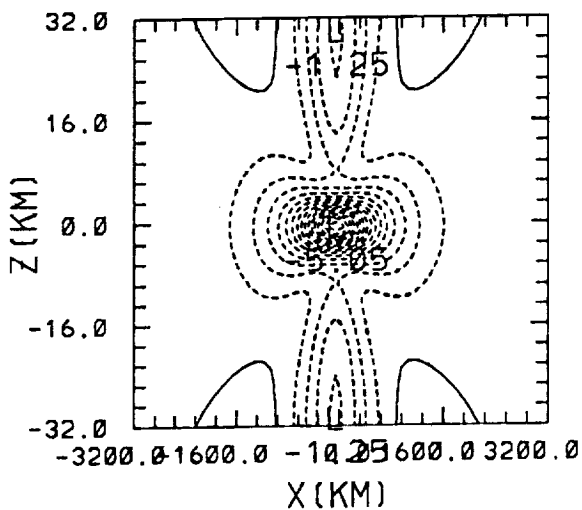
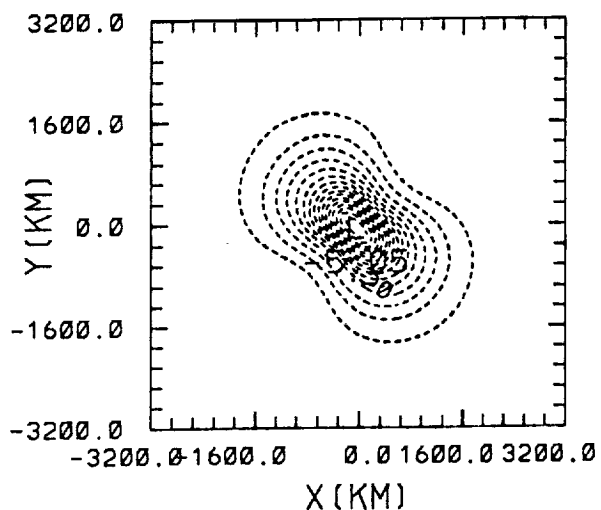


ZONAL WIND (X,Y=0,Z,T=3 HR)



CONTOUR FROM -0.20000 TO 3.0000 INTERVAL OF 0.20000 CONTOUR FROM -0.20000 TO 3.0000 INTERVAL OF 0.20000

MERIDIONAL WIND (X,Y,Z=0,T=3 HR) MERIDIONAL WIND (X,Y=0,Z,T=3 HR)



CONTOUR FROM -4.0000 TO 0.0000E+00 INTERVAL OF 0.30000 CONTOUR FROM -4.0000 TO 0.0000E+00 INTERVAL OF 0.30000

Figure 2 a



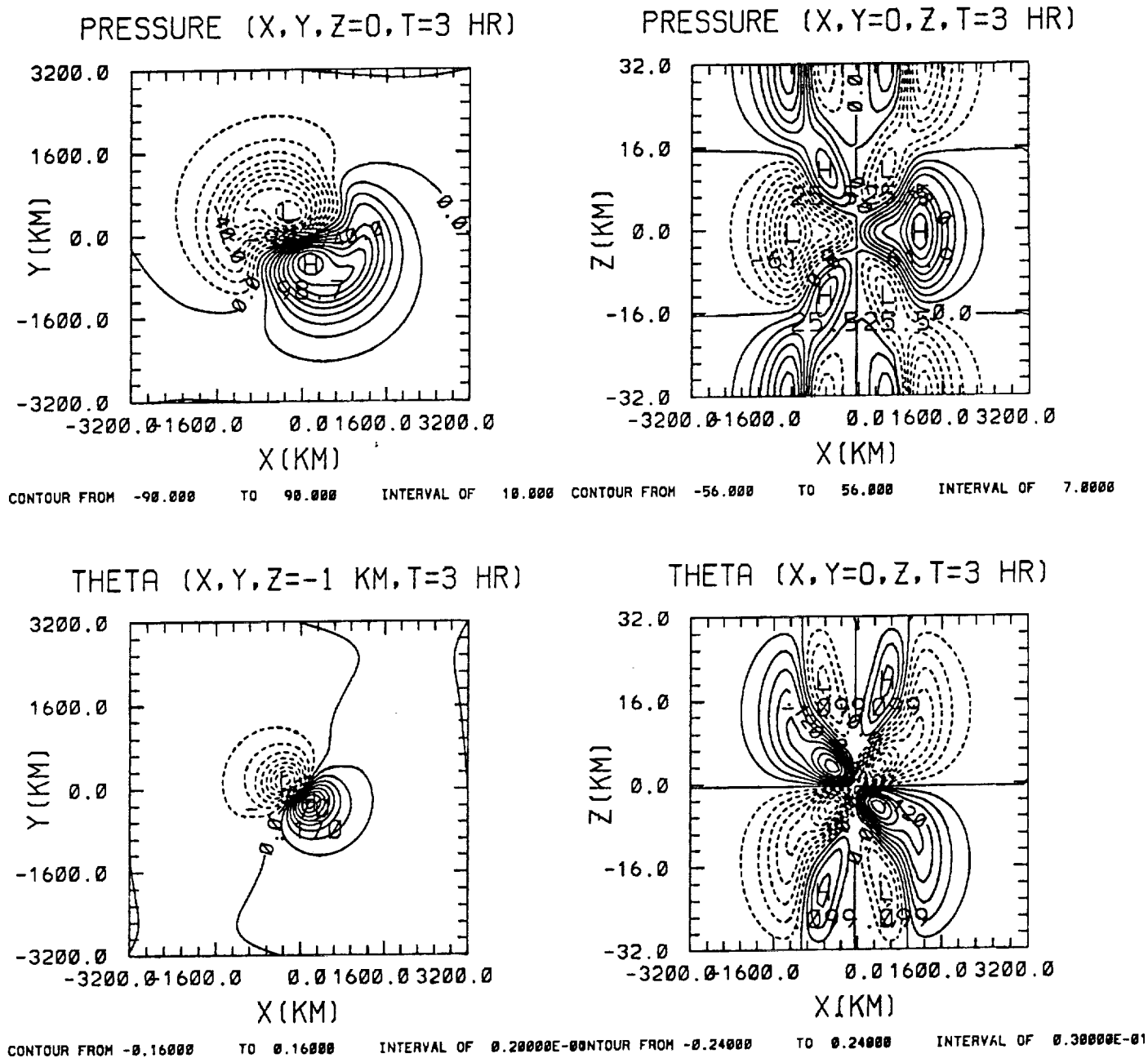
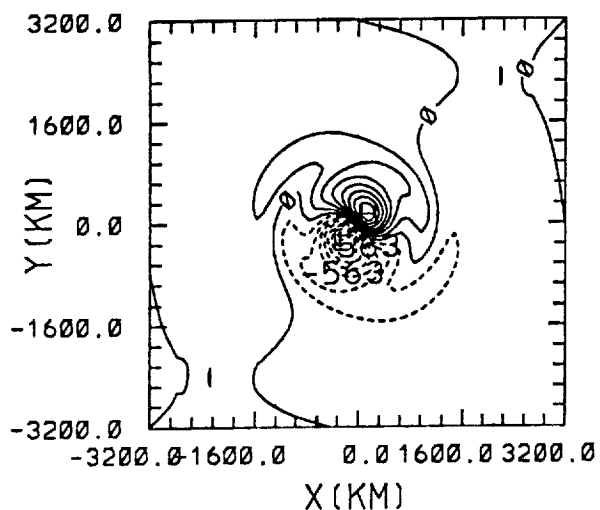
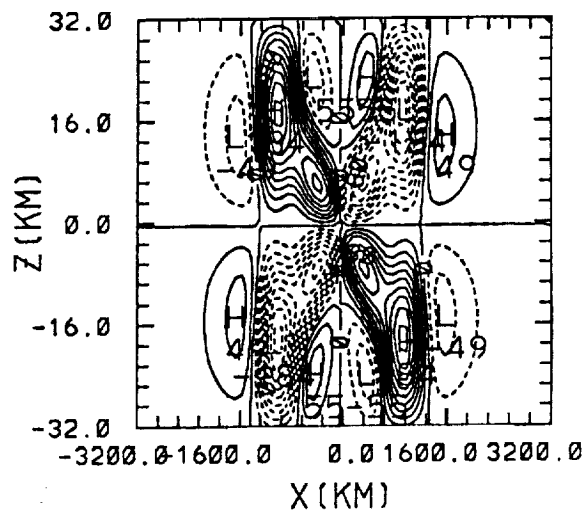


Figure 2 b

W (X,Y,Z=-1 KM,T=3 HR)

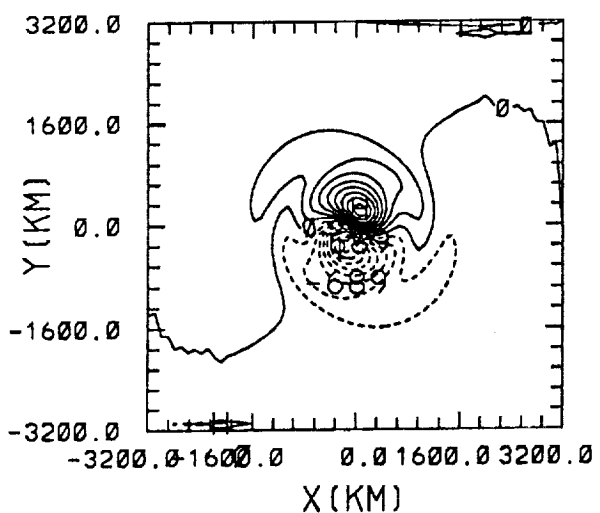


W (X,Y=0,Z,T=3 HR)

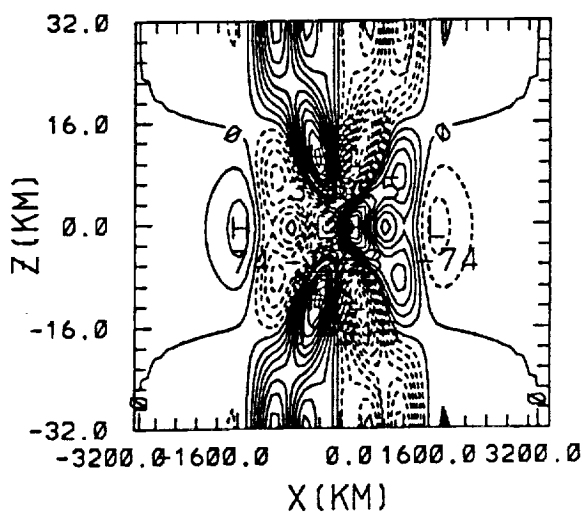


CONTOUR FROM -0.56000E-02 TO 0.56000E-02 INTERVAL OF 0.70000E-03 CONTOUR FROM -0.18000E-01 TO 0.18000E-01 INTERVAL OF 0.20000E-02

DIVERGENCE (X,Y,Z=0,T=3 HR)



DIVERGENCE (X,Y=0,Z,T=3 HR)



CONTOUR FROM -0.64000E-05 TO 0.64000E-05 INTERVAL OF 0.80000E-06 CONTOUR FROM -0.30000E-05 TO 0.30000E-05 INTERVAL OF 0.30000E-06

Figure 2 c

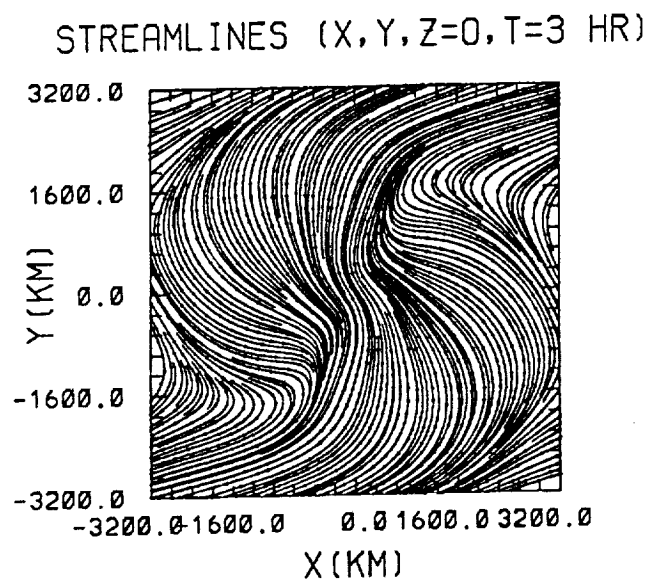
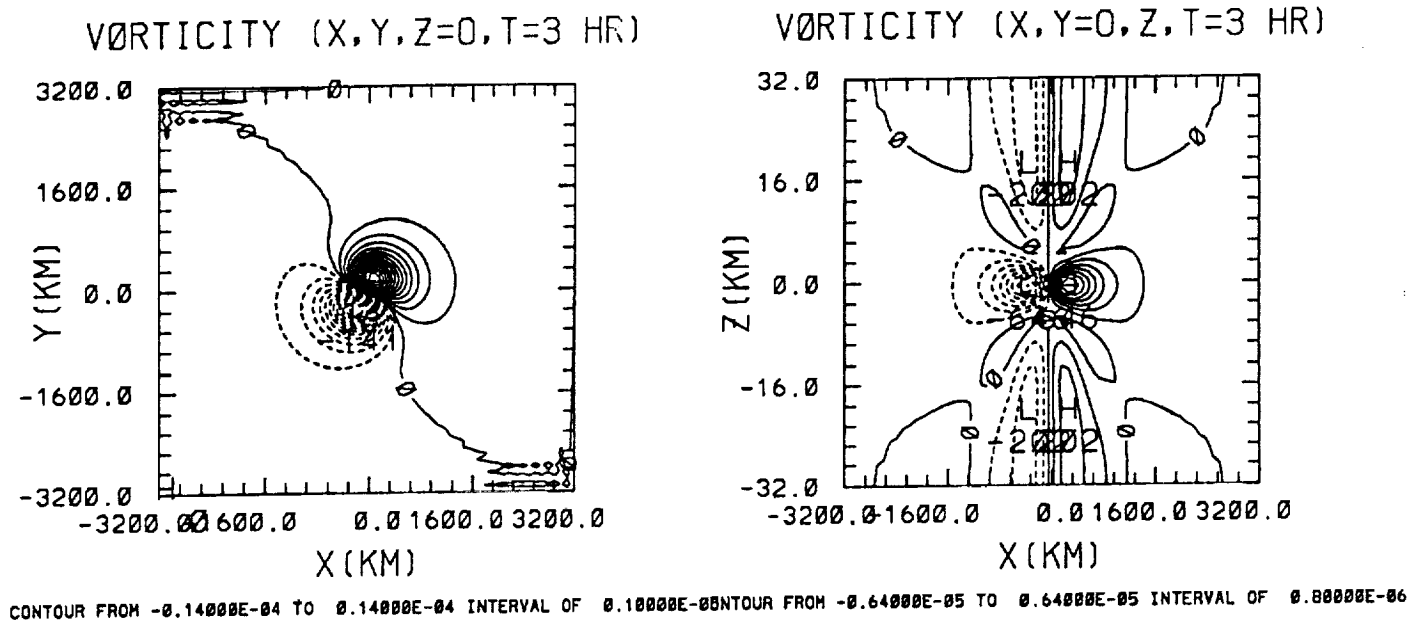
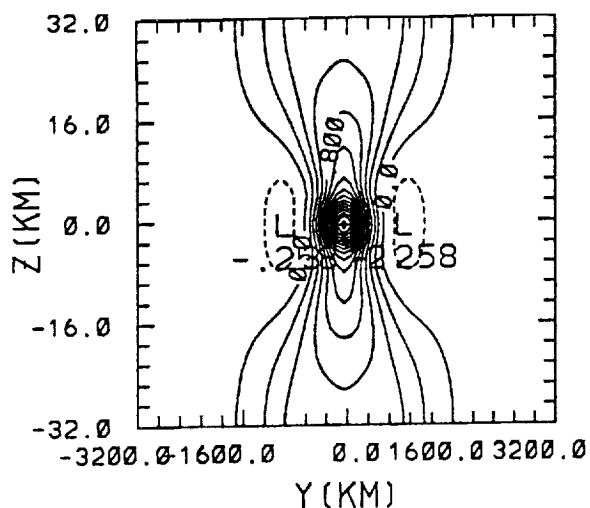
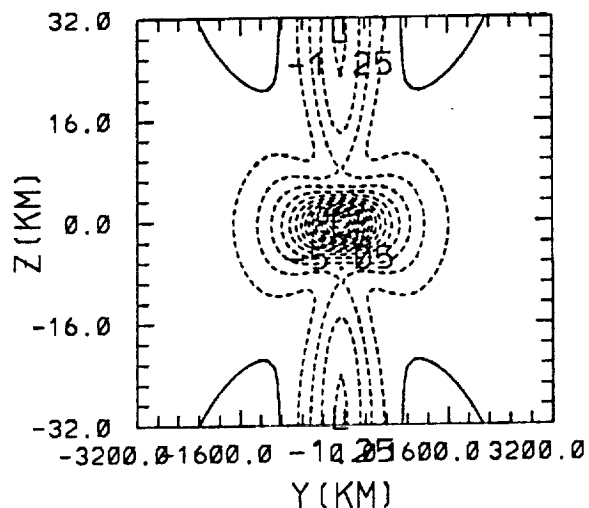


Figure 2 d

ZONAL WIND (X=0,Y,Z,T=3 HR)

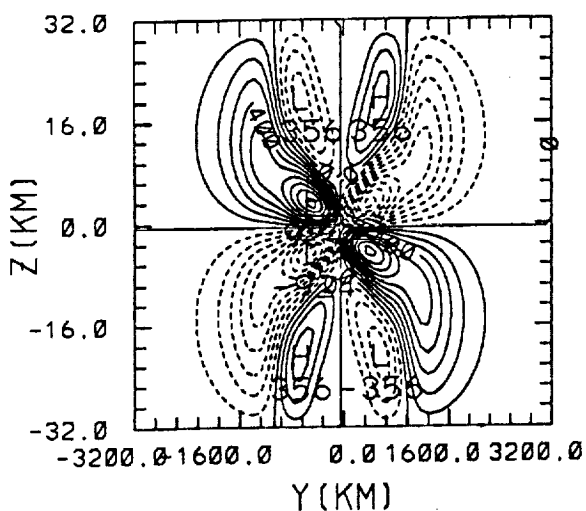


MERIDIONAL WIND (X=0,Y,Z,T=3 HR)

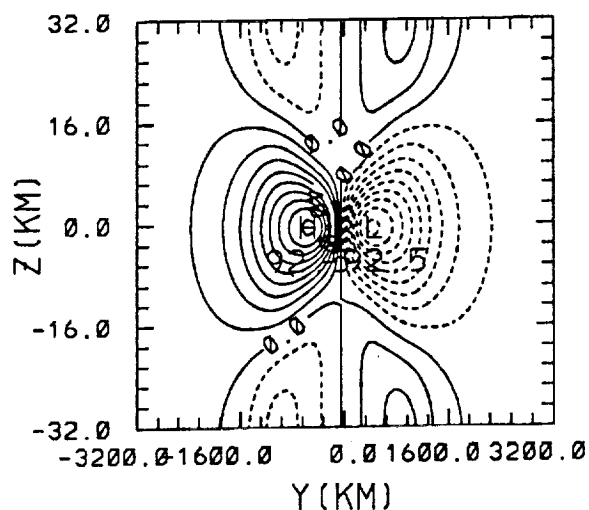


CONTOUR FROM -0.20000 TO 3.0000 INTERVAL OF 0.20000 CONTOUR FROM -4.8000 TO 0.8000E+00 INTERVAL OF 0.30000

W (X=0,Y,Z,T=3 HR)



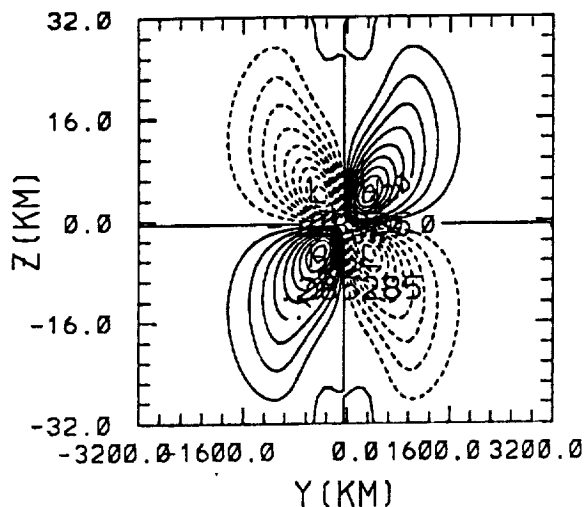
PRESSURE (X=0,Y,Z,T=3 HR)



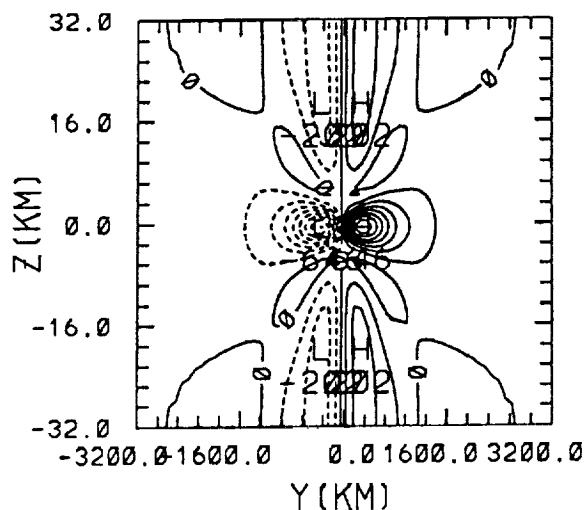
CONTOUR FROM -0.90000E-02 TO 0.90000E-02 INTERVAL OF 0.10000E-02 CONTOUR FROM -90.000 TO 90.000 INTERVAL OF 10.000

Figure 2 e

THETA (X=0,Y,Z,T=3 HR)

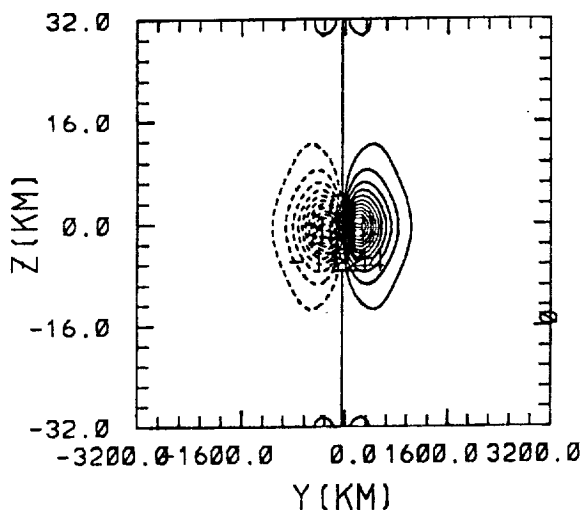


DIVERGENCE (X=0,Y,Z,T=3 HR)



CONTOUR FROM -0.27000 TO 0.27000 INTERVAL OF 0.30000E-05 CONTOUR FROM -0.64000E-05 TO 0.64000E-05 INTERVAL OF 0.80000E-06

VORTICITY (X=0,Y,Z,T=3 HR)



CONTOUR FROM -0.12000E-04 TO 0.12000E-04 INTERVAL OF 0.10000E-05

Figure 2 f

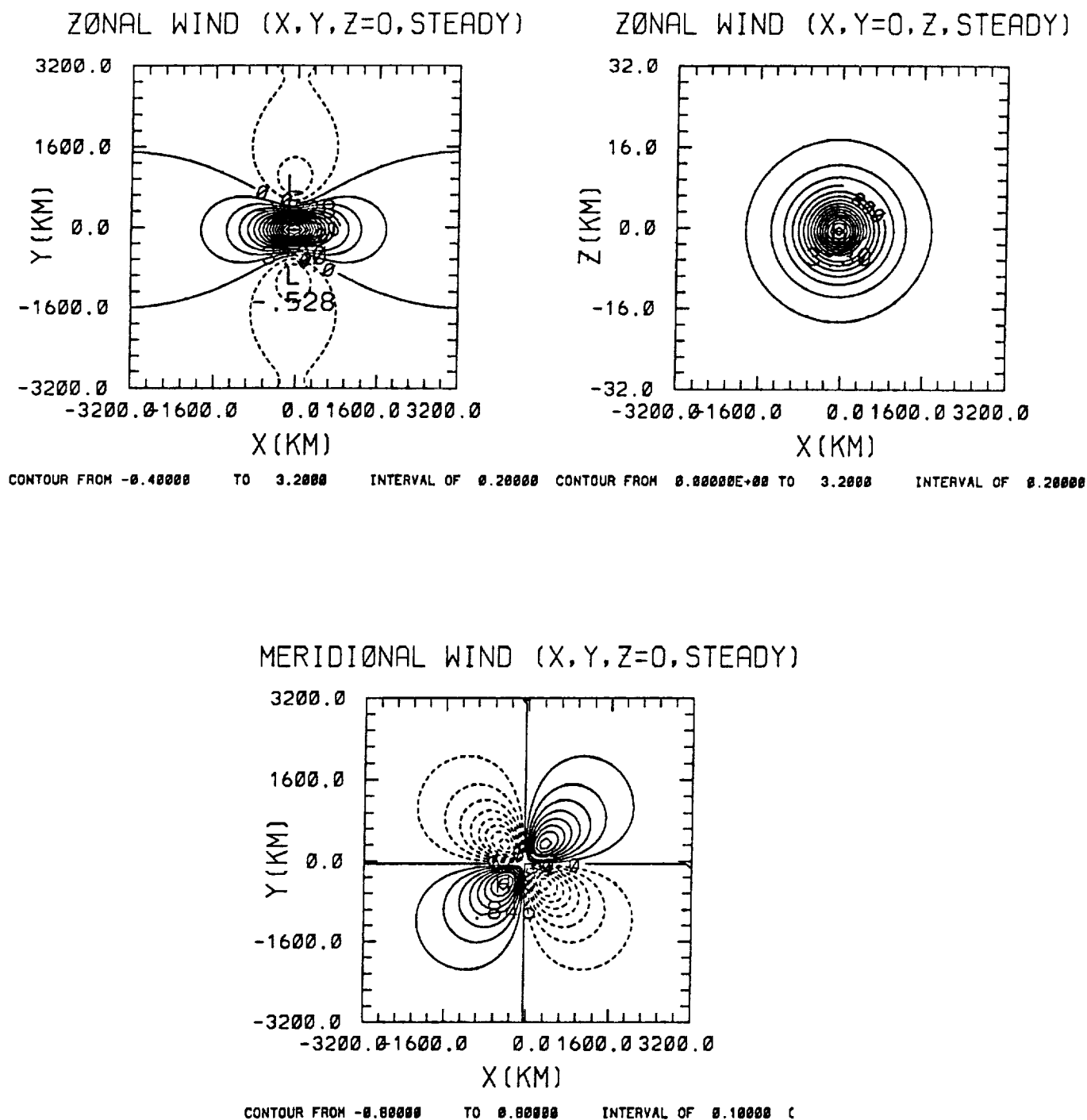
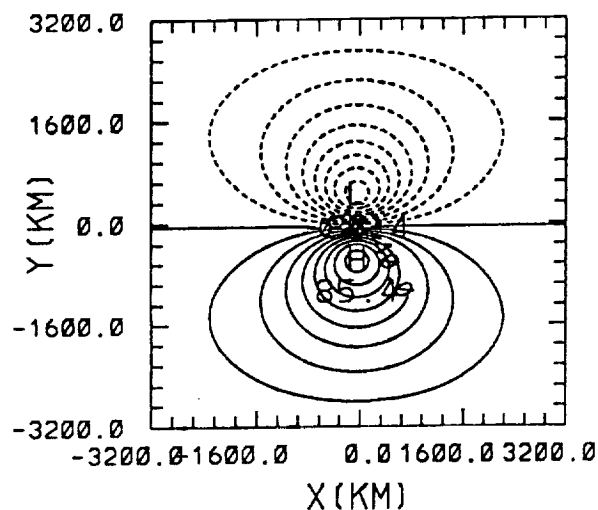


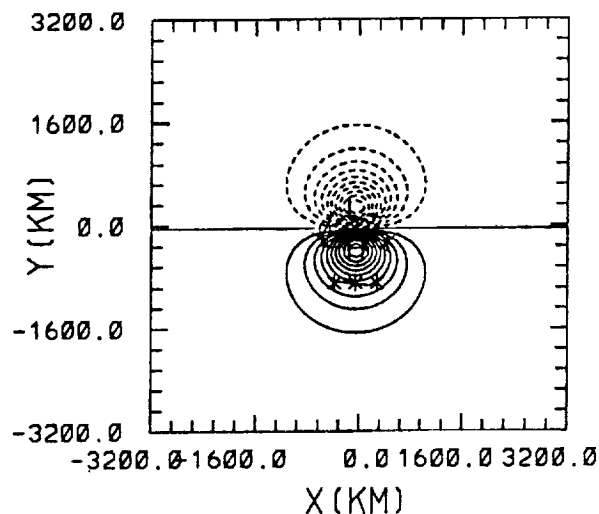
Figure 3 a

PRESSURE (X,Y,Z=0, STEADY)



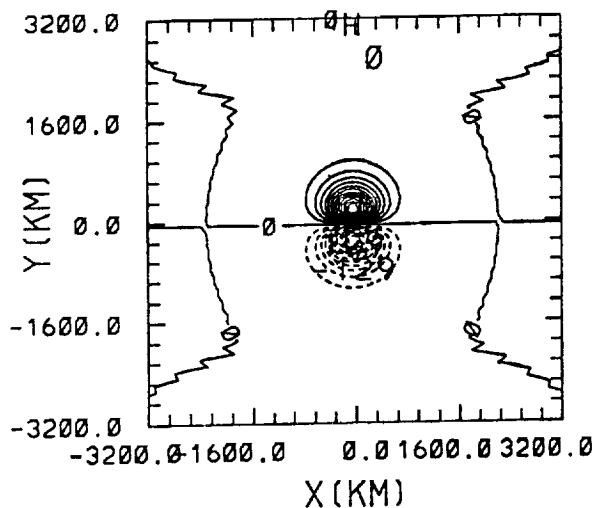
CONTOUR FROM -88.000 TO 88.000 INTERVAL OF 18.000

THETA (X,Y,Z=-1 KM, STEADY)



CONTOUR FROM -0.10000E+00 TO 0.10000E+00 INTERVAL OF 0.10000

VORTICITY (X,Y,Z=0, STEADY)



CONTOUR FROM -0.12000E-04 TO 0.12000E-04 INTERVAL OF 0.10000E-04

STREAMLINES (X,Y,Z=0, STEADY)

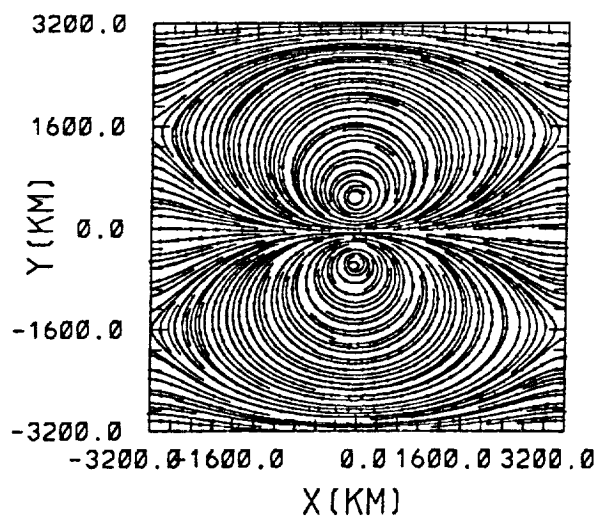


Figure 3 b

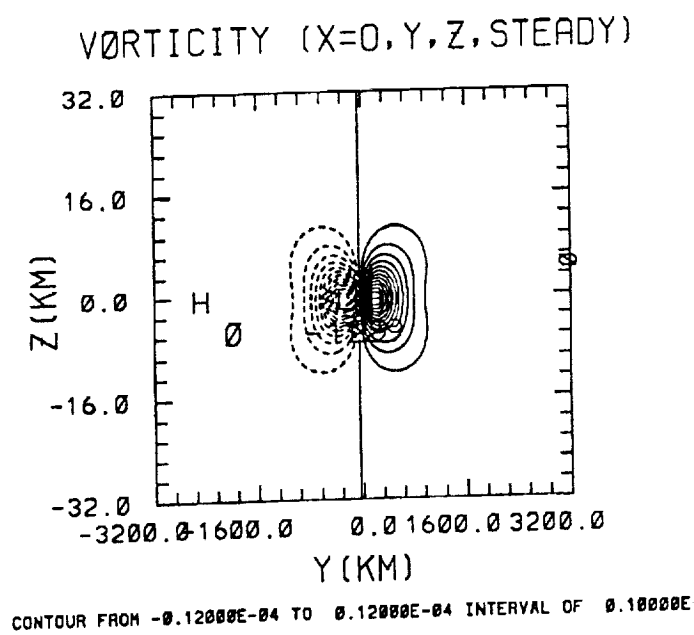
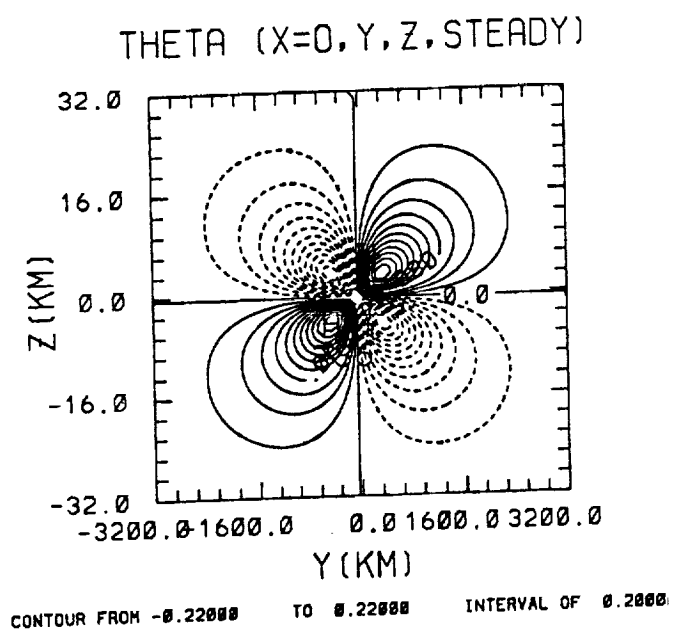
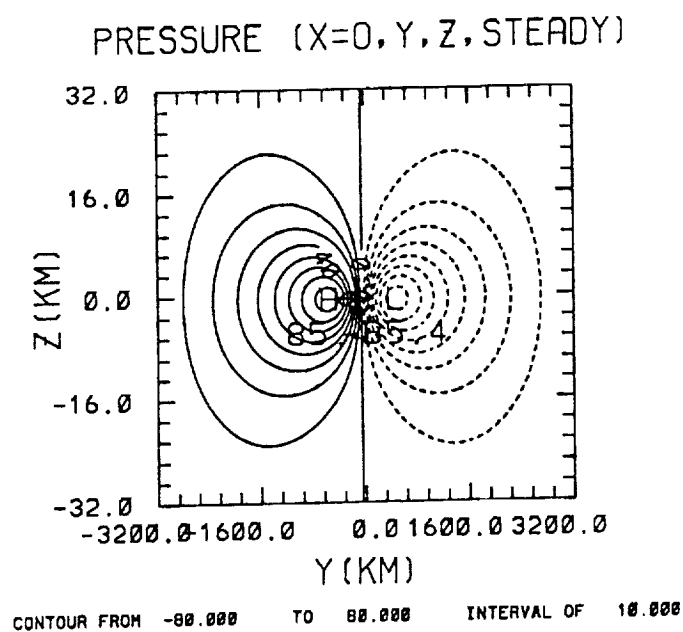
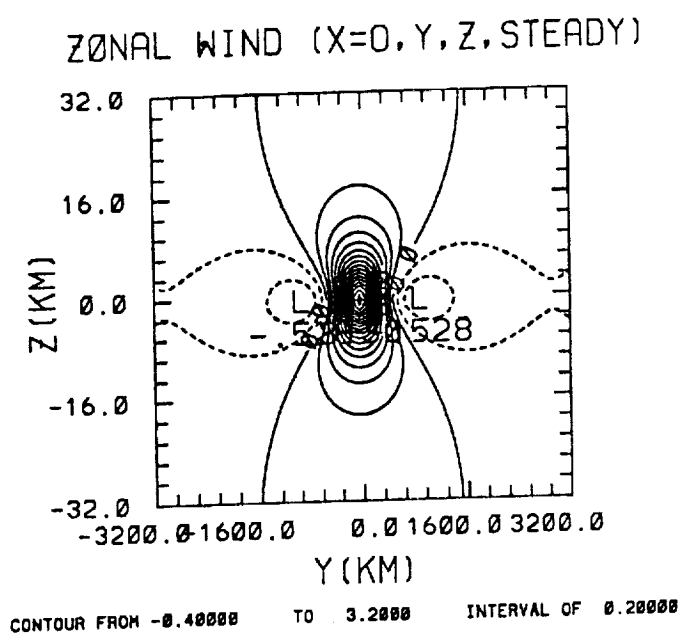


Figure 3 c



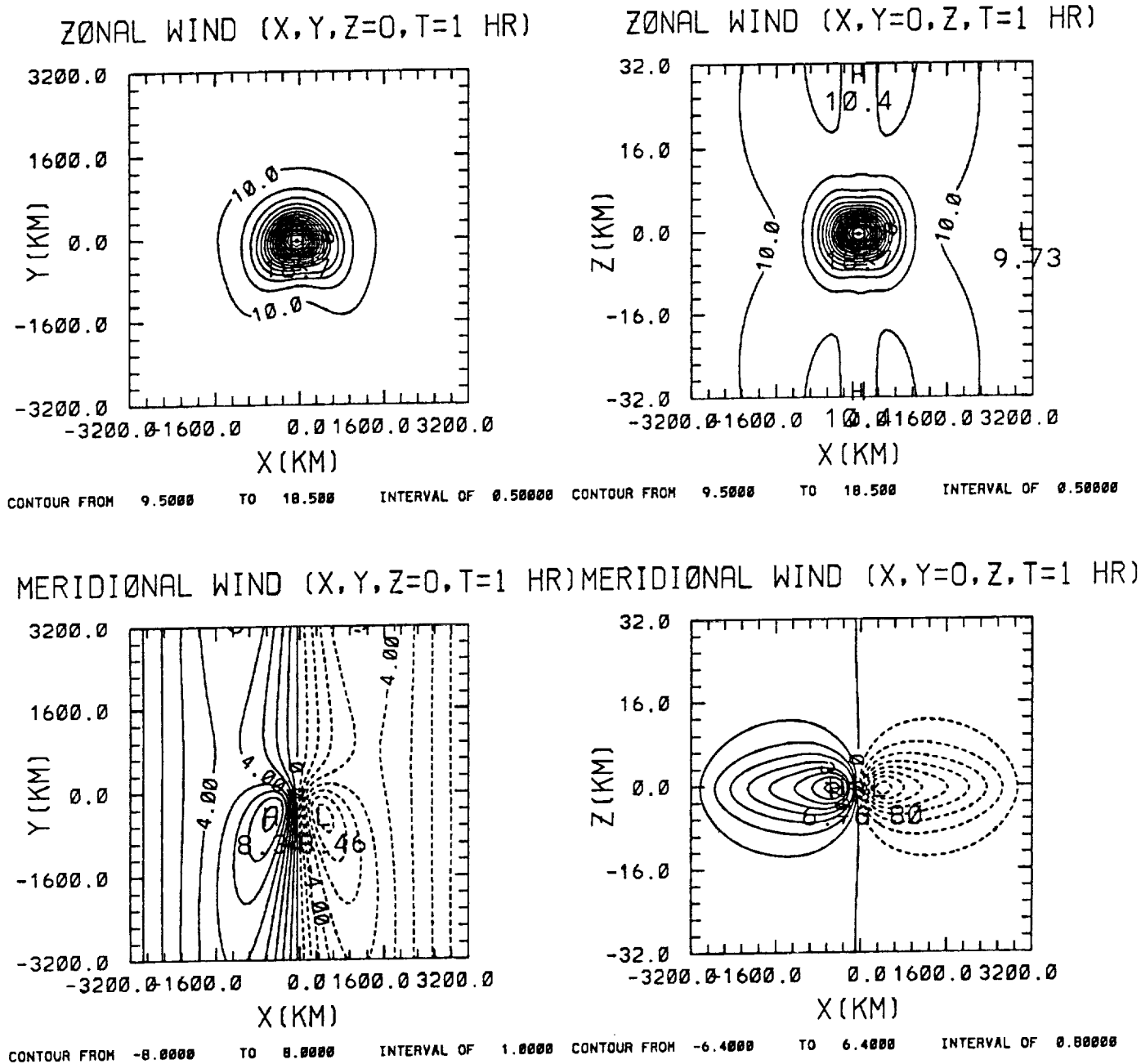


Figure 4 a

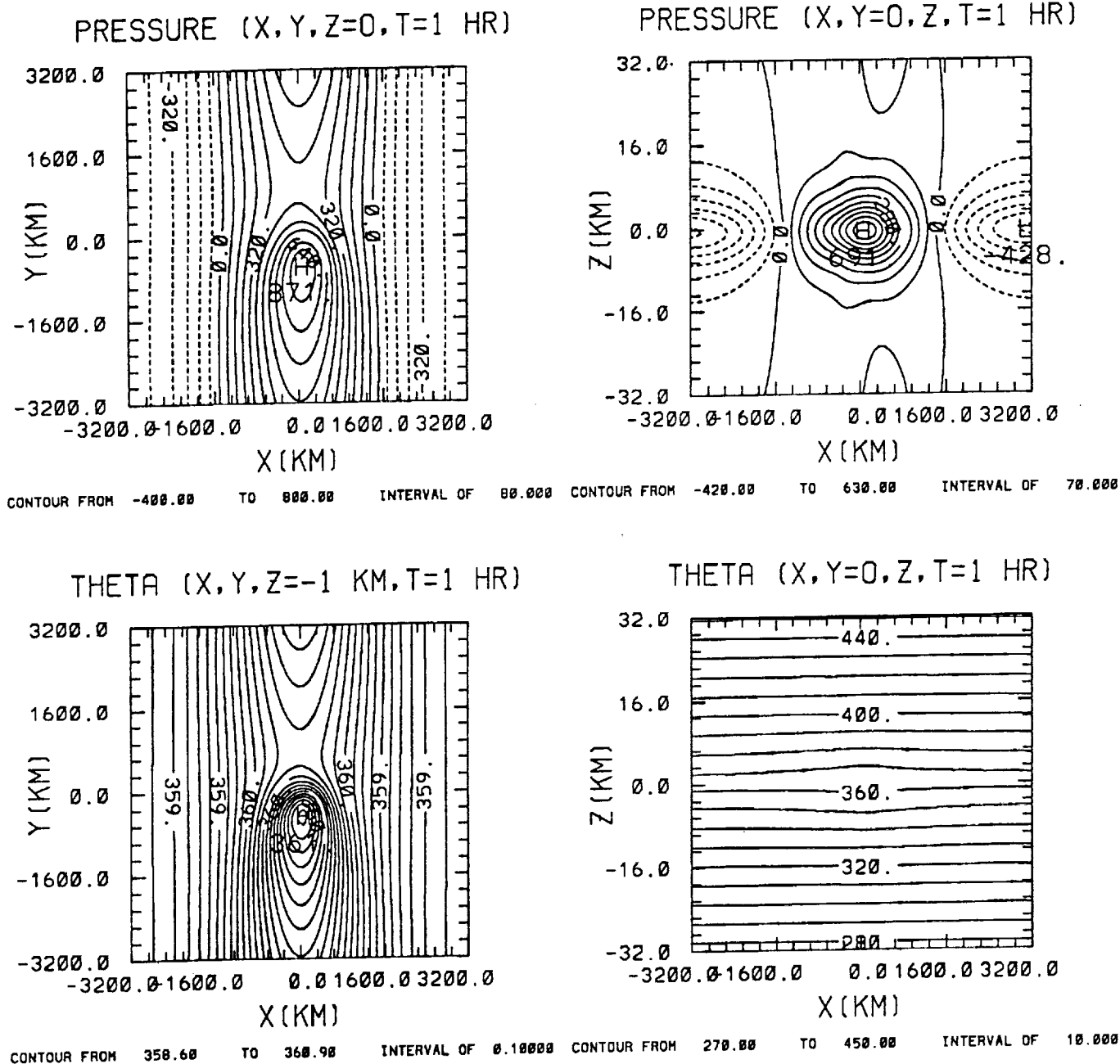
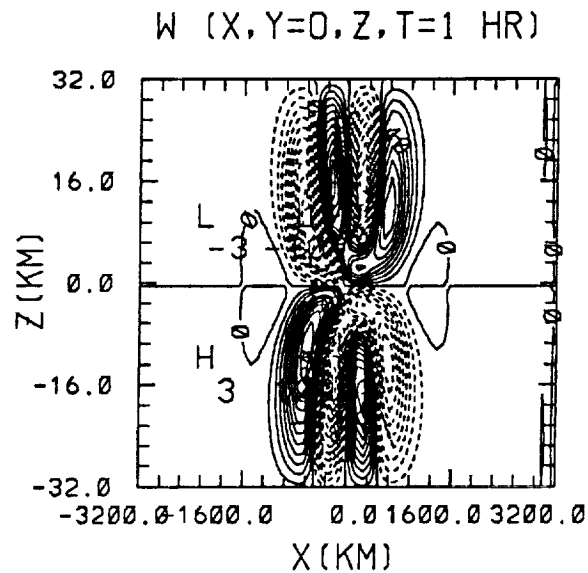
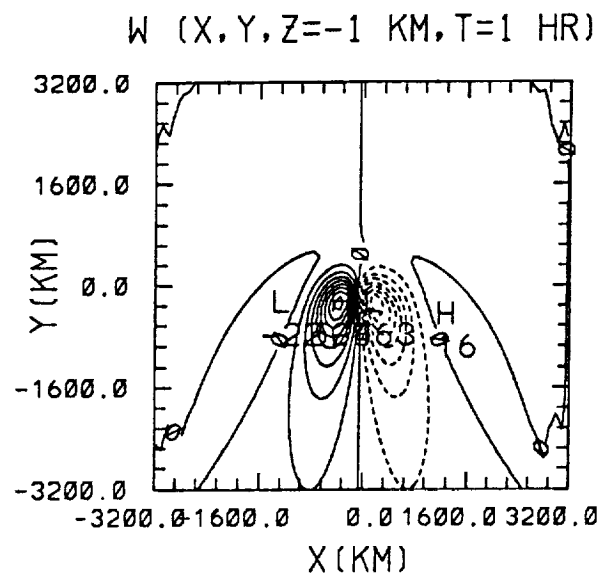
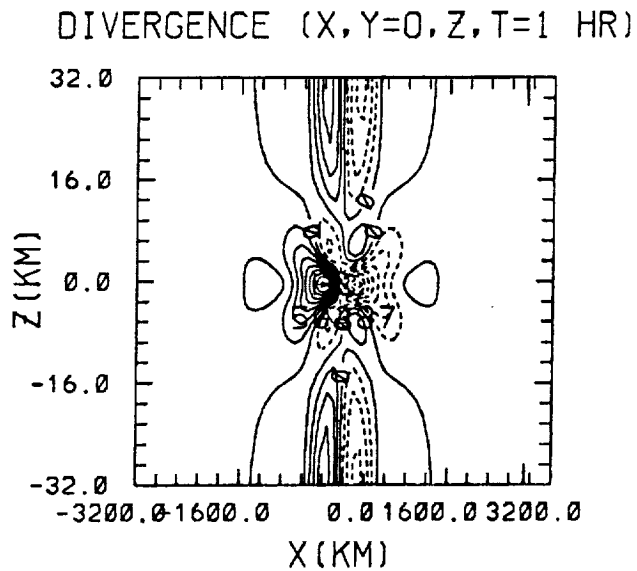
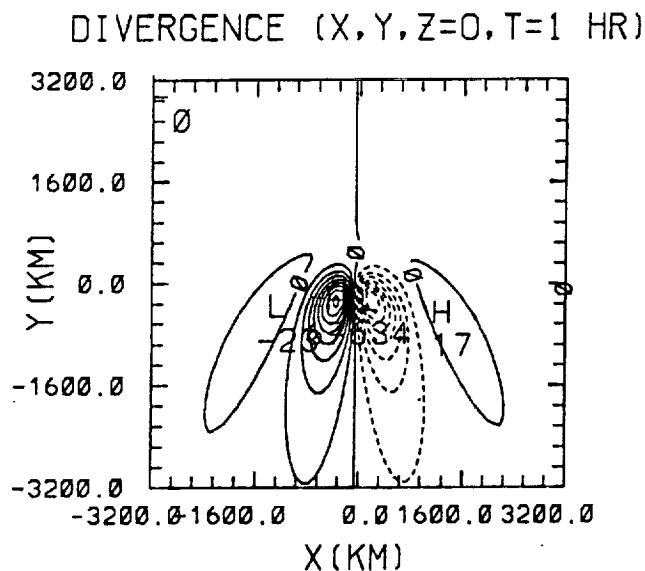


Figure 4 b



CONTOUR FROM -0.42000E-02 TO 0.48000E-02 INTERVAL OF 0.60000E-03 CONTOUR FROM -0.11000E-01 TO 0.11000E-01 INTERVAL OF 0.10000E-02



CONTOUR FROM -0.56000E-05 TO 0.64000E-05 INTERVAL OF 0.80000E-06 CONTOUR FROM -0.48000E-05 TO 0.48000E-05 INTERVAL OF 0.60000E-06

Figure 4 c

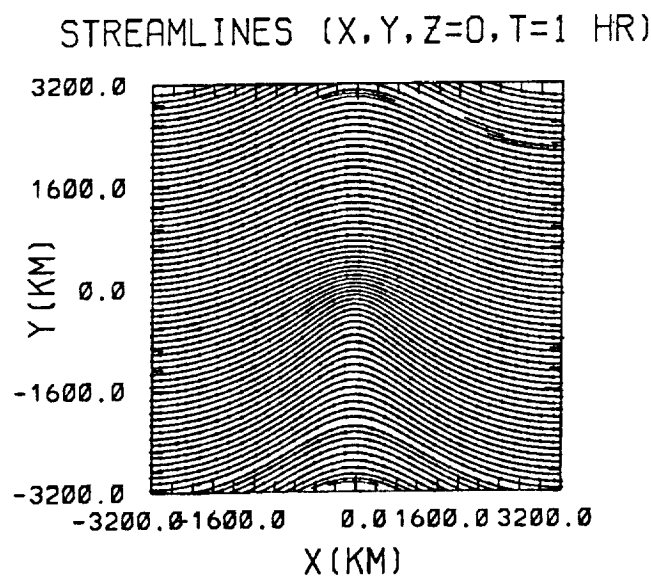
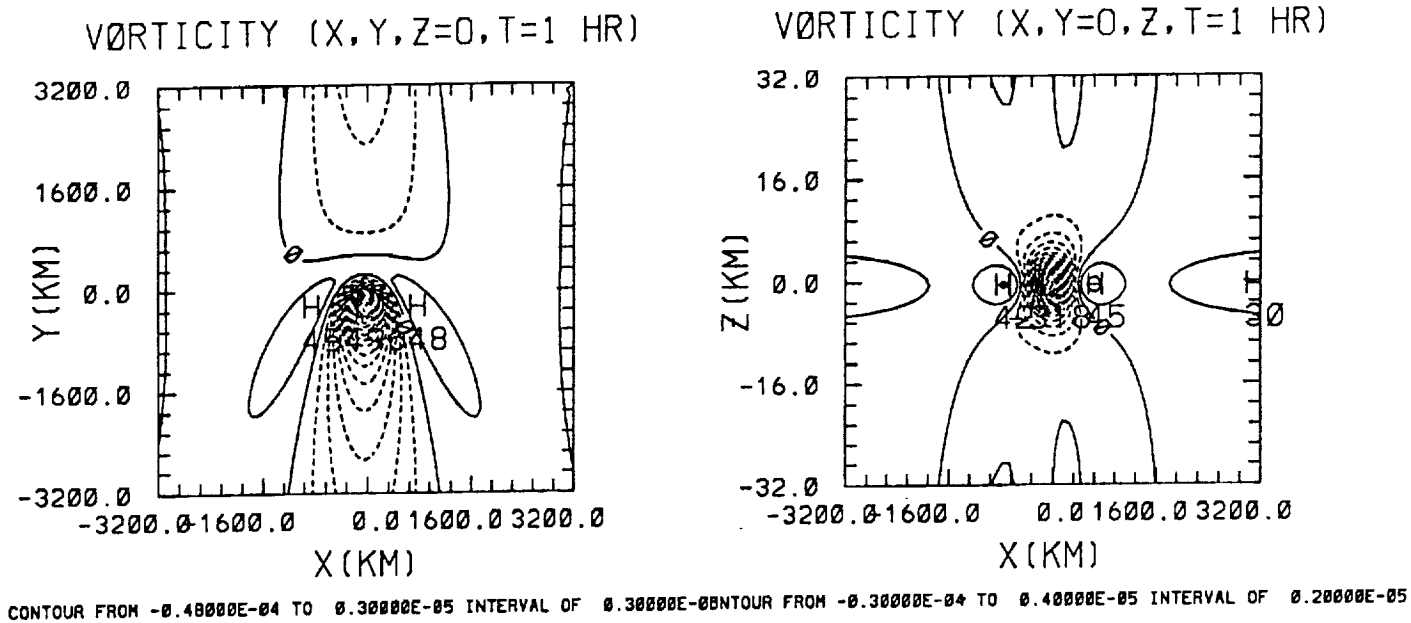


Figure 4 d

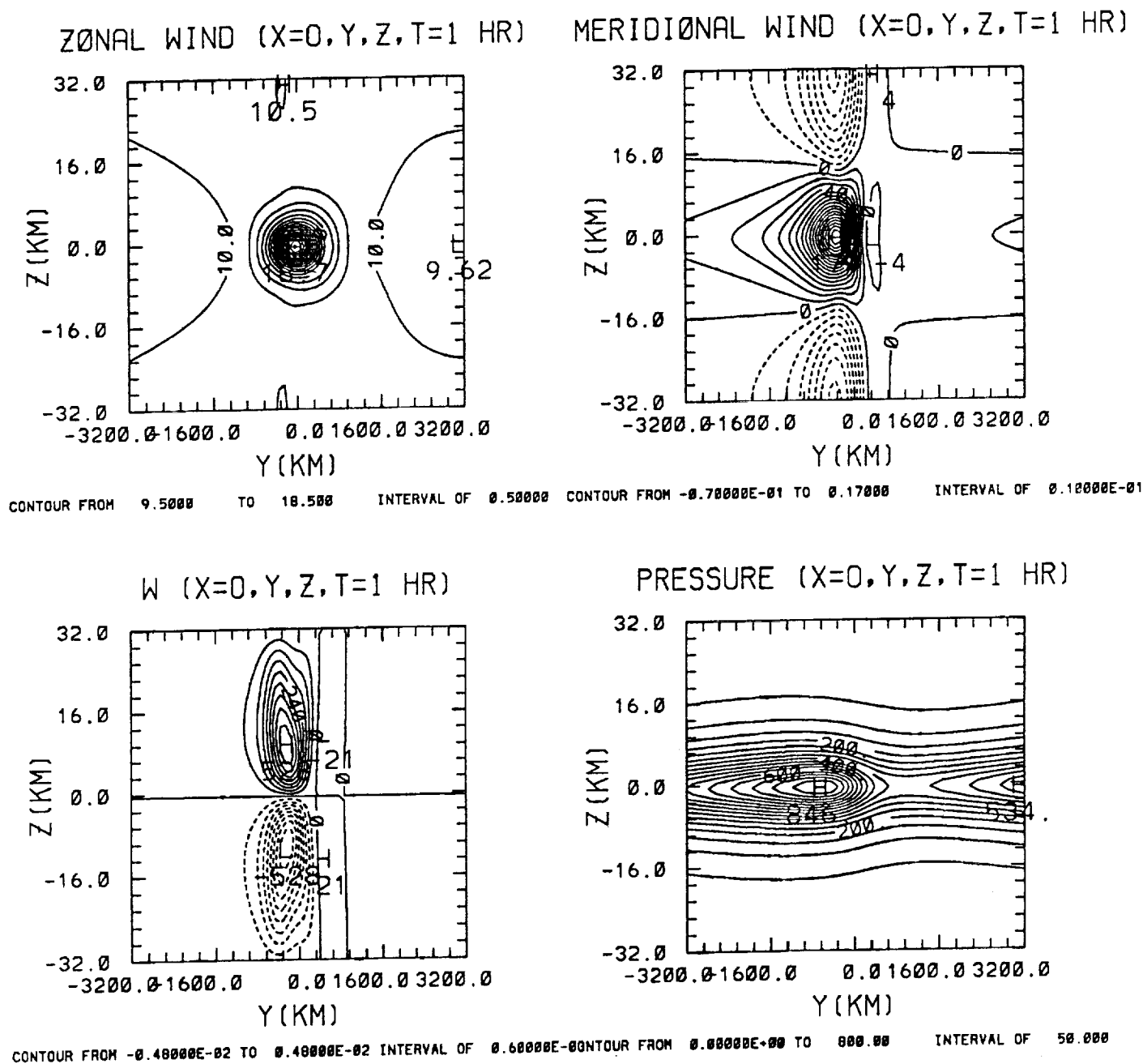


Figure 4 e

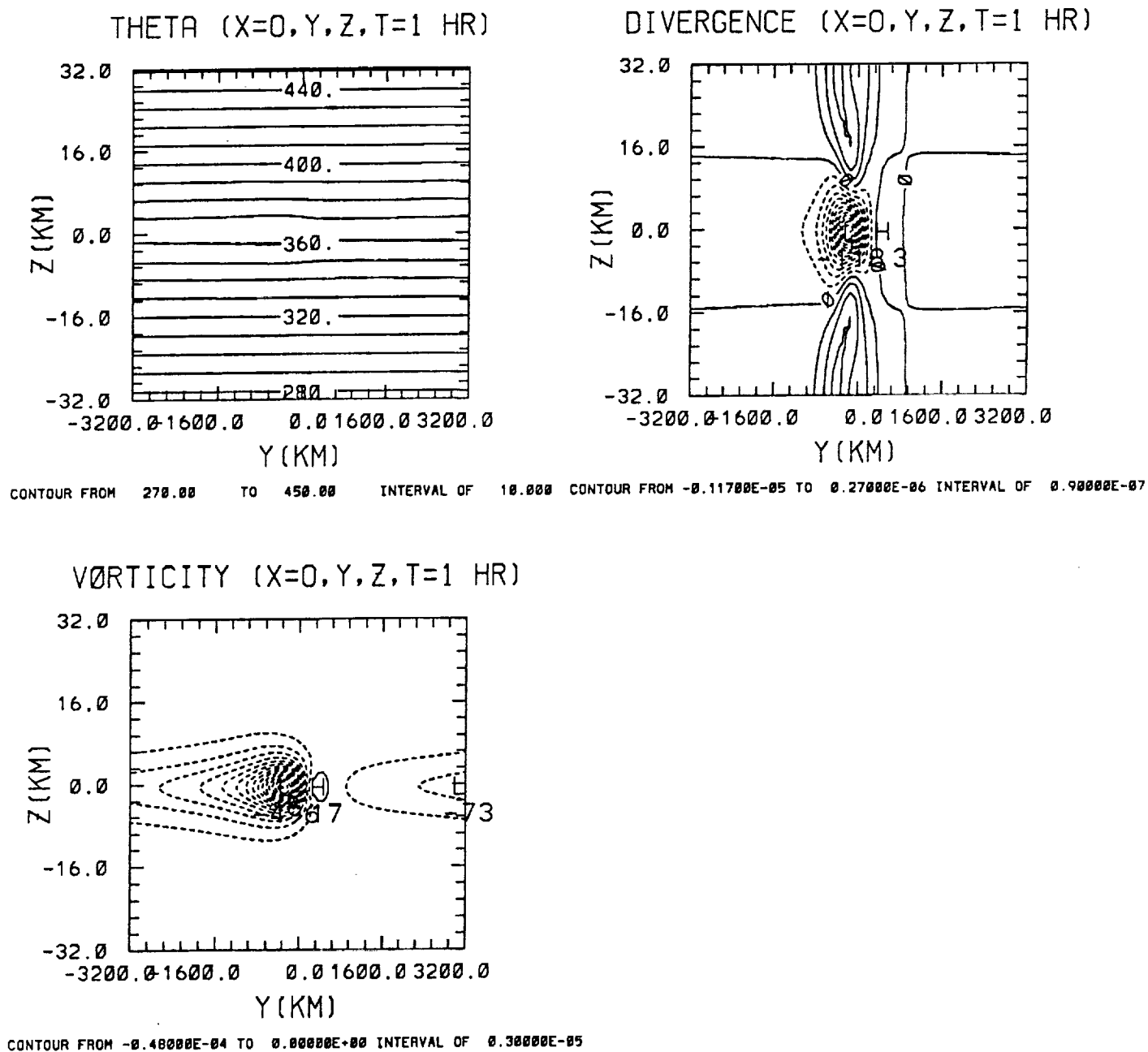


Figure 4 f

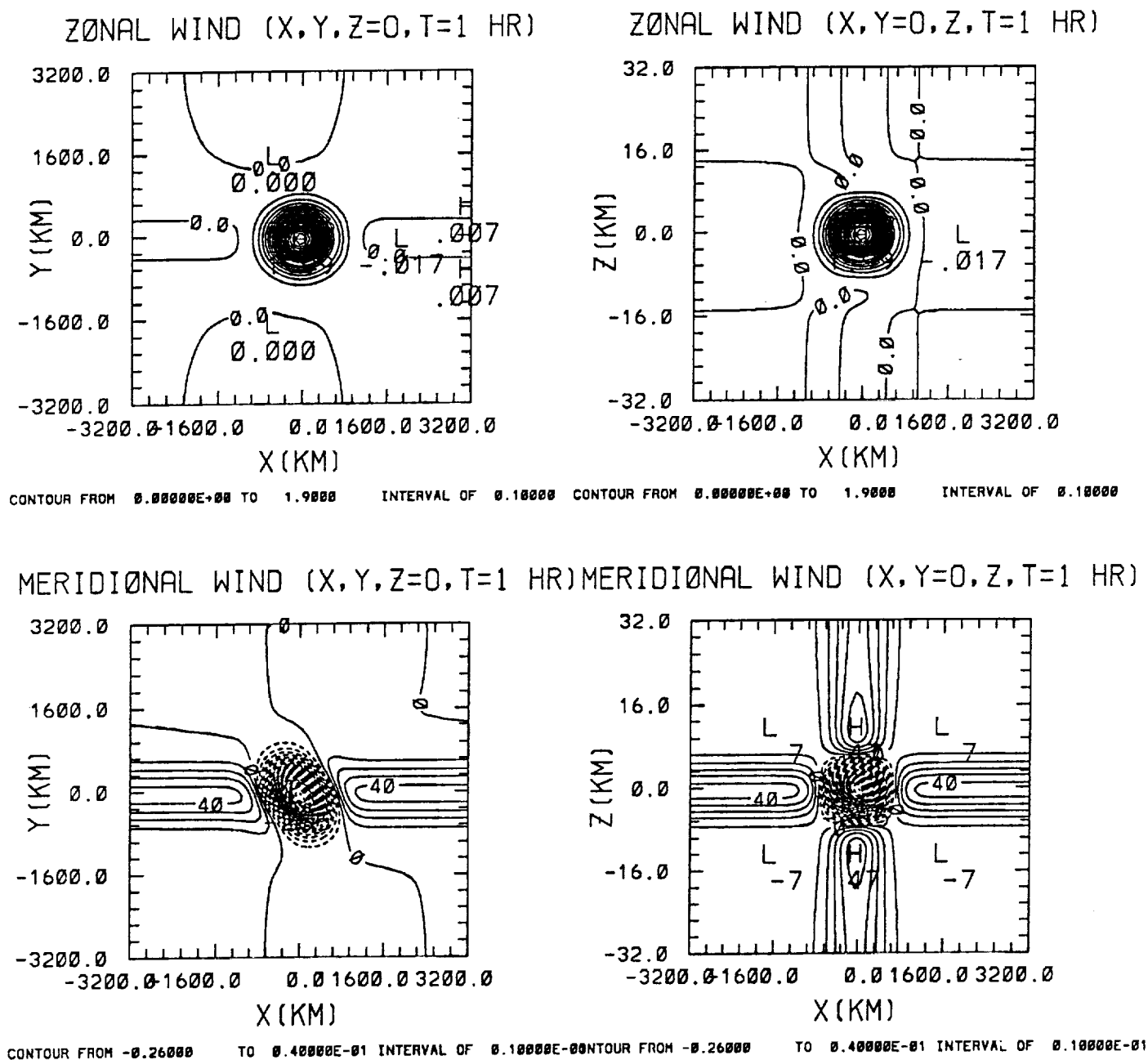
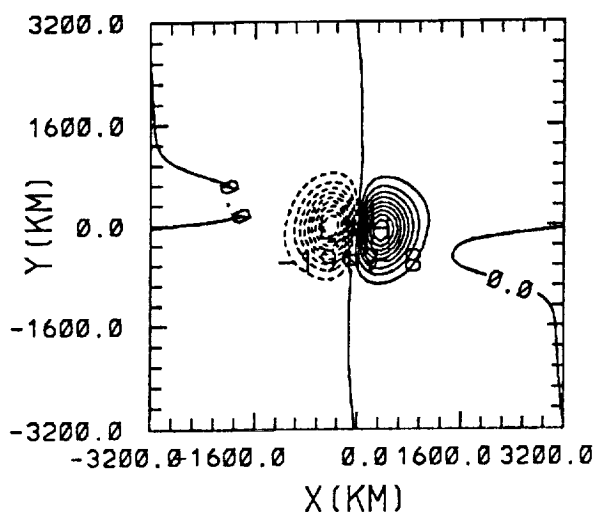
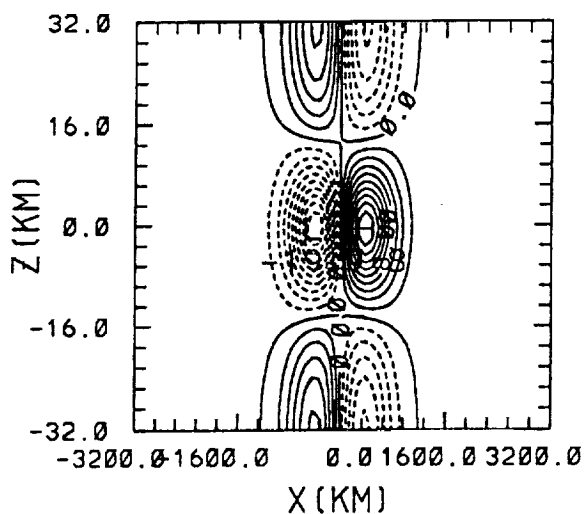


Figure 5 a

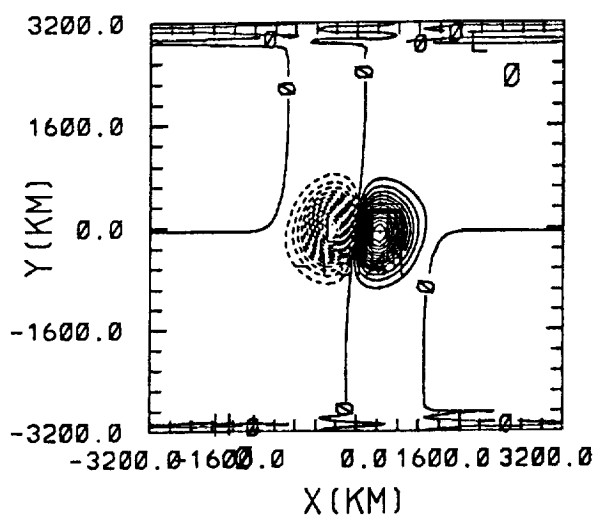
PRESSURE (X,Y,Z=0,T=1 HR)



PRESSURE (X,Y=0,Z,T=1 HR)



THETA (X,Y,Z=-1 KM,T=1 HR)



THETA (X,Y=0,Z,T=1 HR)

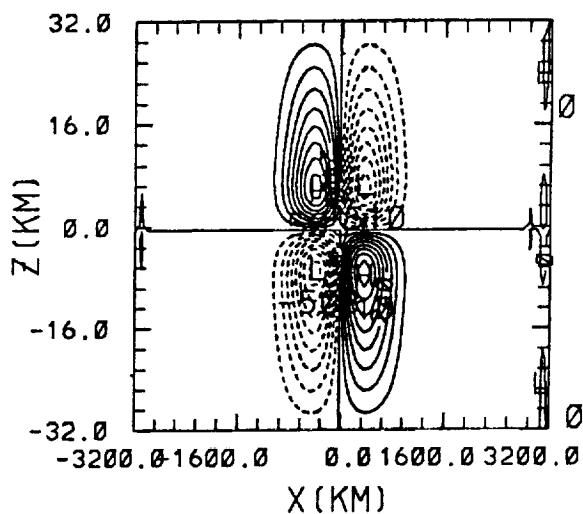
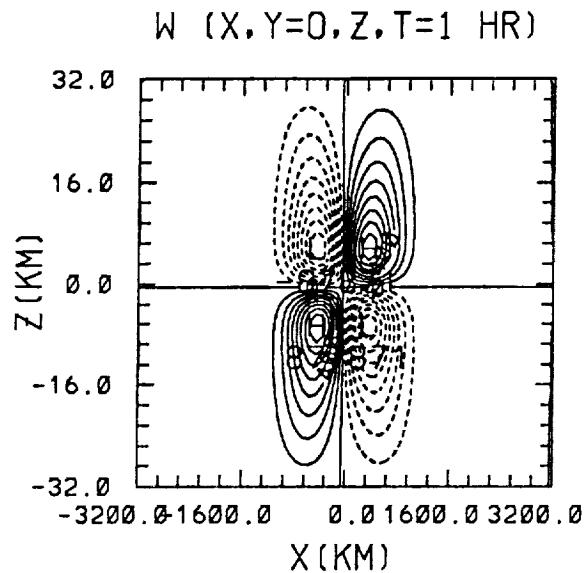
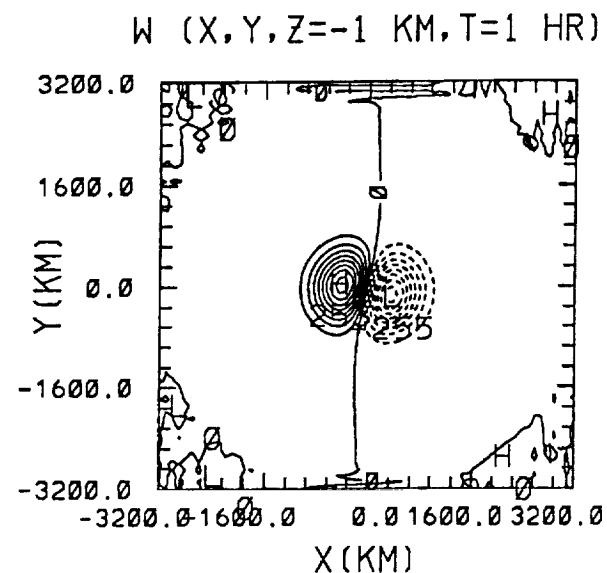
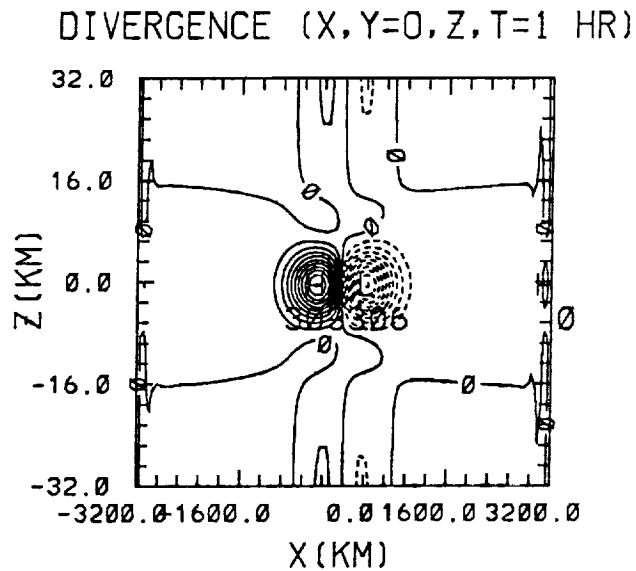
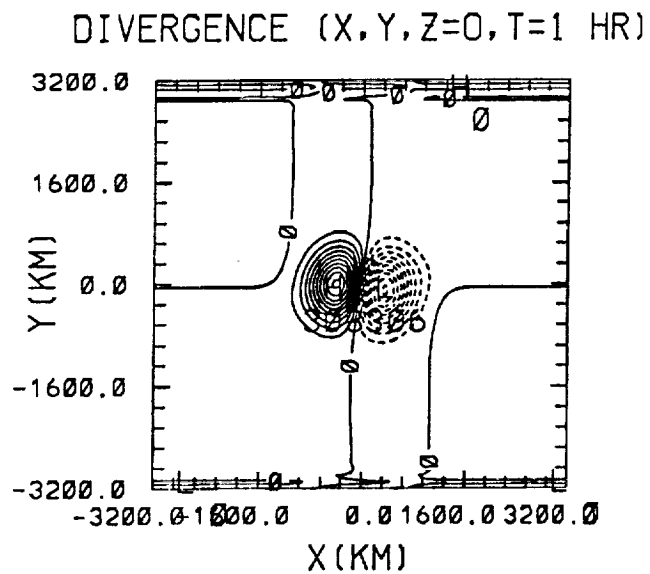


Figure 5 b



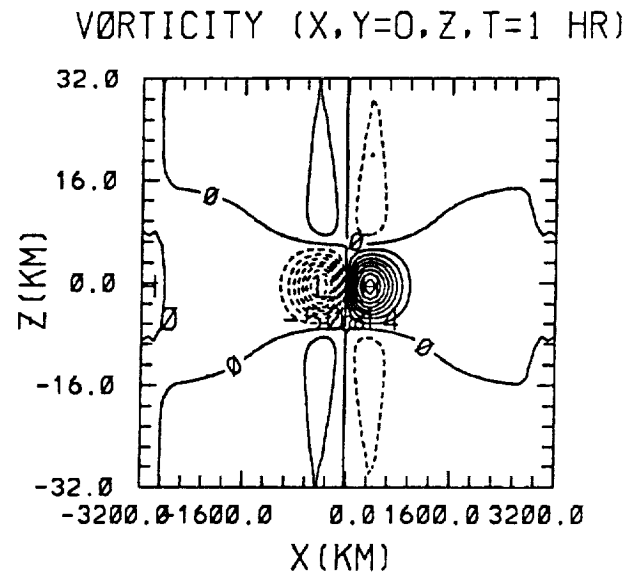
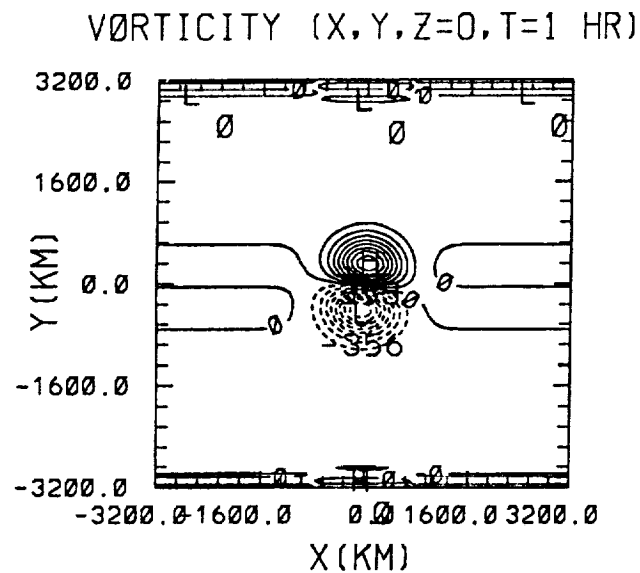


CONTOUR FROM  $-0.24000E-02$  TO  $0.24000E-02$  INTERVAL OF  $0.30000E-03$  CONTOUR FROM  $-0.80000E-02$  TO  $0.80000E-02$  INTERVAL OF  $0.10000E-02$



CONTOUR FROM  $-0.30000E-05$  TO  $0.30000E-05$  INTERVAL OF  $0.30000E-06$  CONTOUR FROM  $-0.30000E-05$  TO  $0.30000E-05$  INTERVAL OF  $0.30000E-06$

Figure 5 c



CONTOUR FROM -0.32000E-05 TO 0.32000E-05 INTERVAL OF 0.40000E-06 CONTOUR FROM -0.40000E-06 TO 0.40000E-06 INTERVAL OF 0.60000E-07

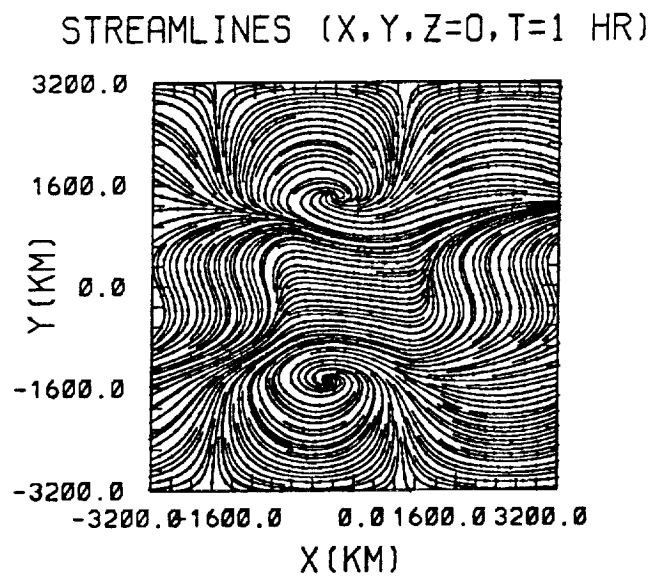
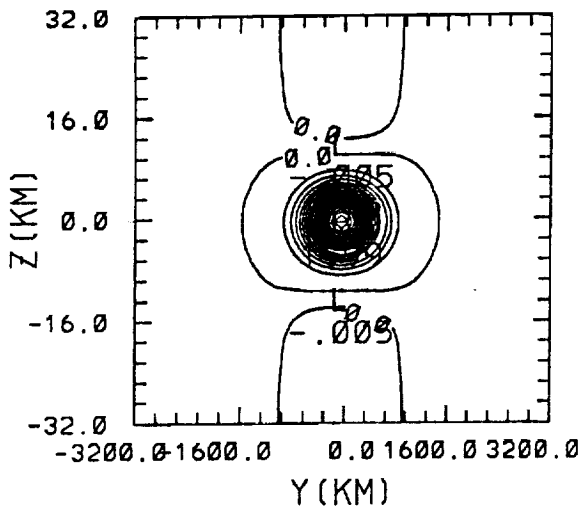
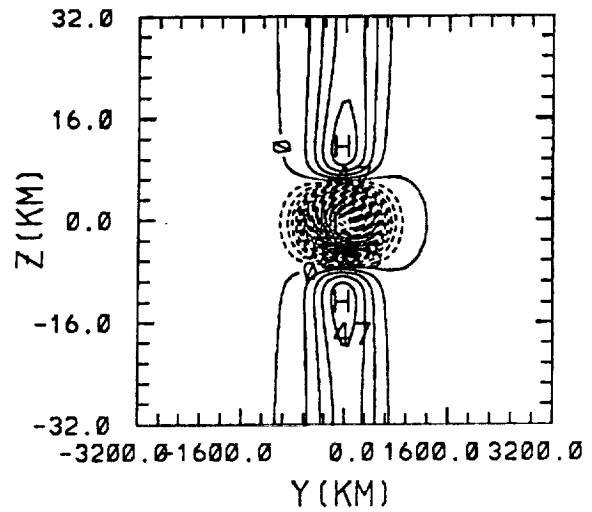


Figure 5 d

ZONAL WIND (X=0,Y,Z,T=1 HR)

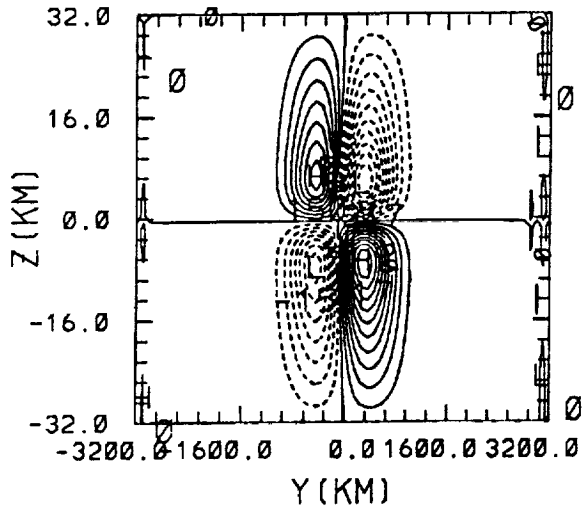


MERIDIONAL WIND (X=0,Y,Z,T=1 HR)

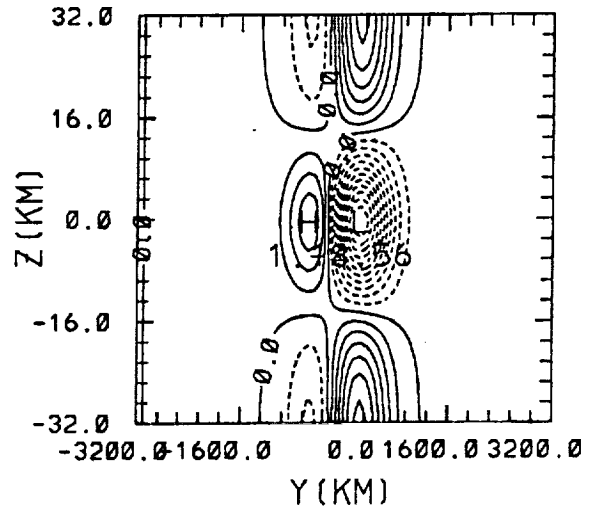


CONTOUR FROM 0.00000E+00 TO 1.9000 INTERVAL OF 0.10000 CONTOUR FROM -0.26000 TO 0.40000E-01 INTERVAL OF 0.10000E-01

W (X=0,Y,Z,T=1 HR)



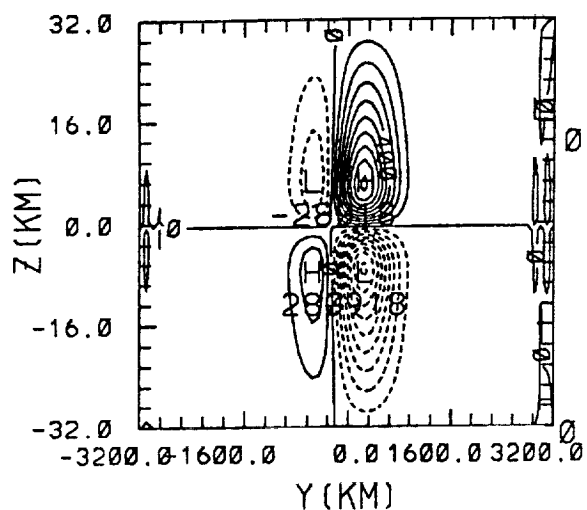
PRESSURE (X=0,Y,Z,T=1 HR)



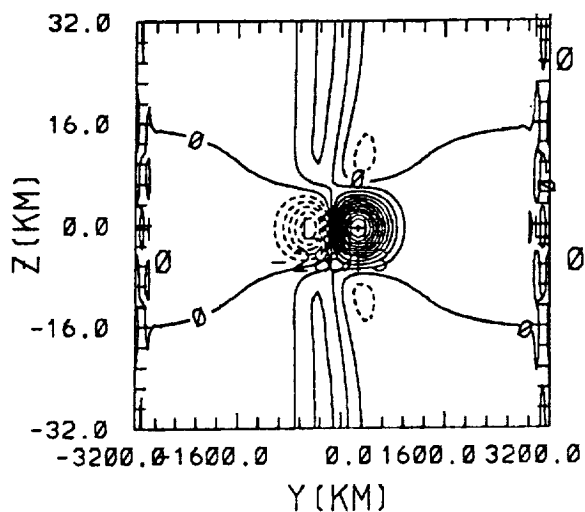
CONTOUR FROM -0.20000E-02 TO 0.20000E-02 INTERVAL OF 0.20000E-03 CONTOUR FROM -3.3000 TO 1.0000 INTERVAL OF 0.30000

Figure 5 e

THETA (X=0,Y,Z,T=1 HR)

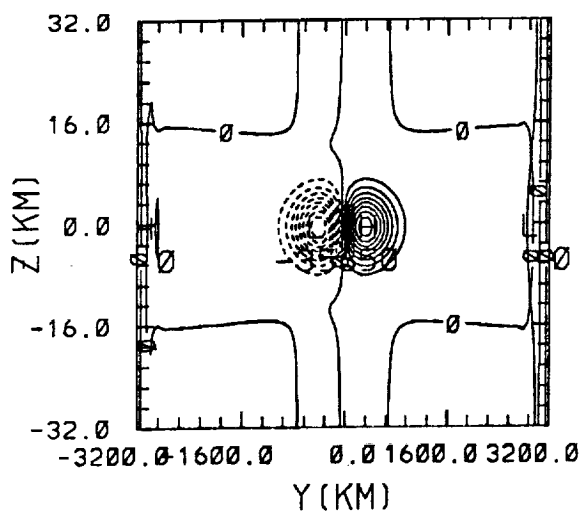


DIVERGENCE (X=0,Y,Z,T=1 HR)



CONTOUR FROM  $-0.90000E-02$  TO  $0.90000E-02$  INTERVAL OF  $0.10000E-02$  CONTOUR FROM  $-0.25000E-06$  TO  $0.60000E-06$  INTERVAL OF  $0.50000E-07$

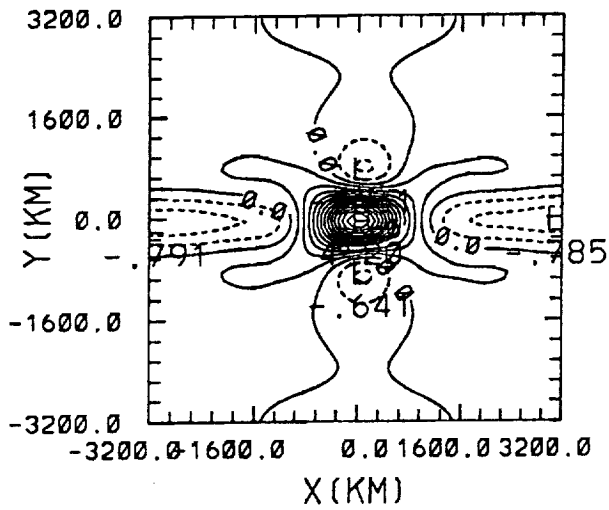
VORTICITY (X=0,Y,Z,T=1 HR)



CONTOUR FROM  $-0.32000E-05$  TO  $0.32000E-05$  INTERVAL OF  $0.40000E-06$

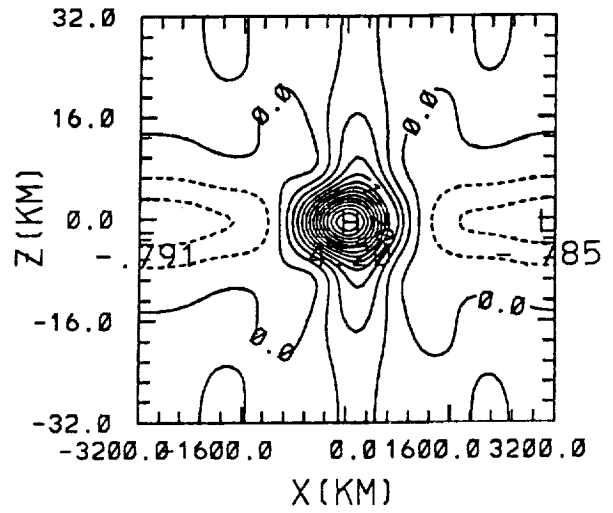
Figure 5 f

ZONAL WIND (X,Y,Z=0,T=6 HR)



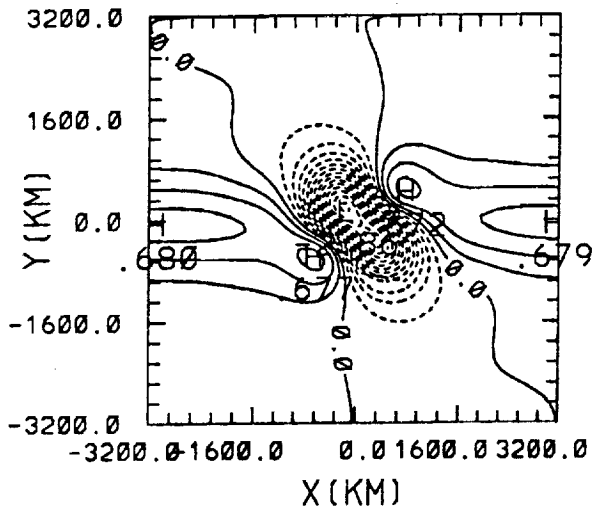
CONTOUR FROM -0.60000 TO 3.9000 INTERVAL OF 0.30000

ZONAL WIND (X,Y=0,Z,T=6 HR)



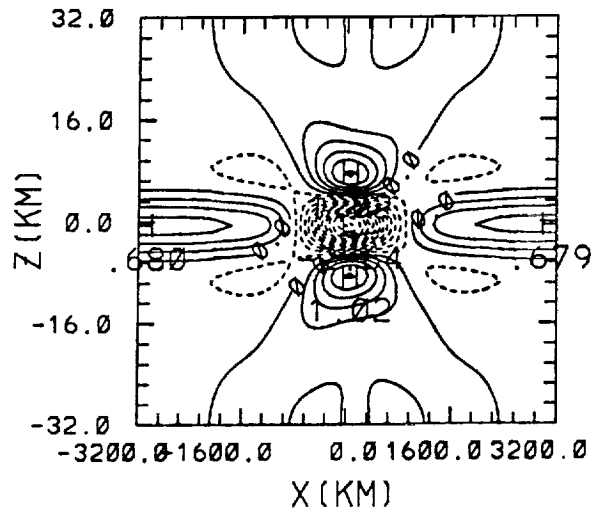
CONTOUR FROM -0.60000 TO 3.9000 INTERVAL OF 0.30000

MERIDIONAL WIND (X,Y,Z=0,T=6 HR)



CONTOUR FROM -2.0000 TO 0.60000 INTERVAL OF 0.20000

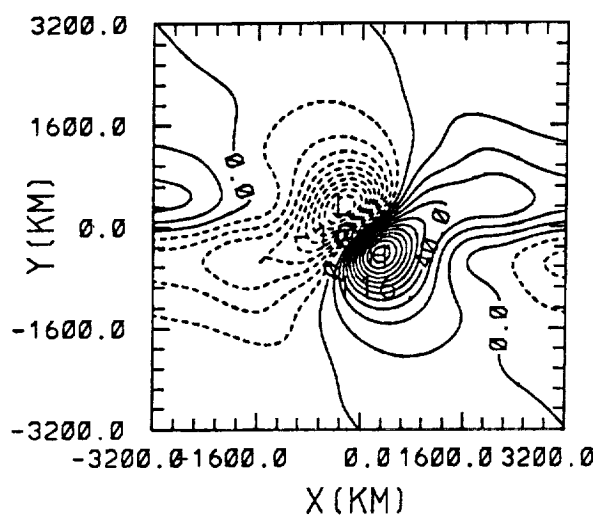
MERIDIONAL WIND (X,Y=0,Z,T=6 HR)



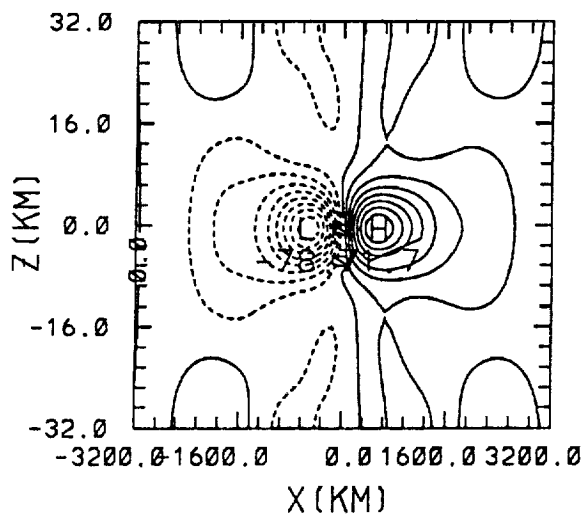
CONTOUR FROM -2.6000 TO 1.0000 INTERVAL OF 0.20000

Figure 6 a

PRESSURE (X,Y,Z=0,T=6 HR)

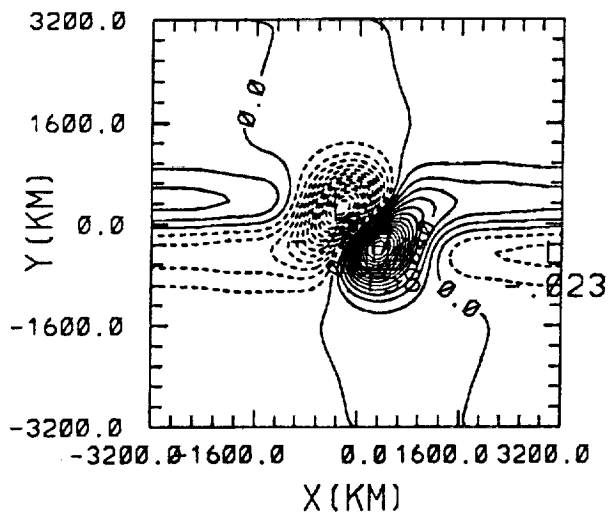


PRESSURE (X,Y=0,Z,T=6 HR)

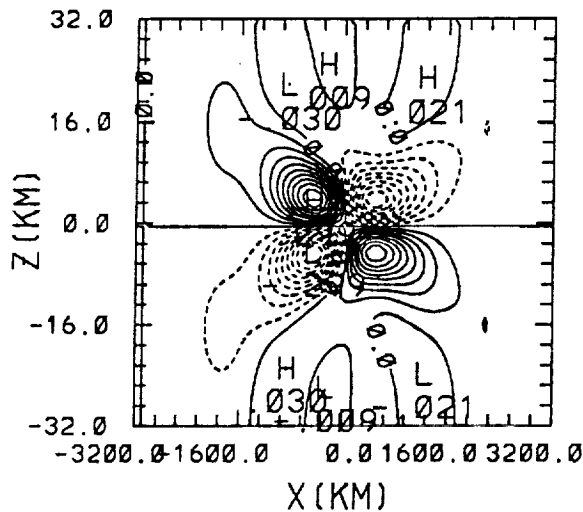


CONTOUR FROM -100.00 TO 110.00 INTERVAL OF 10.000 CONTOUR FROM -72.000 TO 63.000 INTERVAL OF 9.0000

THETA (X,Y,Z=-1 KM,T=6 HR)

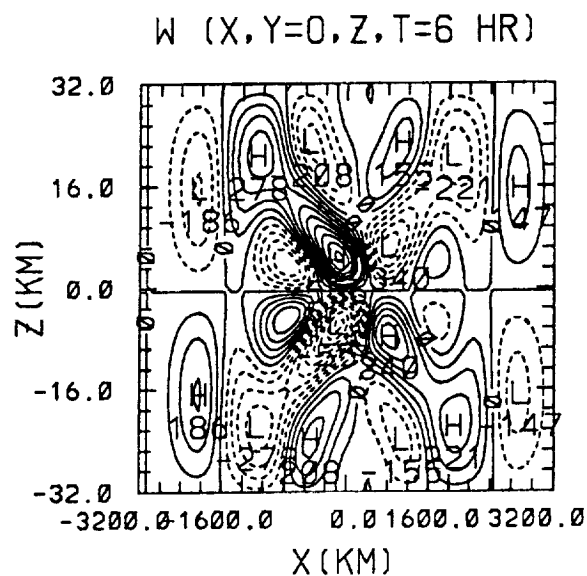
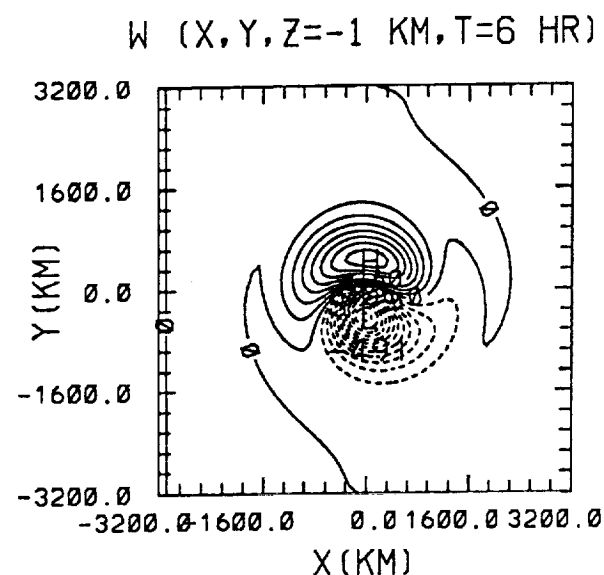


THETA (X,Y=0,Z,T=6 HR)

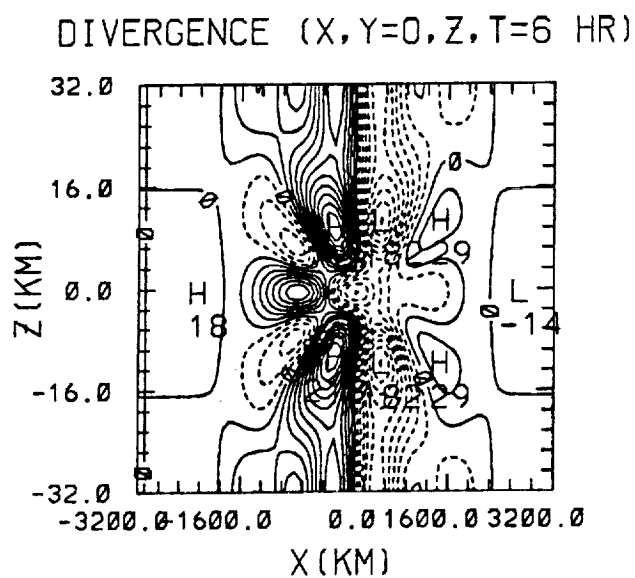
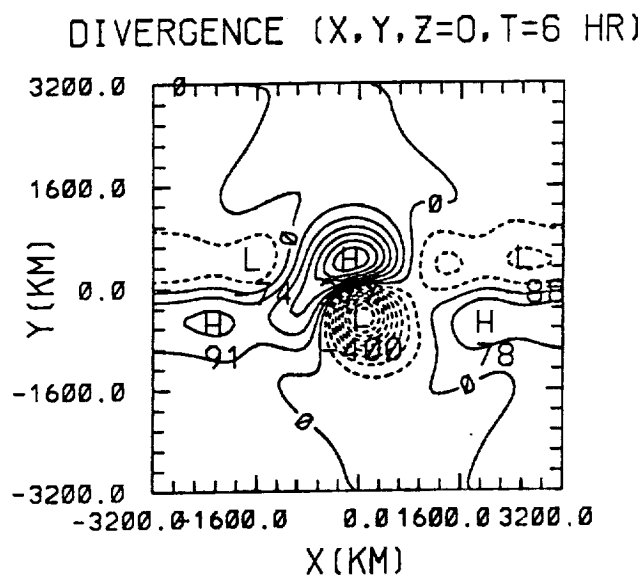


CONTOUR FROM -0.14000 TO 0.15000 INTERVAL OF 0.10000E-000 CONTOUR FROM -0.27000 TO 0.27000 INTERVAL OF 0.30000E-01

Figure 6 b



CONTOUR FROM  $-0.40000E-02$  TO  $0.20000E-02$  INTERVAL OF  $0.40000E-03$  CONTOUR FROM  $-0.54000E-02$  TO  $0.54000E-02$  INTERVAL OF  $0.60000E-03$



CONTOUR FROM  $-0.36000E-05$  TO  $0.24000E-05$  INTERVAL OF  $0.40000E-06$  CONTOUR FROM  $-0.18000E-05$  TO  $0.20000E-05$  INTERVAL OF  $0.20000E-06$

Figure 6 c

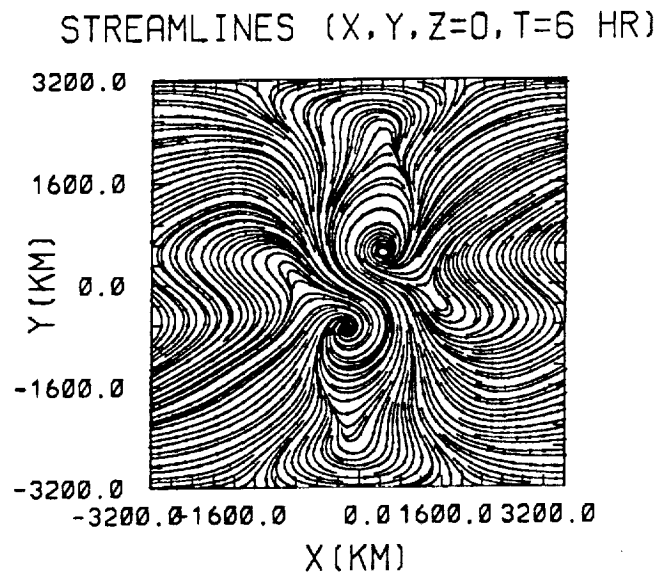
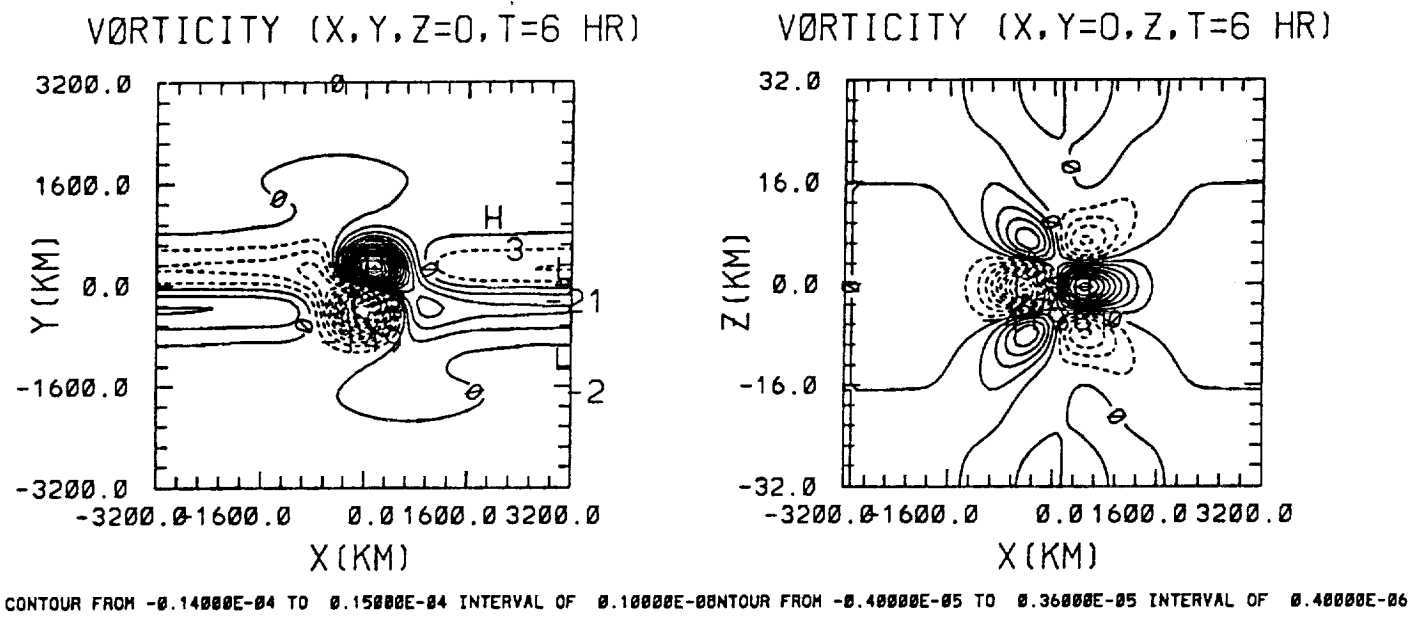


**Figure 6 d**



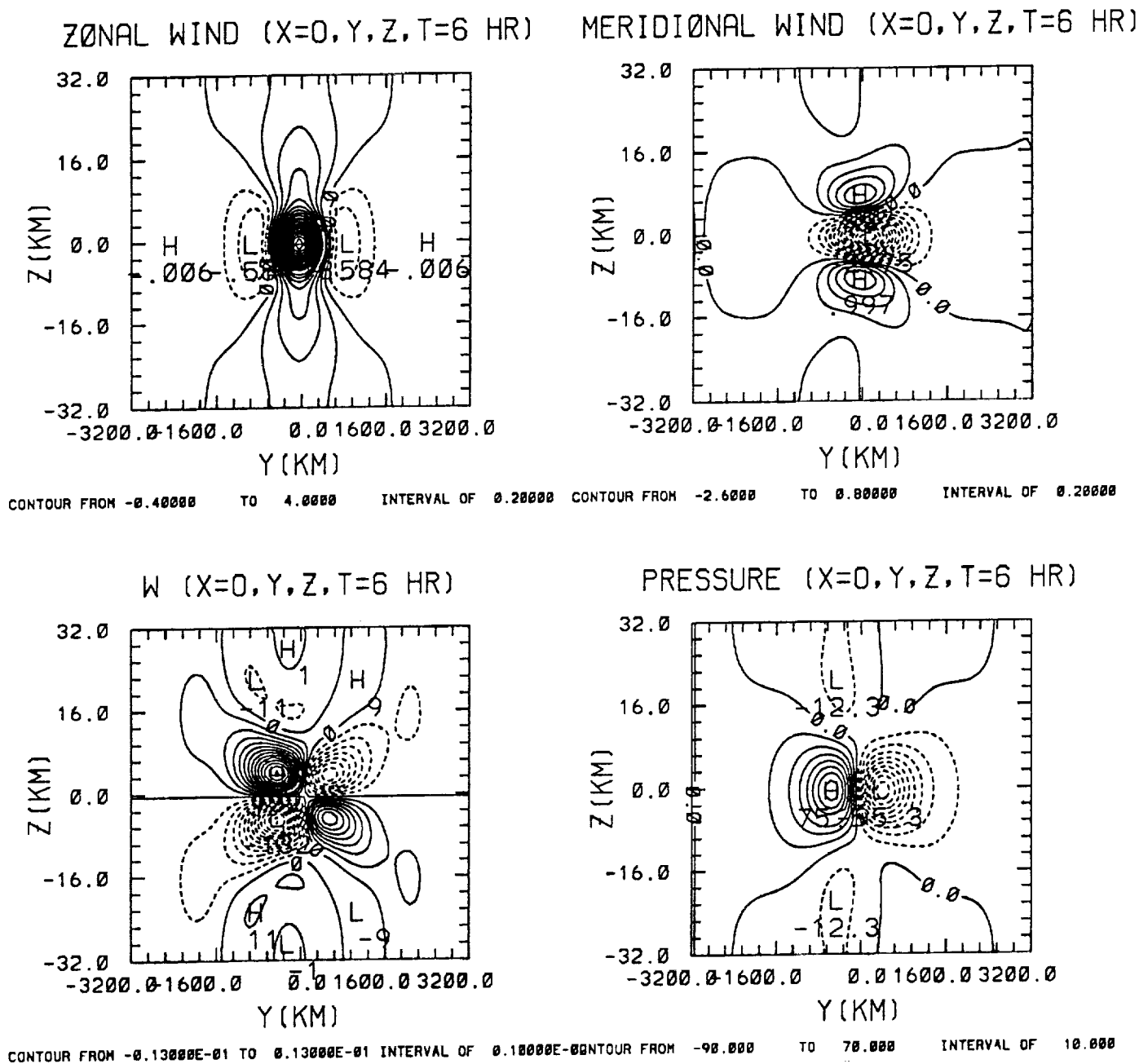
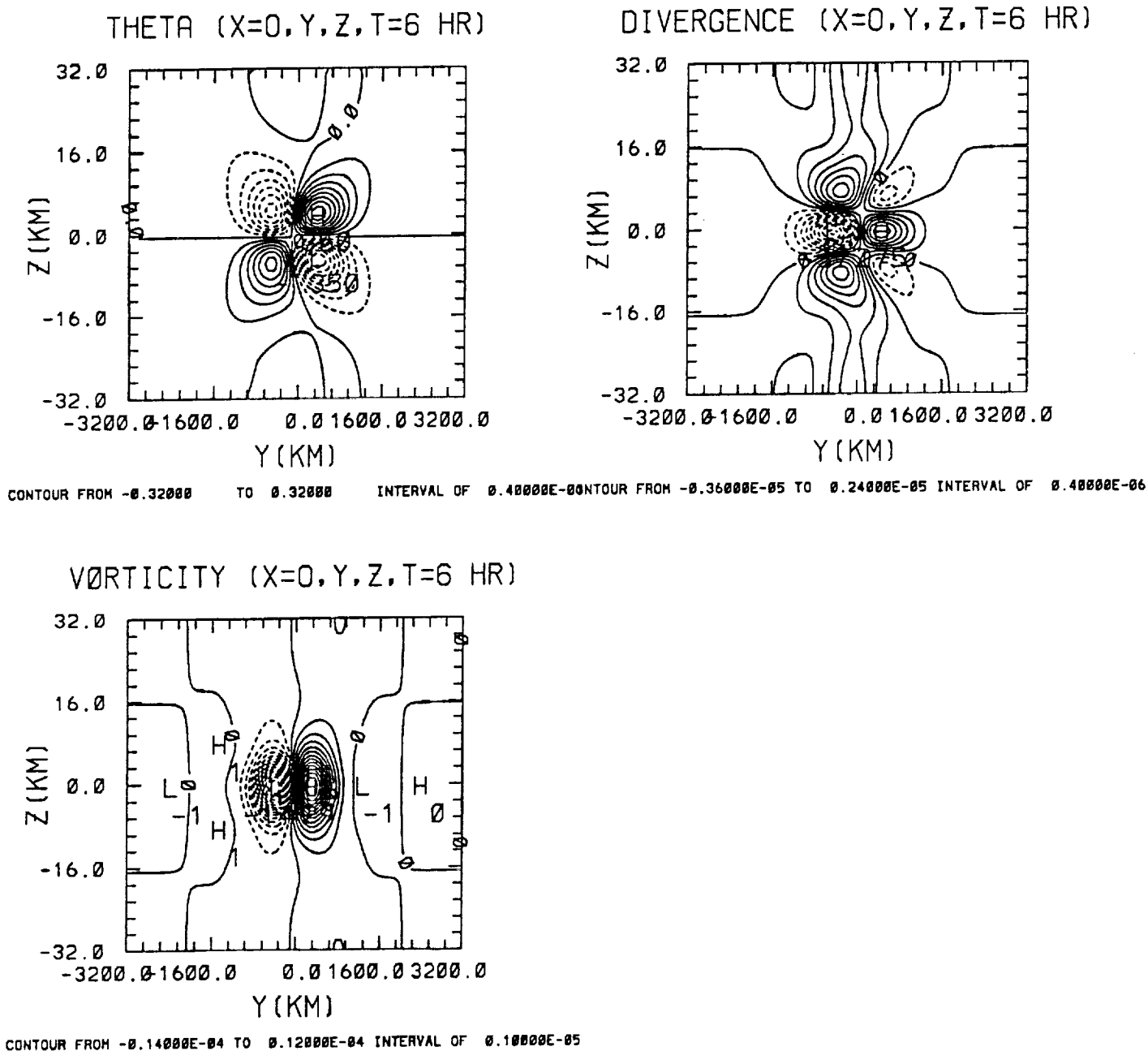
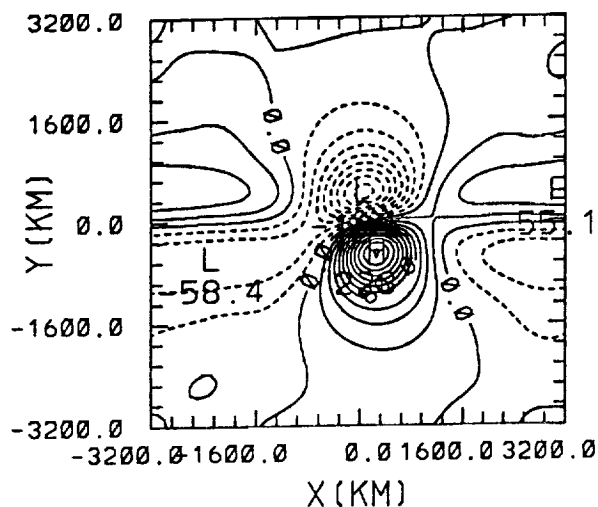


Figure 6 e



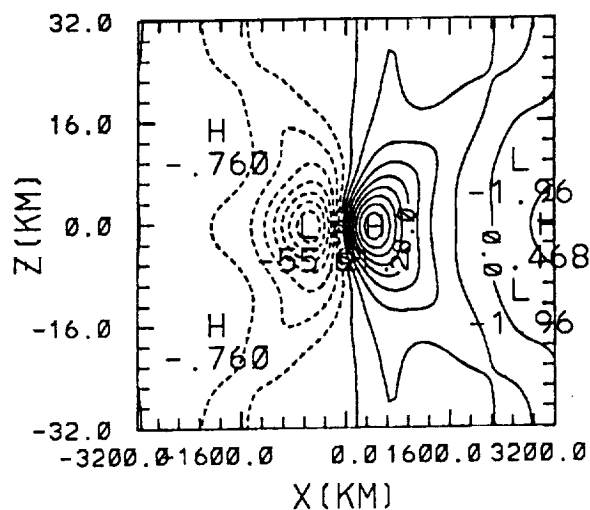


PRESSURE (X,Y,Z=0,T=12 HR)



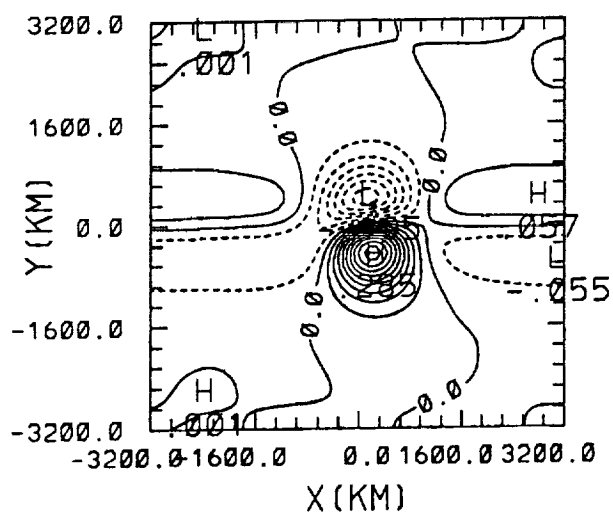
CONTOUR FROM -160.00 TO 220.00 INTERVAL OF 20.000

PRESSURE (X,Y=0,Z,T=12 HR)



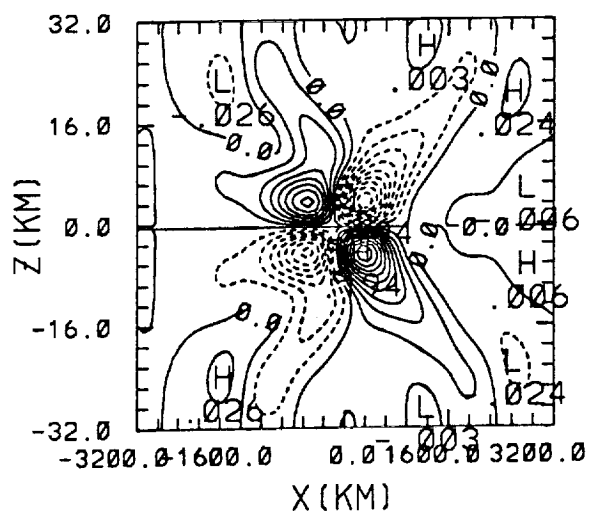
CONTOUR FROM -49.000 TO 56.000 INTERVAL OF 7.0000

THETA (X,Y,Z=-1 KM,T=12 HR)



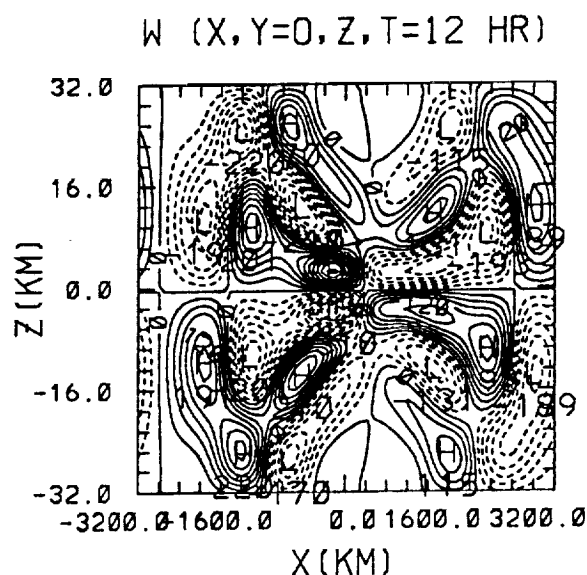
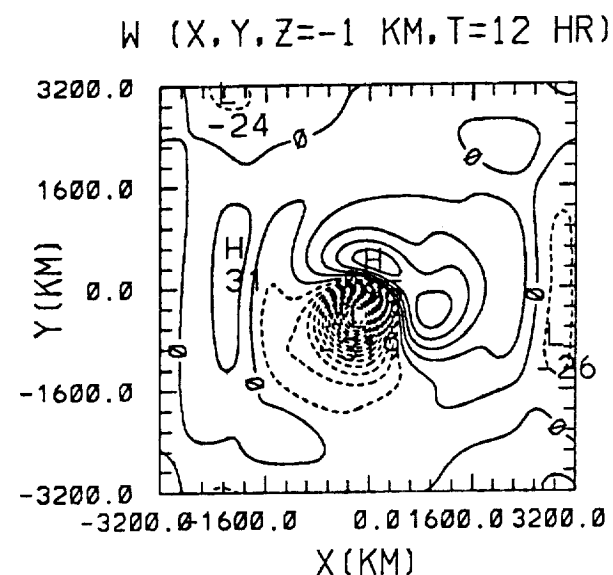
CONTOUR FROM -0.18000 TO 0.27000 INTERVAL OF 0.30000E-00

THETA (X,Y=0,Z,T=12 HR)

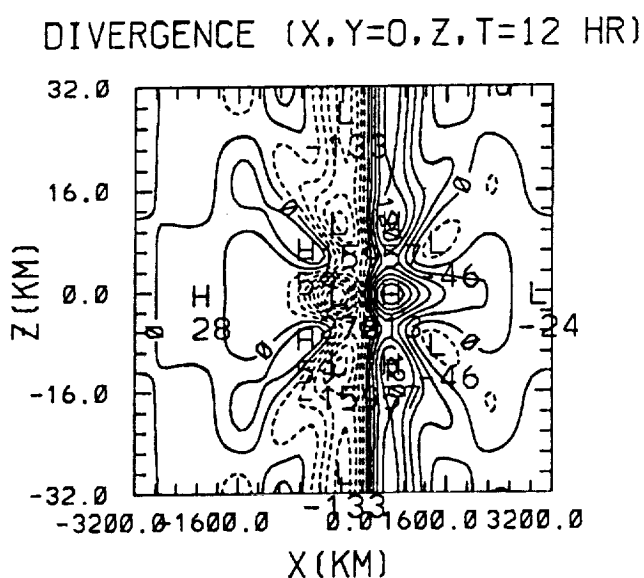
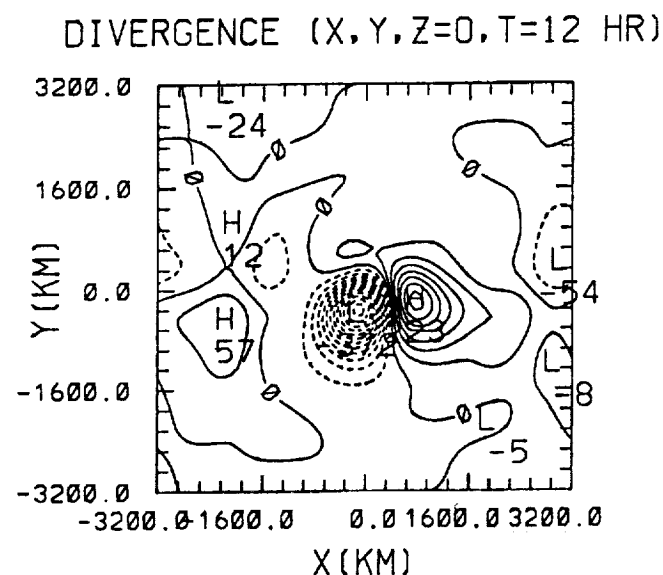


CONTOUR FROM -0.18000 TO 0.18000 INTERVAL OF 0.20000E-01

Figure 7 b



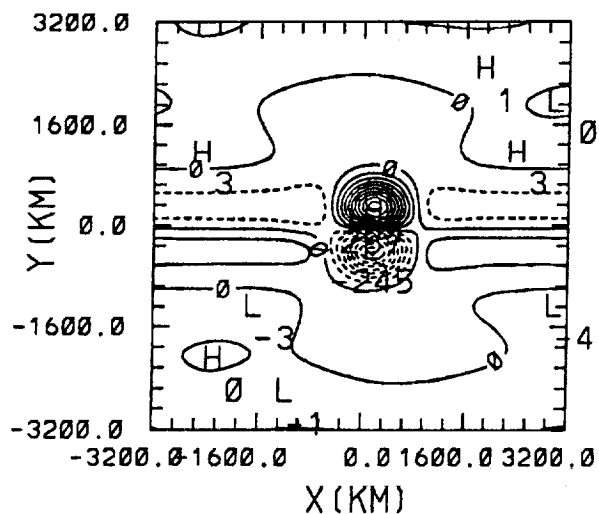
CONTOUR FROM  $-0.30000E-02$  TO  $0.80000E-03$  INTERVAL OF  $0.20000E-02$  CONTOUR FROM  $-0.30000E-02$  TO  $0.30000E-02$  INTERVAL OF  $0.30000E-03$



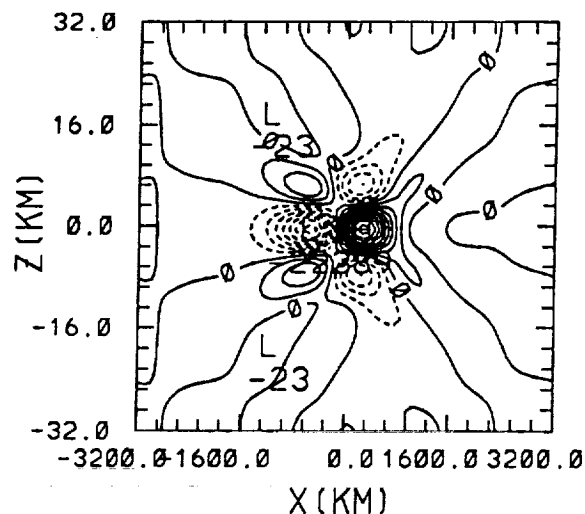
CONTOUR FROM  $-0.36000E-05$  TO  $0.21000E-05$  INTERVAL OF  $0.30000E-05$  CONTOUR FROM  $-0.24000E-05$  TO  $0.21000E-05$  INTERVAL OF  $0.30000E-06$

Figure 7 c

VORTICITY (X,Y,Z=0,T=12 HR)



VORTICITY (X,Y=0,Z,T=12 HR)



CONTOUR FROM -0.24000E-04 TO 0.27000E-04 INTERVAL OF 0.30000E-05 CONTOUR FROM -0.21000E-05 TO 0.27000E-05 INTERVAL OF 0.30000E-06

STREAMLINES (X,Y,Z=0,T=12 HR)

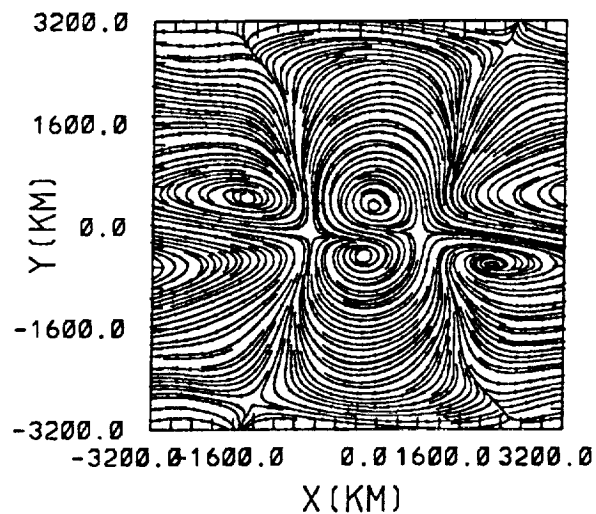


Figure 7 d

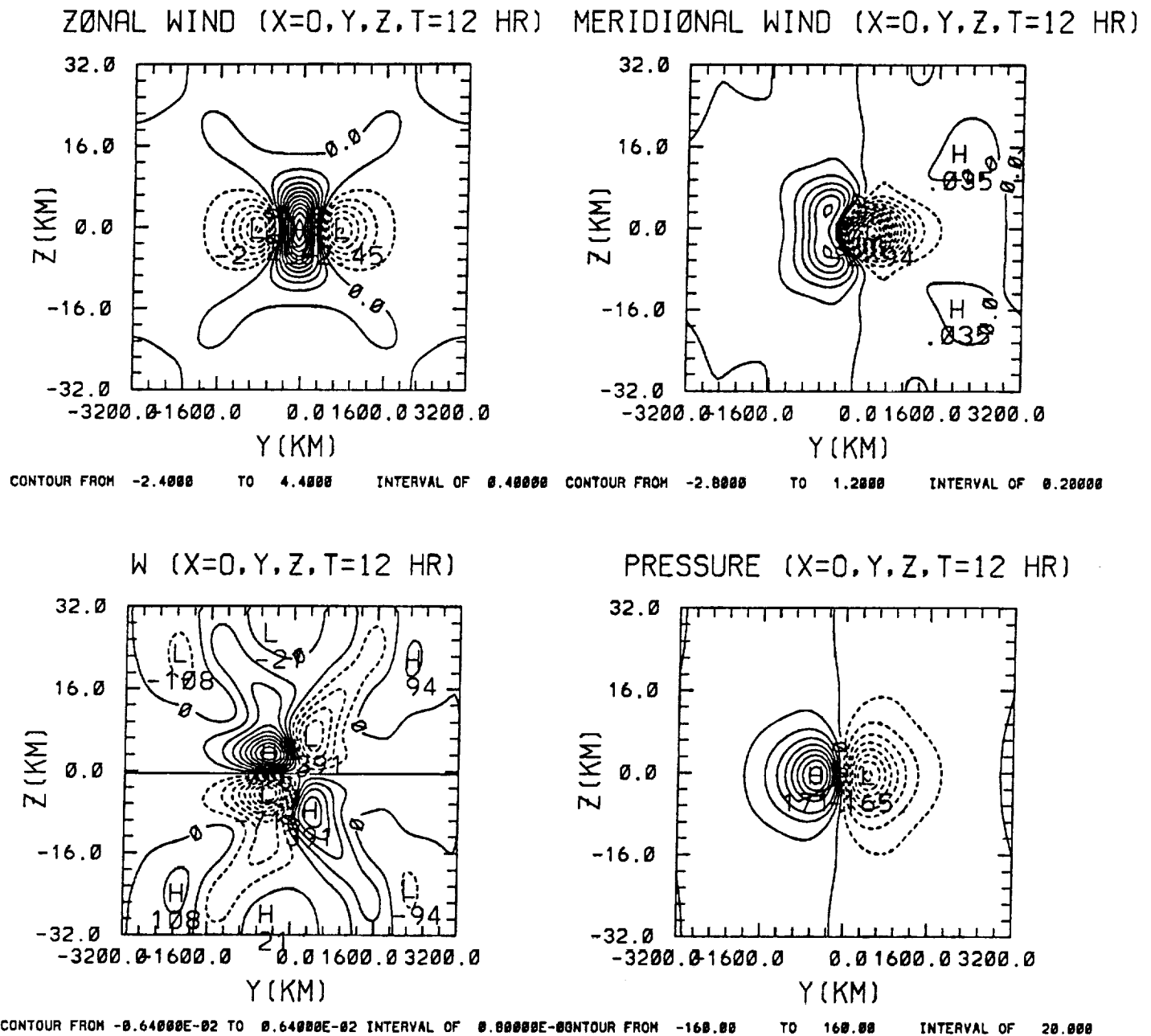


Figure 7 e

